DOI number: https://doi.org/10.15388/vu.thesis.824
https://orcid.org/0009-0006-7900-1859

VILNIUS UNIVERSITY
CENTER FOR PHYSICAL
SCIENCES AND TECHNOLOGY

Erikas Atkočaitis

Fatigue Effect in Optical Coatings: Parametric Study of Laser Irradiation Conditions, Temporal Scaling, and Lifetime Analysis

DOCTORAL DISSERTATION

Natural Sciences
Physics (N 002)

VILNIUS 2025

This dissertation was written between 2021 and 2025 at Laser Research Center, Faculty of Physics, Vilnius University.

The research was supported by the: scholarship for academic accomplishments by Research Council of Lithuania, European Union's Horizon 2020 research and innovation program (grant agreement No. 871124), European Regional Development Fund (project No. 01.2.2-LMT-K-718-01-0014 and No. 01.2.2-LMT-K-718-03-0004), Universities' Excellence Initiative programme by the Ministry of Education, Science and Sports of the Republic of Lithuania (project No. S-A-UEI-23-6), UV-Fatique (Project ID 13N17255) and PriFUSIO (Project ID 13F1000H) and Fast Coatings (Project ID 448756425).

Academic Supervisor:
Assoc. Prof. Dr. Andrius Melninkaitis (Vilnius University, Natural Sciences, Physics – N 002)

Dissertation Defense Panel:

Chairman – Prof. Dr. Aidas Matijošius (Vilnius University, Natural Sciences, Physics – N 002)

Members:
Dr. Andrejus Michailovas (Center for Physical Sciences and Technology, Vilnius, Natural Sciences, Physics – N 002),
Prof. Dr. Domas Paipulas (Vilnius University, Natural Sciences, Physics – N 002),
Dr. Volodymyr Pervak (Ludwig-Maximillian's University, München, Germany, Natural sciences, Physics – N 002),
Dr. Tomas Tolenis (ELI ERIC, ELI Beamlines Facility, Dolní Břežany, Czech Republic, Natural Sciences, Physics – N 002).

The dissertation shall be defended at a public meeting of the Dissertation Defence Panel at 10:00 on 29 September 2025 in Room 306 of the Vilnius University, Faculty of Physics, Laser Research Center.
Address: Saulėtekio al. 10, VU FF LRC, Room 306, Vilnius, Lithuania.
Tel. +370 5 236 6050; e-mail: ieva.grudiene@ff.vu.lt

The text of this dissertation can be accessed at the Vilnius University Library, as well as on the website of Vilnius University:
www.vu.lt/naujienos/ivykiu-kalendorius

DOI numeris: https://doi.org/10.15388/vu.thesis.824
https://orcid.org/0009-0006-7900-1859

VILNIAUS UNIVERSITETAS
FIZINIŲ IR TECHNOLOGIJOS
MOKSLŲ CENTRAS

Erikas Atkočaitis

Optinių dangų nuovargio efektas: lazerinės apšvietos sąlygų įtaka slenksčiui, jo dėsningumui ir ilgaamžiškumui

DAKTARO DISERTACIJA

Gamtos mokslai
Fizika (N 002)

VILNIUS 2025

Disertacija rengta 2021 – 2025 metais Vilniaus universitete, Fizikos fakultete, Lazerinių tyrimų centre.

Mokslinius tyrimus rėmė: Lietuvos moklso tarybos parama už studijų rezultatus, Europos Sąjungos tyrimų ir inovacijų programa Horizon 2020 (projekto Nr. 871124), Europos regioninės plėtros fondas (projekto Nr. 01.2.2-LMT-K-718-01-0014 ir Nr. 01.2.2-LMT-K-718-03-0004) ir Lietuvos Respublikos švietimo, mokslo ir sporto ministerijos universitetų ekslencijų iniciatyvos porgrama (projekto Nr. S-A-UEI-23-6), UV-Fatique (projekto Nr. 13N17255), PriFUSIO (projekto Nr. 13F1000H) ir Fast Coatings (projekto Nr. 448756425).

Mokslinis vadovas:
Doc. dr. Andrius Melninkaitis (Vilniaus universitetas, gamtos mokslai, fizika – N 002)

Gynimo taryba:

Pirmininkas – prof. dr. Aidas Matijošius (Vilniaus universitetas, gamtos mokslai, fizika – N 002)
Nariai:
Dr. Andrejus Michailovas (Fizinių ir technologinių mokslų centras, Vilnius, gamtos mokslai, fizika – N 002)
Prof. dr. Domas Paipulas (Vilniaus universitetas, gamtos mokslai, fizika – N 002)
Dr. Volodymyr Pervak (Ludviko ir Maksimiliano universitetas, Miunchenas, Vokietija, gamtos mokslai, fizika – N 002)
Dr. Tomas Tolenis (ELI ERIC, ELI Beamlines, Dolní Břežany, Čekija, gamtos mokslai, fizika – N 002)

Disertacija ginama viešame Gynimo tarybos posėdyje 2025 m. rugsėjo mėn. 29 d. 10:00 val. Lazerinių tyrimų centro 306 auditorijoje.
Adresas: Saulėtekio al. 10, Lazerinių tyrimų centras, 306 aud., Vilnius, Lietuva.
Tel. +370 5 236 6050; el. paštas: ieva.grudiene@ff.vu.lt

Disertaciją galima peržiūrėti Vilniaus universiteto bibliotekoje ir VU interneto svetainėje adresu: www.vu.lt/naujienos/ivykiu-kalendorius

Acknowledgement

Firstly, I would like to thank my scientific advisor, Assoc. prof. dr. Andrius Melninkaitis, who has guided, supported, and encouraged me throughout this journey into laser damage research, starting at the end of my bachelor's degree.

However, I would especially like to thank my Physics teacher, Roza Miliajeva, and my Math teacher, Violeta Bugailiškytė, from Vilnius Mykolas Biržiška Gymnasium. Teacher Roza sparked my love for physics and, specifically in a single class test during the 9th or 10th grade on the topic of work and force, opened my mind to truly understanding it. Teacher Violeta was the epitome of how to teach mathematics through logic and critical thinking rather than rote memorization of formulas.

Secondly, I would like to thank my colleagues at Lidaris – especially Egidijus P., Edvinas Z., Mindaugas Š., dr. Justinas G., and Austėja A. – who lent a hand during experiments and helped resolve various issues with laser systems.

Thirdly, I thank all my fellow PhD students – Jonas B. , Vaida M., Marius N., Evaldas K., Indrė M., dr. Dominyka S., dr. Miglė K., Jokūbas P. – and everyone else with whom I spent countless hours both discussing ideas and talking nonsense on the third floor of the VU Laser Research Center.

Of course, I am also grateful to the professors, associate professors, and staff of the Laser Research Center who supported me in various ways during my PhD studies.

Importantly, I am deeply grateful to both local and international colleagues – dr. Vytautas Jukna, dr. Julius Vengelis, dr. Marco Jupé, dr. Morten Steinecke, prof. dr. Laurent Gallais, dr. Linas Smalakys, dr. Simonas Kičas, and Vaida Grašytė – who directly contributed to my research.

I must also acknowledge the former director of the Laser Research Center and current Dean of the VU Faculty of Physics, prof. dr. Aidas Matijošius, as well as the current LRC director, dr. Dalia Kaškelytė, whose continuous support and guidance throughout the PhD years have been invaluable. I cannot imagine the VU Laser Research Center without them.

I am immensely thankful to my friends – mostly Andrius G., Urtė K., Ieva D., Dominyka L., Tomas L., dr. Vytautas Ž., and Dovydas A. – who pulled me away from my work to relax and reminded me to enjoy life beyond thesis.

And finally, I must thank my two cats, Audra (Storm) and Gūsis (Wind Gust), who slept on my legs while I wrote the thesis, zoomed around the room when I needed a break, and used their paws on the keyboard to make their own tiny contributions to this research.

Table of contents

List of abbreviations

UV	Ultraviolet
DUV	Deep Ultraviolet
HAZ	Heat Affected Zones
fs	Femtosecond
ps	Picosecond
ns	Nanosecond
ms	Milisecond
CW	Continuous-wave
IR	Infrared
2PA	Two-Photon Absorption
3PA	Thre-Photon Absorption
AR	Anti-reflective
LIDT	Laser-induced damage threshold
LID	Laser-induced damage
CB	Conduction band
VB	Valence band
MPI	Multiphoton ioniation
MPA	Multiphoton absorption
AI	Avalanche ionization
STE	Self-trapped excitons
IBS	Ion beam sputtering

List of frequently used symbols

τ	Pulse duration
I	Intensity
A	Absorptance
α	absorption coefficient
ω_{MPI}	Multiphoton ionization rate
S	Number of pulses
β_{m}	m-photon absorption coefficient
F	Fluence
λ	Wavelength
ρ	Free electron density

Introduction

Laser–matter interaction is a fundamental physical process that underpins a wide range of technological advancements. From everyday applications – such as nanoscale lithography in electronics [1] and precision machining of macroscale structures [2] – to large-scale initiatives like space exploration [3] and inertial confinement fusion for clean energy generation [4], lasers have had a profound and far-reaching impact. Despite their versatility, a common challenge across laser-based technologies is the operation of optical components under extreme conditions, including ultrashort pulse durations, high peak irradiance, and extreme wavelengths. These regimes inevitably give rise to laser-induced damage (LID), which remains a major limitation to the further advancement and reliability of high-performance laser systems [5].

In photonics, a broad spectrum of laser systems operates with varying parameters. These systems rely on optical components to guide and deliver the beam either to the laser output or to the target site, depending on the application. Such components are often coated with dielectric or metallic films, each exhibiting distinct optical and mechanical properties. As a result, their resistance to LID varies significantly depending on the coating material, its structural design, and the specific laser parameters.

Among these laser parameters, pulse duration [6], repetition rate [7], wavelength [8], and beam diameter [9] are key influences on the onset and progression of LID. Understanding how each of these parameters affects optical performance – and how such effects can be reliably predicted – is essential. This variability has prompted the development of scaling laws to model and estimate laser-induced damage threshold (LIDT) across different exposure conditions. Although many studies have investigated LIDT scaling with individual parameters, they are often limited by narrow experimental ranges or contradictory findings.

Notably, most LIDT scaling studies have focused on single-shot damage, while in practice, optical components typically operate under prolonged irradiation. In these conditions, materials may not fully recover between pulses, resulting in cumulative degradation. This phenomenon, known as the fatigue effect [10], can significantly influence the long-term performance and lifetime of optical elements. At present, lifetime estimation methods rely either on extrapolating short-term multi-pulse LIDT results [11], which can result in unreliable prediction, or on direct long-duration testing, which is time- and cost-intensive.

While progress has been made in LIDT characterization and scaling law development, critical gaps remain – particularly in understanding how combined laser parameters, prolonged exposure affect optical material behavior,

and which material properties govern these responses. Current models often rely on simplified conditions or limited datasets and may not accurately reflect the cumulative degradation observed in real-world laser systems. This highlights the need for a more comprehensive and predictive framework that integrates both damage threshold behavior and long-term optical stability.

The goal of the thesis

The main goal of this dissertation is the investigation of laser-induced damage threshold scaling laws and laser-induced fatigue effect for the prediction and characterization of the lifetime in optical thin film coatings.

The main tasks of the thesis

The following tasks were set to reach the goal of the dissertation:

- Distinguish and analyze the LIDT scaling laws on pulse duration between failure modes in dielectric coatings using ultraviolet (UV) and infrared (IR) wavelengths.
- Conduct qualitative and quantitative studies of LIDT scaling with pulse duration in thin metallic coatings; critically evaluate existing predictive models and refine them through theoretical analysis and experimental validation.
- Perform an experimental study on temporal absorptance behavior in dielectric coatings across the UV – IR wavelength range.
- Develop a universal predictive model for the optical lifetime of dielectric coatings subjected to ultrashort pulse laser irradiation.

Practical and scientific novelty

While catastrophic LIDT scaling laws and fatigue behavior have been extensively studied, the influence of color change damage on catastrophic damage remains poorly understood. Moreover, existing optical lifetime prediction models are predominantly based on the onset of catastrophic damage fatigue, overlooking the potential role of sub-catastrophic color change damage in long-term optical degradation.

- For the first time, the LIDT of laser-induced color changes in dielectric coatings was investigated as a function of pulse duration (τ). Theoretical analysis based on free-electron generation equations suggests that the

temporal scaling law is influenced by the material bandgap and the laser wavelength. These observations are discussed in Chapter 3.

- A comprehensive study on LIDT scaling with pulse duration in metallic and semiconductor coatings revealed a nontrivial dependence on the coating thickness and specific heat capacity, which is governed by the thermal decay constant of the material. These observations are discussed in Section 3.1.

- Multipulse LIDT analysis of multilayer AR coatings revealed that fatigue of catastrophic damage exhibits dependence on pulse duration at both IR and UV wavelengths, whereas the fatigue behavior of the color change mode appears largely insensitive to pulse duration. These observations are discussed in Section 3.2.

- The combined analysis of color change damage morphologies and temporal absorptance dynamics in dielectric coatings demonstrated distinct absorptance behavior depending on whether the material has undergone thermal annealing, providing deeper insights into the formation of the color change damage and long-term material behavior. These observations are discussed in Chapter 4.

- For the first time, the temporal absorption behavior of dielectric coatings was investigated as a function of pulse duration. Absorptance data were analyzed using rate equation models, revealing that classical multiphoton absorption process alone cannot fully explain the observed results. A simple numerical model suggests that intermediate defect states may also play a significant role in the nonlinear optical properties, which depend on pulse duration and exposure history. These observations are discussed in Section 4.2.

- Combining LIDT and absorption measurement techniques enabled the analysis of the relationship between absorptance and laser-induced color change fatigue across deep-UV (DUV) to IR wavelengths at a fixed pulse duration. These observations are discussed in Chapter 5.

- The analysis of absorbed dose in dielectric coatings allowed the construction of a phenomenological optical lifetime prediction model. These observations are discussed in Chapter 5.

Statements to be defended

1. Laser-induced damage threshold scaling with pulse duration in optical coatings is not governed by a widely accepted $\tau^{0.5}$ law, but is instead

determined by the failure mode, incident wavelength, number of pulses, and intrinsic material properties.

2. In metallic coatings, the laser-induced damage threshold in the pulsed regime is primarily limited by the absorptance and specific heat capacity of the coating, whereas in the continuous-wave regime, heat diffusion within the substrate becomes the dominant limiting factor.

3. Laser-induced color changes in dielectric coatings can be initiated through either linear or nonlinear absorption processes, provided that a total absorbed dose threshold is reached.

4. The total absorbed dose threshold that governs the lifetime of dielectric coatings with respect to color change damage is strongly dependent on material properties and photon energy, which together determine the order of the absorption process.

5. Laser-induced color change damage in dielectric coatings can result from at least two distinct physical mechanisms: a laser-driven annealing process or the breaking of chemical bonds.

Approbation of the research results

List of publications, related to the dissertation topic

[A1] **E. Atkočaitis**, L. Smalakys, A. Melninkaitis, Pulse temporal scaling of LIDT for anti-reflective coatings deposited on lithium triborate crystals, Opt. Express **30**(16), 28401-28413 (2022).

[A2] **E. Atkočaitis**, M. Keršys, S. Kičas, V. Grašytė, A. Melninkaitis, Nonlinear absorptance of single-layer HfO_2 coatings: investigating the impact of thermal and laser annealing, Opt. Express **31**(23), 38376-38387 (2023).

[A3] **E. Atkočaitis**, A. Aleksiejūtė, J. Galinis, A. Melninkaitis, The Role of Absorbed Dose in Lifetime of HfO_2 and SiO_2 Dielectric Coatings, Opt. Express **33**(7), 38376-38387 (2023).

[A4] **E. Atkočaitis**, M. Jupé, U. Kimbaraitė, L. Gallais, E. Žutautaitė, K. Kiedrowski, M. Steinecke, L. Herrero, L. Jensen, M. Ščiuka, A. Varanavičius, G. Jansonas, A. Melninkaitis, Exploring Laser-Induced Damage Threshold in Metallic Coatings Across Fifteen-Order Magnitude Range of Pulse Lengths, Opt. Express, accepted to publish in 2025.

[A5] **E. Atkočaitis**, A. Melninkaitis, Absorbed Dose Threshold for Single-layer ZrO_2, HfO_2 and Al_2O_3 Dielectric Coatings at 355 nm, Opt. Letters **50**(16), 4910-4913 (2025).

Conference proceedings

[A6] **E. Atkočaitis**, A. Melninkaitis, Real-time investigation of the UV nonlinear absorptance in an anti-reflective coated LBO crystals, Proc. SPIE **12300**, Laser-Induced Damage in Optical Materials 2022, 123000J (2 December 2022).

Other publications

[A7] L. Rimkus, J. Darginavičius, **E. Atkočaitis**, A. Augus, Solid-state femtosecond UV lasers: recent advances and challenges, Proc. SPIE **12652**, UV and Higher Energy Photonics: From Materials to Applications 2023, 1265206 (5 October 2023).

International conference presentations

This section lists conference presentations where the author was either the main presenter or the author's work was presented by another contributor.

[C1] M. Jupé, **E. Atkočaitis**, E. Žutautaitė, K. Kiedrowski, M. Steinecke, L. Herrero, L. Jensen, U. Kimbaraitė, M. Šciuka, A. Melninkaitis, Experimental study of LIDT scaling laws for metallic coatings: effect of pulse duration within fifteen orders of magnitude, SPIE Laser Damage, (online), 2021.

[C2] E. Drobužaitė, L. Smalakys, **E. Atkočaitis**, A. Melninkaitis, Analysis of lifetime distributions of dielectric and metallic mirrors, SPIE Laser Damage, (online), 2021.

[C3] **E. Atkočaitis**, L. Smalakys, A. Melninkaitis, Antireflection coatings on LBO crystals: investigation of LIDT scaling with pulse duration at IR and UV wavelengths, SPIE Laser Damage, (online), 2021.

[C4] **E. Atkočaitis**, L. Smalakys, A. Melninkaitis, Experimental and numerical study of LIDT pulse temporal scaling for anti-reflective coated LBO crystals, SPIE Laser Damage, Rochester, NY, USA, 2022.

[C5] **E. Atkočaitis**, A. Melninkaitis, Real-time investigation of UV nonlinear absorptance in anti-reflective coated LBO crystals, SPIE Laser Damage, Rochester, NY, USA, 2022.

[C6] **E. Atkočaitis**, M. Keršys , S. Kičas, V. Grašytė, A. Aleksiejūtė, J. Galinis and A. Melninkaitis, Exploring nonlinear effects of laser irradiation on single- and multi-layer dielectric coatings: a study on HfO_2, ZrO_2 and Al_2O_3 coatings, SPIE Laser Damage, Dublin, CA, USA, 2023.

[C7] **E. Atkočaitis**, S. Kičas, V. Grašytė A. Aleksiejūtė, J. Galinis and A. Melninkaitis, Investigation of IR-UV nonlinear absorptance in HfO_2, ZrO_2 and Al_2O_3 single- and multi-layer coatings, SPIE Optics + Optoelectronics, Prague, Czech Republic, 2023.

[C8] A. Melninkaitis, **E. Atkočaitis**, A. Aleksiejūtė, E. Pupka, J. Galinis, S. Kičas, V. Grašytė, R. Grigutis, L. Smalakys, Laser-Induced Damage in Optical Elements: From Threshold Toward a Lifetime, **Invited Talk**, OPTICA Design and Fabrication Congress, Québec city, Canada, 2023.

[C9] **E. Atkočaitis**, A. Aleksiejūtė, J. Galinis, S. Kičas, V. Grašytė and A. Melninkaitis, Investigating the lifetime of dielectric coatings: the role of absorption, SPIE Laser Damage, San Ramon, CA, USA, 2024.

[C10] V. Pervak, **E. Atkočaitis**, A. Melninkaitis, Exploring non-linear absorptance in Ta_2O_5, HfO_2, and SiO_2 oxide coatings: a comparative analysis, SPIE Laser Damage, San Ramon, CA, USA, 2024.

[C11] **E. Atkočaitis**, A. Aleksiejūtė, J. Galinis, and A. Melninkaitis, The Role of Absorbed Dose in Lifetime of Dielectric Coatings, OCLA, Vilnius, Lithuania 2025.

National conference presentations

[C12] **E. Atkočaitis**, M. Jupé, E. Žutautaitė, L. Smalakys, K. Kiedrowski, M. Steinecke, L. Herrero, L. Jensen, U. Kimbaraitė, M. Ščiuka, A. Varanavičius, G. Jansonas, A. Melninkaitis, Ar egzistuoja Moore'o dėsnis optiniam atsparumui?, 44th National Lithuanian conference of Physics, Vilnius, Lithuania, 2021.

[C13] **E. Atkočaitis**, S. Kičas, V. Grašytė, A. Aleksiejūtė, J. Galinis and A. Melninkaitis, Investigations of nonlinear absorptance and fatigue effect in HfO_2, ZrO_2 and Al_2O_3 dielectric coatings, Open Readings, Vilnius, Lithuania, 2023.

Contribution of the author

The author of this dissertation has contributed to the design of experiments, performed the majority of LIDT and all absorption measurements, analyzed all experimental results and prepared manuscripts for publications [**A1** – **A5**]. The author has performed numerical rate equation, morphological analysis in publication [**A1**], developed numerical analysis for the absorption and optical lifetime assessment in publications [**A3, A5**], and performed numerical analysis in publications [**A2, A5**].

Contribution of the co-authors

- Assoc. prof. dr. Andrius Melninkaitis was involved in all studies outlined in this dissertation. He formulated the main tasks and objectives, provided analytical insights on the results, proofread the prepared manuscripts, offered advice on experiments and their design, numerical modeling, and, in general, laser-induced damage and absorption physics.
- Dr. Linas Smalakys offered advice as well as technical insights on the morphological evaluation of the color change damage in publication [**A1**].

- Martynas Keršys helped write code for the numerical modeling in publication [**A2**].
- Dr. Simonas Kičas and Vaida Grašytė provided experimental samples and spectral measurements for samples in publications [**A2, A3, A5**].
- Austėja Aleksiejūtė helped performing LIDT measurements in publication [**A3**].
- Dr. Justinas Galinis helped with damage site analysis in publication [**A3**]. and with morphological analysis in [**A5**].
- Dr. Marco Jupé, dr. Kevin Kiedrowski, dr. Morten Steinecke, dr. Lars Herrero, and dr. Lars Jensen provided experimental samples in publication [**A4**]
- Urtė Kimbaraitė and Mindaugas Ščiuka helped perform LIDT measurements with CW laser in publication [**A4**].
- Emilija Žutautaitė helped with numerical simulations of the heat transport model in publication [**A4**].
- Prof. dr. Laurent Gallais provided numerical simulations of the two-temperature model and the heat transport model in publication [**A4**].
- Dr. Arūnas Varanavičius and Gaudenis Jansonas provided help and expertise in LIDT experiments with a sub-10 fs NAGLIS OPCPA system in publication [**A4**].
- Dr. Vytautas Jukna provided code for numerical simulations and insights into absorption behavior in Section 4.2.

Layout of the dissertation

The dissertation is presented as a collection of articles and unpublished data, with chapters *3 – 5* summarizing the main findings from papers [**A1 – A5**]. The papers are numbered in chronological order of their publication date. *Chapter 1*, Literature overview, provides an overview of the current state of knowledge on laser-induced damage, fatigue effect, and absorptance behavior in optical materials. *Chapter 2*, Experimental methods and characterization techniques, outlines the experimental setups and procedures used to evaluate LIDT and absorptance. *Chapter 3*, Laser-induced damage threshold scaling laws on pulse duration, discusses LIDT scaling on pulse duration in metallic and dielectric coatings and related physical phenomena. *Chapter 4*, Nonlinear absorption influence on LIDT, discusses absorption behavior in dielectric coatings with different irradiation conditions. *Chapter 5*, Absorption influence on

fatigue effect, discusses how absorption-related processes affect the long-term performance of optical components.

1. Literature review

1.1 Laser-induced damage

International Standardization Organization (ISO) has defined LID as any permanent laser-radiation-induced modification in the surface or bulk of a specimen that is detectable using an inspection technique with a sensitivity appropriate to the intended function of the optical component (ISO 21254 [11]). The LIDT is further defined as the highest laser fluence or intensity at which the extrapolated probability of damage is zero. This definition of LID is applicable for observable damage with microscopy, which corresponds to the majority of inspected damage types.

The broad definition of LID as *any* permanent change implies the existence of multiple failure modes. The most commonly encountered damage in coatings is *catastrophic damage* (see Fig. 1.1), which is characterized by ablation and/or crater formation at the irradiated site [12]. This type of damage can lead to the complete failure of the optical component. Usually, it resembles an ablated

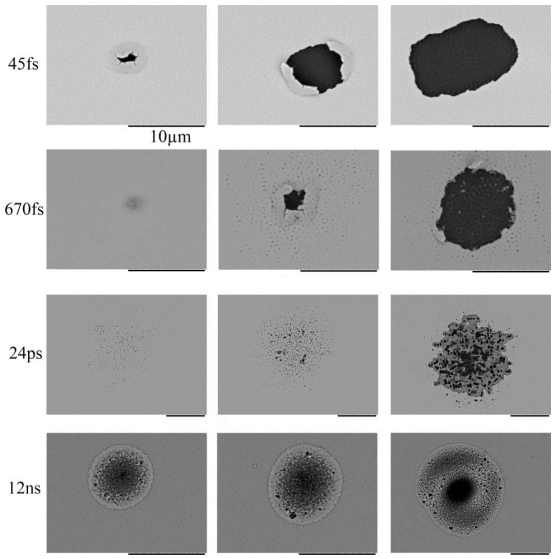

Figure 1.1: Damage morphologies for pulsed laser irradiation obtained with scanning electron microscope with increasing fluences (from left to right) on single-layer hafnia coating [13].

surface with a crater pit in the center of the irradiated area. Depending on the pulse duration (the influence of pulse duration on LIDT will be discussed in Sec. 1.4.1), the catastrophic damage morphology in dielectrics also varies.

At short pulses (<10-20 ps), the initial damage crater with delamination signs appears to be localized to the small region of the peak of the Gaussian intensity distribution. At longer pulses (>20 ps), the morphology transitions to sub-micrometer pits, which are no longer localized to the peak intensity region, along with melting and re-solidification. For metals (see Fig. 1.2), the damage

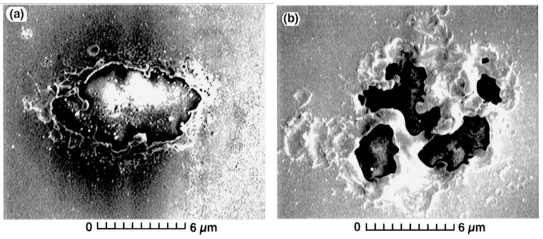

Figure 1.2: Typical damage on gold coating [6] with a) 900 ps pulses and b) 0.6 ps pulses.

mechanism is different from that of dielectric coatings (see Section 1.4.1.2). In this case, damage morphologies exhibit material melting and boiling across all pulse durations (fs – CW (continuous-wave)).

A second type of damage is *non-catastrophic damage*, often referred to as *color change* or *color mode* (see Fig. 1.3), which manifests as a hue shift in the irradiated area without mechanical destruction [10]. Such material modi-

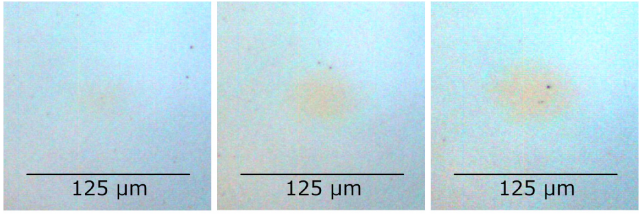

(a) 10^4 pulses, 0.89 J/cm^2 (b) 10^5 pulses, 0.78 J/cm^2 (c) 10^6 pulses, 0.72 J/cm^2

Figure 1.3: High contrast Nomarski images of color change damage for ZrO_2 coating at different pulse number and fluences [14].

fication occurs with multi-pulse exposure at fluences below catastrophic LIDT [15]. In some cases, these modifications remain undetectable by conventional inspection methods and require specialized visualization techniques. For instance, digitally comparing phase changes between pre- and post-irradiation images captured with a differential interference contrast (DIC) microscope enables the identification of subtle structural changes [16]. Color change has been observed to be localized within the irradiated area.

A third category, known as *functional damage*, has recently gained attention [17, 18]. It refers to performance degradation (such as deviation from certain optical specifications) caused by laser-induced changes, even when no visible

damage is observed.

Most laser systems operate below the single-pulse LIDT. However, damage has been observed after prolonged exposure [10]. This phenomenon, referred to as the *fatigue effect*, results from the accumulation of sub-single-pulse threshold modifications over repeated irradiation. Fatigue is commonly quantified as the difference between the single-shot and multi-shot LIDTs. Consequently, the *lifetime* of an optical component is closely tied to fatigue behavior and is often estimated by extrapolating multi-pulse LIDT data to predict performance under real-world operating conditions. In this context, the *optical* lifetime refers to the duration of exposure required to reach the damage threshold, i.e., the long-term LIDT. There are several fatigue mechanisms which will be discussed in Section 1.3.

1.2 Mechanisms of laser-induced damage

Any laser-matter interaction typically begins with the transfer of energy from incident photons to charge carriers within the material, a process known as absorption. Depending on the interaction regime, laser light absorption can generally be categorized into two types:

- a controlled and purposeful effect, such as harmonic generation [19, 20], optical parametric amplification [21], generation [22], and oscillation [23], and optical parametric chirped pulse amplification [24, 25];
- an unintended effect that leads to optical power losses and potential degradation of optical components.

This section will focus on the negative aspect of the absorption within materials – an initial cause of laser-induced damage.

Dielectric coatings on optical elements absorb light, generating free electrons and heat, ultimately limiting the durability and maximum achievable power of the entire optical system. The schematic illustration of the main processes, leading to the initiation of LID, is shown in Fig. 1.4. Since the absorptance of dielectric coatings depends not only on wavelength but also on intensity [26], these effects must be carefully considered when designing coatings for high-power laser applications. For this reason, absorption effects have been thoroughly investigated throughout this work across various optical surfaces, resulting in numerous measurements aimed at optimizing coating performance.

In wide-bandgap optical materials, nonlinear absorption is a consequence of the absorption process under high-intensity or high-photon-energy irradiation and plays a significant role in the formation of laser-induced damage. Typically, the energy of a photon in the UV – IR wavelength range is lower than the bandgap of wide-bandgap materials. Therefore, the most natural concept is

the simultaneous absorption of several photons whose sum energy is enough to bridge the bandgap. This type of interband transition is known as multiphoton absorption (MPA). Alternatively, electrons can reach the CB via tunneling ionization due to an extremely strong electric field [27]. The tunneling electron does not induce immediate absorption of light since its energy is constant during the tunneling. However, it generates free electrons in CB, which do absorb laser light via inverse bremsstrahlung (IBH) [28].

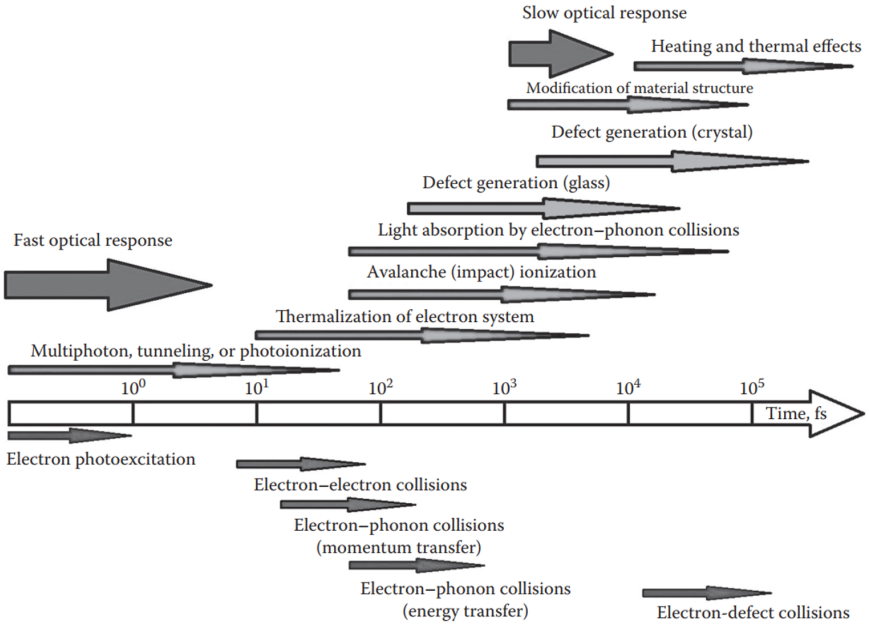

Figure 1.4: A scheme of time hierarchy of laser-induced microscopic processes (arrows in bottom part of figure) and related particle dynamics (arrows in top art of figure) in transparent media [12].

1.2.1 Linear absorption and thermal damage

Absorption in a medium can be linear and nonlinear. Linear absorption defines such an absorptance that does not change at different intensities. The absorptance linearity will only be maintained as long as the incident light does not change the initial number of absorbers in the ground state. Generally, absorptance can be defined as a fraction of intensity before and after the medium [26]:

$$I = I_0 \exp[-\alpha_{\text{linear}} z] \tag{1.1}$$

where I is intensity after the medium, I_0 is initial intensity, α_{linear} is linear absorption coefficient and z is optical thickness. Eq. 1.1 describes how the irradiance decreases exponentially as a function of propagation distance in a

linearly absorbing medium. For transparent media, linear absorption often is insufficient to induce thermal damage with pulsed lasers (see Fig. 1.4). However, linear absorption is one of the driving mechanisms in the CW pulse width range and for metallic materials.

In metallic coatings, free electrons are abundant and are excited through IBH, which then transfers their energy to the lattice via electron–phonon interactions. If the absorbed energy does not dissipate quickly enough, it accumulates within the lattice, eventually raising the local temperature to the melting point. Once this threshold is reached, material modification or damage occurs.

One of the models that explains LID in metallic materials is a one-dimensional heat flow calculation model described by Wood [29], where a semi-infinite medium (without coating) is assumed with temperature-independent absorption properties. For CW irradiation, thermal diffusion must be accounted for, and the temperature rise in the stationary regime at the surface may be approximated by the equation:

$$\Delta T = \frac{PA}{2\rho C r \pi D}, \tag{1.2}$$

where ΔT is the temperature difference between T_{melt} melting point and T_{init} initial temperature, P is incident power, A is absorptance, ρ is the volumetric density, C is specific heat capacity, D is the diffusivity, r is the beam radius. In the pulsed regime, energy deposition is instantaneous, and thus heat conduction is negligible, leading to a temperature rise:

$$\Delta T = \frac{P\tau A}{\rho C V}, \tag{1.3}$$

where $V = \pi r^2 h$ is the irradiated volume, h is the thickness of the material.

Equations 1.2 and 1.3 describe the melting temperature as the primary damage criterion under linear absorption. However, as the material heats, it may reach a threshold for volumetric expansion, leading to critical internal stress and resulting in catastrophic cracking. In such a case, the LIDT (E_{D}) in CW regime can be evaluated by:

$$E_{\mathrm{D}} = \frac{4\kappa C D S \tau}{\beta \alpha r^2} \tag{1.4}$$

and in pulsed regime by:

$$E_{\mathrm{D}} = \frac{C\kappa S}{\beta\alpha} \tag{1.5}$$

where S is the damaging stress, β is the volume expansion coefficient, κ is thermal conductivity.

1.2.2 Nonlinear absorption-induced and electronic damage

1.2.2.1 Multiphoton absorption

As mentioned earlier, the intensity in a material declines exponentially in a linearly absorbing medium (Eq. 1.1 in Section 1.2.1). However, when intensities are high enough to excite multiple electrons, the classical Beer-Lambert law does not hold because the absorptance will be a nonlinear intensity function at any given time. For a monochromatic wave, MPA can be expressed as a simple power-series expansion [30]:

$$\frac{dI}{dz} = -\alpha_{\text{linear}} I - \beta_2 I^2 - \beta_3 I^3 - ... \tag{1.6}$$

MPA is typically described by the nonlinear absorption coefficient [31] $\beta_{\text{m}} \equiv m\hbar\omega\sigma_{\text{m}}N_0$ (σ_{m} – m-photon absorption cross-section, N_0 – initial electron density). Accurate evaluation of nonlinear absorption coefficients is critical for the design of substrates and coatings aimed at minimizing nonlinear effects and improving laser damage resistance [32]. This is particularly important for multilayer dielectric coatings, where nonlinear absorption can strongly influence damage formation. In the femtosecond to picosecond pulse duration regime, LID is often confined to individual layers within the coating stack [6]. However, due to electric field interference effects, failure typically initiates at the interface between low- and high-refractive-index materials, most often within the first layer pair of the multilayer structure [33]. Therefore, understanding and controlling nonlinear absorption behavior is essential for mitigating early-stage damage and extending the optical lifetime of multilayer coatings.

1.2.2.2 Laser-induced free electron generation

One of the principal damage formation mechanisms in solid dielectrics is governed by nonlinear electron excitation from the valence band (VB) to the conduction band (CB) and the subsequent generation of free electrons until critical electron density is reached (10^{21} cm^{-3}). In general, the accepted laser-induced plasma formation sequence proceeds as follows [27]: charge carriers are initially generated by MPA. These carriers absorb energy from the laser field via IBH, creating additional carriers through impact ionization (II). The newly generated carriers absorb laser energy and trigger further II events, initiating an avalanche ionization (AI) process. This picture is valid when MPI – AI interplay has sufficient development time, typically for pulse durations in the picosecond or longer range. However, for femtosecond pulses, the dynamics become more complex, and the contribution of AI may be significantly overestimated [34].

The simplest way to describe electron generation in dielectrics while considering both MPI and AI processes is through the single-rate equation (SRE) model [6]:

$$\frac{dN}{dt} = \omega_{\mathrm{MPI}} + \alpha_{\mathrm{AI}} IN - \gamma N \tag{1.7}$$

where N represents the carrier density, I – intensity, ω_{MPI} is multiphoton ionization rate [27], α_{AI} – avalanche ionization constant, γ – carrier recombination. This model assumes a linear relationship between AI and intensity, justified by the linear heating rate of carriers at a given intensity. However, this linearity implies that all carriers contribute equally to AI regardless of their energy, leading to overestimating the AI contribution, particularly at lower intensities. In reality, the electrons need to gain a specific amount of energy before they can cause collisions with other carriers to excite new valence electrons [35]. Although the SRE model is an oversimplification, it remains valuable for capturing the major trends of laser-induced damage formation.

To address the limitations of SRE, Kaiser *et al.* [35] proposed a more detailed model that incorporates interactions between photons, phonons, and charged carriers. In this approach, electrons initially excited by MPA accumulate at discrete energy levels corresponding to integer multiples of the photon energy ($\hbar\omega$), forming sharp spikes (δ distribution function) in the carrier energy distribution. These spikes gradually broaden due to the thermalization process occurring over a few femtoseconds. By dynamically tracking the energy distribution, the model accurately determines the fraction of carriers that surpass the critical energy ϵ_{c} necessary for impact ionization. Consequently, AI is correctly attributed to the high-energy subset of carriers rather than the entire electron population, avoiding the overestimation inherent in the SRE model.

Figure 1.5 illustrates electron generation dynamics relative to pulse duration, separating contributions from strong electric field ionization (SEFI, i.e., multiphoton ionization) and II throughout and after the laser pulse. For top-hat pulse profiles (see Fig. 1.5 a) – d)), ionization rates increase linearly during the pulse duration. II becomes significant only once sufficiently high-energy carriers are present, leading to a delayed onset compared to MPI. For ultrashort pulses (25 fs), electrons do not have enough time to accumulate sufficient energy during the pulse, rendering the contribution of II negligible (Fig.1.5a)). In contrast, for pulses of 200 fs (or longer) II contribution becomes comparable to MPI. II continues for approximately 100 fs after irradiation until no electrons remain in CB with sufficient energy to continue II, and the electron density saturates. For Gaussian pulse profiles (Fig. 1.5e), electron generation primarily occurs near the peak intensity, further emphasizing the delayed contribution of II relative to MPI.

Although the model by Kaiser et al. provides an excellent description of carrier dynamics during laser irradiation, it requires solving a large number of

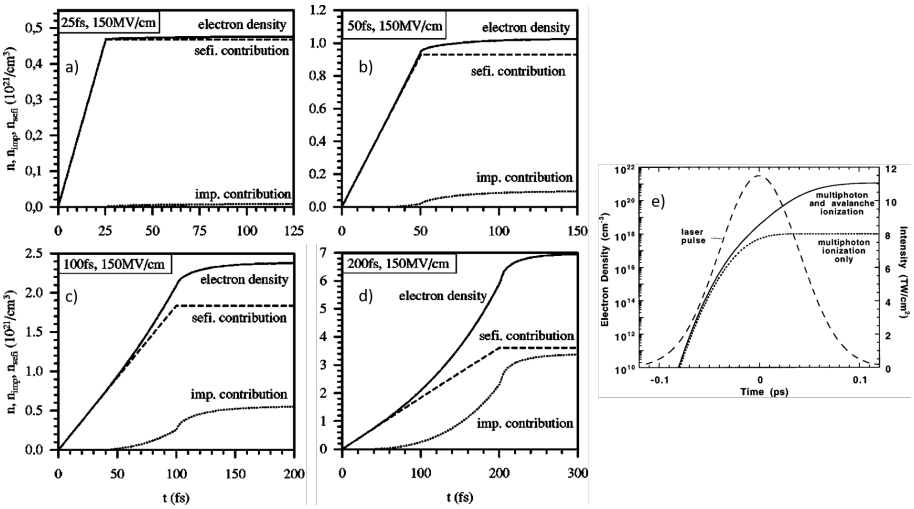

Figure 1.5: Time dependence of free-electron density and the contributing processes, i.e., strong-electric-field ionization (sefi) and impact ionization with an electric field of 150 MV/cm and pulse lengths of a) 25 fs, b) 50 fs, c) 100 fs, and d) 200 fs, respectively [35]. e) illustrates how electron densities are produced by MPI alone and in combination with AI, plotted along with the 100 fs Gaussian pulse shape [6].

coupled differential equations. To simplify the modeling while preserving critical features, Rethfeld [34] introduced the multi-rate equation (MRE) model, which discretizes the carrier energy distribution without assuming thermalization. Energy levels are separated by $\hbar\omega$, with the threshold for impact ionization reached after $k = \lceil \epsilon_c/\hbar\omega \rceil$ photon absorptions.

The MRE model formulates rate equations for each energy level, summarized as:

$$\frac{dN}{dt} = \omega_{\mathrm{MPI}} + \sum_{s=e,h} \gamma_{\mathrm{n}}^{\mathbf{s}} N_{\mathrm{k}}^{\mathbf{s}} - \gamma N \tag{1.8}$$

where s=e,h is for electrons and holes, respectively, $\gamma_{\mathrm{n}}^{\mathbf{s}}$ describes excited carrier collisions (which have energy $\geq \epsilon_c$) with neutral carriers in k-th energy level. While Eq.1.8 resembles the SRE (Eq. 1.7), it differs fundamentally: AI now depends only on the population of carriers above the critical energy, introducing a natural delay between MPI and AI onset. Thus, the MRE model more accurately captures the sequence of nonlinear ionization events during femtosecond to picosecond laser irradiation in dielectric materials.

1.2.2.3 Coulomb explosion

Coulomb explosion (CE) is recognized as a prominent non-thermal laser-induced damage mechanism, particularly under femtosecond laser irradiation. It arises when a rapid photoionization process, often via multiphoton or tunnel-

ing ionization, leads to the escape of a substantial number of electrons from the surface of the material, leaving behind a highly charged, electrostatically unstable lattice. This localized positive charge generates intense repulsive forces between ions, ultimately causing the ejection of atomic or cluster species from the surface in an explosive manner.

In dielectric materials, this phenomenon has been experimentally confirmed [36]. It has been shown that under sub-threshold femtosecond laser fluences, CaF_2 surfaces emit predominantly positive ions with high kinetic energies ($\sim$10 eV), largely independent of their mass [37]. Their time-of-flight mass spectrometry revealed a strong forward-peaked ion emission and distinct non-thermal energy distributions, further supporting CE as the underlying mechanism. Additionally, they observed a fluence-dependent transition to thermal ablation, highlighting the CE dominance at low fluence and the onset of thermal effects at higher intensities. A theoretical framework for Coulomb explosion applicable across different material classes has been developed within a continuum drift-diffusion approach. This model emphasizes the role of charge carrier transport properties in determining the feasibility of surface charging and subsequent electrostatic disruption. In this context, materials with low carrier mobility and weak electronic screening, such as wide bandgap dielectrics, readily support the development of strong surface electric fields sufficient to trigger Coulomb explosion [38]. Conversely, in metals and semiconductors irradiated with near-infrared femtosecond pulses, the high mobility of free carriers and efficient redistribution of charge inhibit the formation of the necessary field gradients. However, model predictions further indicate that, under ultraviolet nanosecond irradiation, conditions in certain semiconductors may permit the onset of Coulomb explosion due to the altered dynamics of charge generation and transport [39].

1.2.2.4 Thermalization

Upon absorption of femtosecond to picosecond pulses, materials enter a highly non-equilibrium state where electrons are rapidly excited and initially thermalize through electron-electron interactions (see Fig. 1.4 for time scales of the electronic excitation processes). This is followed by a slower energy transfer to the lattice via electron-phonon coupling, as described in the foundational two-temperature model (TTM) [40]. However, recent theoretical and experimental studies have revealed that this conventional model is often insufficient. The phonon subsystem may remain internally non-thermalized for several picoseconds, forming a bottleneck that limits overall electron cooling and thus prolongs elevated electronic temperatures [41, 42]. Similar effects have been observed in bismuth, with relaxation dynamics strongly dependent on excitation fluence [43]. This persistent electronic excitation can significantly influence the onset of damage, especially in semiconductors and dielectrics. Carr et al.

showed that the energy deposited in wide-bandgap materials during damage leads to local temperatures consistent with blackbody emission, implying thermal equilibrium within the damage plasma. This condition develops only after extensive electron-lattice interaction [44]. In metals, non-equilibrium electron distributions can directly exert stress on the lattice, leading to deformation or fracture, where damage thresholds are exceeded before melting occurs due to stress accumulation from hot electrons [45, 46].

1.2.3 Absorption evaluation methods

One of the most popular techniques to measure the nonlinear absorption is using the Z-scan method [47], implementing the transmission-reflection technique. This method enables the evaluation of nonlinear refractive index, multiphoton, and linear absorption constants from the absorptance measurements, especially in very thin films [48]. Ganeev et al. [49] reported nonlinear absorption coefficient values for various media, including semiconductors, metals, and crystals at 1064 nm and 532 nm wavelengths. Correa et al. proposed theoretical formulae to fit two–, three–, four–, and five–photon absorption processes with Z-scan [50]. Nagaraja et al. investigated the nonlinearity of ZnO thin films annealed at different temperatures on quartz substrates using CW He-Ne laser radiation [51]. They observed that the nonlinear coefficient increases with annealing temperature but decreases with intensity. Zeyada et al. noticed that the nonlinear absorption coefficient of α-PbO_2 increases with photon energy but, contrary to Ref. [51], decreases with annealing temperature [52]. Razskazovskaya et al. measured and calculated two-photon-absorption (2PA) coefficients for dispersive dielectric multilayer coatings (HfO_2/SiO_2, Ta_2O_5/SiO_2) [32], revealing that the multilayer structure significantly influences nonlinear absorption. Chen et al. measured 2PA and 3PA for HfO_2, SiO_2, and Al_2O_3 thin films and bulk material of varying thickness with 515 nm and 343 nm wavelengths [53]. It was demonstrated that absorption coefficients depend on material thickness and substrate effects, as further confirmed in Ref. [48].

Despite significant contributions to understanding absorption behavior in materials, Z-scan measurements are limited in their ability to account for thermo-optical effects arising from cumulative heating at high repetition rates. Additionally, extinction coefficients derived from Z-scan data include both scattering and absorption contributions, making it challenging to isolate pure absorption losses [54].

Beyond Z-scan, alternative absorptance measurement techniques provide further insights. Apel et al. used an ArF laser calorimeter at 193 nm to measure nonlinear absorptance in Al_2O_3 films of different thicknesses, showing that nonlinear absorption cannot be described by a single coefficient across varying thicknesses and coating deposition methods [30]. However, since this

method records absorptance after several minutes of laser exposure, it may yield inaccurate results due to prolonged sample modification.

Photothermal absorption measurement techniques have become more popular recently due to their ability to dissociate from the scattering losses and enable high-power, high-repetition rate laser sources. Papernov et al. employed photothermal heterodyne imaging (PHI), a pump-probe technique, to study time-dependent absorptance changes in HfO_2 films coated on 500 nm SiO_2 [55]. They observed a decrease in absorptance over time, attributed to local laser annealing in the exposed area. A similar annealing effect was noted in Ref. [56]. Laser-induced deflection [54], lock-in thermography [57] There are other photothermal absorptance measurement techniques [54, 57], photothermal microscopy [58] have been used to evaluate the MPA and nonlinear absorption coefficients in a variety of materials. However, although they enable precise nonlinear absorptance measurements, they remain time-consuming and lack temporal resolution.

1.2.4 Intrinsic, atomic-level defect-driven damage

Atomic-scale laser-induced damage initiation mechanisms can be classified into two subcategories: native (inherent) defect-driven damage and laser-induced defect-driven damage, both of which play a crucial role in determining the response of a material to laser irradiation, particularly under ultrashort pulse durations. One of the most extensively studied materials in this context is amorphous silica (also known as fused silica). Therefore, in this section, SiO_2 will be used as a representative material to describe the mechanisms and consequences of defect formation.

1.2.4.1 Native point defects

Native point defects are commonly present in dielectric materials and play a significant role in their optical, electronic, and structural properties. These defects manifest themselves as missing oxygen atoms (oxygen vacancies), atoms with incomplete bonding (such as silicon or oxygen atoms that are not fully connected to their usual number of neighbors), or foreign impurity atoms embedded in the structure.

Native point defects in amorphous silica (SiO_2) arise from the disordered nature of its glass network, which lacks long-range atomic order and features a wide range of Si–O–Si bond angles and ring sizes – including small, highly strained three-membered rings. These strained configurations create unstable regions in the structure that are more likely to form defects, even in high-purity materials. From a thermodynamic perspective, such defects can form during the rapid cooling (quenching) of molten silica, which prevents atoms from settling into a fully relaxed and stable arrangement. On the kinetic side,

the low mobility of atoms in the solid glass phase means that once these defects form, they tend to remain trapped in place.

Among the most important native defects are the silicon dangling bond, known as the E′ center (denoted as $\equiv Si^{\bullet}$), and the non-bridging oxygen hole center (NBOHC, denoted as $\equiv$ Si–$O^{\bullet}$) [59]. The E′ center involves a silicon atom bonded to only three oxygen atoms, instead of the usual four found in a complete SiO_4 tetrahedron. This missing bond leaves an unpaired electron in a dangling bond, creating a reactive and electronically active site. The E′ center absorbs light around 5.8 eV and serves as a deep trap for electrons, strongly affecting the optical and electrical behavior of the material [59]. In contrast, the NBOHC forms when a Si–O–Si bond is broken, leaving an oxygen atom bonded to only one silicon atom. This type of oxygen atom holds a localized hole, forming an $O^{\bullet}$ center that emits visible light (photoluminescence) at around 1.9 eV [60]. Hydroxyl groups (Si–OH) are another source of structural instability, acting as precursors to NBOHCs, especially when exposed to vacuum ultraviolet (VUV) radiation that can break the Si–OH bond [61].

Both E′ centers and NBOHCs introduce electronic states within the bandgap of the material. These defect-related states allow the material to absorb lower-energy (sub-bandgap) or multiple photons simultaneously (multiphoton absorption). This increases the likelihood of energy absorption during intense laser irradiation, effectively lowering the threshold for laser-induced damage. Furthermore, these defects enhance local electric fields and can concentrate energy in specific regions, especially under ultrafast (femtosecond) or UV laser pulses.

1.2.4.2 Laser-induced defects

Laser-induced defects in silica emerge from the interaction of high-intensity or high-energy laser pulses with the material's lattice, leading to electronic excitation, bond-breaking, and structural rearrangement. In Si–OH-rich ('wet') silica, photons with energies around 7.9 eV – such as those from an excimer laser – efficiently break Si–OH bonds, forming NBOHCs and atomic hydrogen (H). However, due to the high mobility of hydrogen, many of these defects recombine and annihilate shortly after formation, limiting their accumulation [61]. In contrast, in Si–OH-deficient ('dry') silica, defects primarily form through the photo-induced breaking of strained Si–O–Si bonds, producing both NBOHCs and silicon dangling bonds (E′ centers), which exhibit significantly lower recombination rates.

A critical intermediate in forming these defects is the self-trapped exciton (STE) – a localized bound state of an electron and hole, stabilized by local lattice distortion. STEs form extremely rapidly in fused silica, with formation times of 150 fs, due to strong electron-phonon coupling following multiphoton excitation [62, 63]. While their formation is ultrafast, STEs persist for

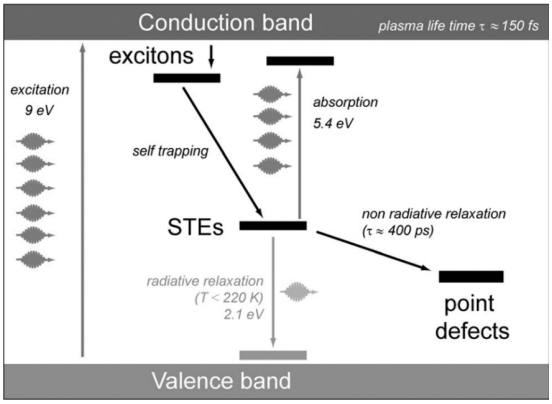

Figure 1.6: Schematic energy diagram of the STE formation inside fused silica and their decay to semi-permanent point defects [63].

relatively long durations – typically several hundred picoseconds – before decaying. At room temperature, this decay is predominantly non-radiative. It can lead to the creation of stable point defects such as E′ centers and NBOHCs (a schematic view of the defect formation process is illustrated in Fig. 1.6) [63]. The presence of pre-existing defects or strained regions in the lattice significantly enhances the likelihood of such STE-induced transformations. Because STEs have lifetimes long enough to outlast a single pulse and interact with subsequent ones, their formation becomes increasingly efficient under repeated laser exposure. This behavior is particularly relevant in femtosecond laser regimes, where high peak intensities and ultrashort pulse durations facilitate efficient energy deposition within sub-picosecond time windows [10, 64, 65].

As laser pulses accumulate, so do the defects they generate, even when the fluence is below the single-shot LIDT – a phenomenon known as incubation. This progressive defect accumulation modifies the local electronic structure and optical response, often enhancing absorption and field localization. Over time, such changes degrade material performance. More broadly, laser-induced defects contribute to both non-catastrophic damage modes, such as localized color changes, and to the initiation of catastrophic breakdown, underscoring their importance in both material degradation and functional laser processing.

1.2.5 Extrinsic, macro-defect driven damage

Larger-scale imperfections – either inclusions introduced during manufacturing or formed during operation – can localize laser energy and lead to catastrophic failure. These macro defects arise from manufacturing processes such as grinding, polishing, and coating deposition. Sub-surface damage (SSD), polishing-induced cracks, and residual stress zones often lie beneath a Beilby layer formed during the final polishing step [66]. These defects act as energy concentrators,

amplifying local electric fields and significantly lowering the LIDT [66, 67]. Coating-related defects, particularly nodular defects, originate from particulate contamination or surface flaws and grow into conical inclusions during deposition. The dome-like tops of these nodules act as micro-lenses, focusing light and initiating localized breakdown [68]. Upon irradiation, nodules often delaminate due to weak adhesion, creating voids that grow with continued exposure.

1.3 Laser-induced fatigue

Almost all laser systems, except for extremely high-energy facilities such as NIF [4] or LMJ [69], operate below the single-pulse LIDT. However, optical damage has been reported after hundreds or thousands of hours of operation [70, 71]. The fatigue effect and the associated optical lifetime remain not fully understood. Yet, they are critical for the development of long-lasting optical components that ideally would not degrade under laser irradiation. There are several fatigue explanation theories that will be discussed in the following sections.

1.3.1 Thermal and mechanical fatigue

The thermal energy delivered by a single pulse requires time to dissipate within the material. However, with multiple pulses, heat can accumulate if the heat diffusion time of the material exceeds the pulse duration. The typical heat diffusion time for glasses is on the order of μs [29]. As the material temperature rises, damage can occur due to mechanical failure, surface melting, or a combination of both [12]. This type of fatigue is particularly relevant for CW lasers [29] and pulsed lasers operating at high repetition rates in the MHz range [7]. Additionally, thermal fatigue can manifest in highly absorbing defects and inclusions [67, 72]. Highly absorbing coatings may also experience gradual laser-induced fatigue due to repeated thermal-mechanical cycling, which causes microstructural changes and eventual failure. Thermal cycling fatigue is mainly caused by the mismatch of thermal expansion between different material layers or localized defects [73], leading to delamination and blistering at the coating-substrate interface [74].

1.3.2 Material modification-induced fatigue

As discussed in previous sections, laser-matter interaction can modify material properties by altering the intrinsic structure of the material. For ultrashort pulses (<20 ps), nonlinear electronic effects such as MPA and AI become dominant [10, 12]. In interference coatings, multiphoton absorption and avalanche ionization cause bond breaking and incubation of lattice defects. These effects

occur when valence electrons are excited to the CB. After excitation, a significant fraction of free electrons relax into STE states, which may further decay into point defect states such as color centers [63], as discussed in Sec. 1.2.4. These processes cause material degradation by forming mid-gap states that, upon repetitive excitation, reduce the damage threshold [12, 75].

1.3.3 Laser-induced contamination

Environmental factors may also influence the operational lifetime of optical components. Organic contaminants in the surrounding environment can settle on optical surfaces and reduce their damage threshold during long-term laser exposure [70, 76–78]. This phenomenon, known as laser-induced contamination (LIC), has emerged as a critical factor limiting both the LIDT and the longevity of optics in high-power laser systems [78, 79]. LIC involves the deposition of nanometer-scale, highly absorbing layers on optical surfaces as a result of complex interactions between high-intensity laser beams and volatile organic compounds present in the environment. These contaminants, often originating from out-gassing materials or airborne molecules, undergo photochemical reactions under laser irradiation, leading to the formation of low-volatility films that significantly alter the optical properties of surfaces [79, 80]. Even when optics exhibit high intrinsic LIDT values, LIC can induce localized absorption and heat accumulation, effectively reducing the practical damage threshold and initiating irreversible damage such as micro-cracking or delamination over time [81]. Such degradation is particularly accelerated in high-repetition-rate systems, where cumulative effects from millions of pulses can cause damage growth from initial defects enhanced by contamination-induced absorption [79]. Furthermore, studies have shown that contamination layers composed of carbonate or siloxane derivatives can drastically increase absorption and scattering losses, ultimately leading to catastrophic optical failure [82, 83]. The impact on laser system lifetime is twofold: first, the reduced transmission or reflection efficiency leads to power loss and system instability; second, once contamination-driven damage initiates, the affected component must be cleaned or in worse case – replaced, incurring downtime and maintenance costs. This necessitates precise material selection, environmental control, and the implementation of real-world testing protocols that emulate operational conditions to predict component longevity accurately [81, 84].

1.3.4 Overview of fatigue characterization methods

Characterization of the fatigue effect is critical to predicting the lifetime of optical materials. However, it is challenging and requires extensive experimental data, long-duration laser exposure, and appropriate predictive fatigue models. Short-term fatigue effects can be measured using the S-on-1 (series of pulses

on one test site) method [11], which provides a characteristic damage curve (typical fatigue curve is illustrated in Fig. 1.7), indicating LIDT as a function of the number of pulses. The S-on-1 LIDT is typically much lower than the 1-on-1 (single pulse on one site) threshold. The characteristic damage curve can also be used to estimate the long-term effects of fatigue and the lifetime of the optics when combined with an appropriate extrapolation model, which is unknown in the general case.

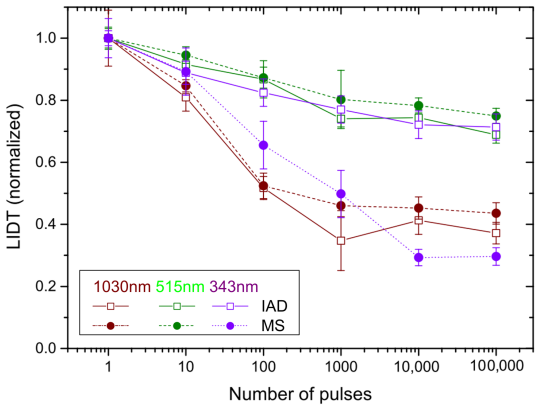

Figure 1.7: S-on-1 LIDT measurements made on the two differently deposited Nb_2O_5 thin coatings (IAD: ion-assisted deposition; MS: magnetron sputtering) [85].

Most of the previous studies focus on catastrophic damage and suggest pertinent fatigue models, demonstrating that LIDT tends to saturate after a certain number of pulses, reaching the so-called LIDT onset [8, 86] — a threshold below which no damage occurs. For example, Mero et al. [75] proposed a phenomenological model to describe the LIDT fatigue behavior in dielectric films subjected to femtosecond multipulse irradiation. Their approach linked the damage threshold decrease to the accumulation and ionization of STEs, which form after multiphoton excitation and relax into long-lived defect states. The damage threshold was observed to decrease with pulse number and saturate after a certain number of pulses, independent of repetition rate, indicating that material relaxation between pulses was negligible. The model, based on rate equations (see Sec. 1.2.2.2) for electron dynamics in CB and STE generation, successfully reproduced experimental observations of LIDT fatigue behavior and associated temperature rise. Emmert et al. [87] developed a more detailed rate equation model that incorporated both native and laser-induced defect states (see Sec. 1.2.4) to explain LIDT fatigue. In their model, CB electrons were generated by direct MPI and ionization of mid-gap trap states. It was emphasized that AI, seeded by traps, dominated the breakdown process at longer pulse durations. The model distinguished between shallow and deep trap

populations and showed that laser-induced defects could account for the gradual threshold reduction over hundreds of thousands of pulses. The approach also demonstrated that the trap parameters (density, ionization cross-section, relaxation rates) strongly influence the fatigue curve. The international ISO standard for LIDT provides an empirical expression for the multipulse damage threshold [11]:

$$F_{\mathrm{th}}(S) = F_{\mathrm{inf}} + \frac{F_1 - F_{inf}}{1 + \frac{1}{\Delta}\log(S)} \tag{1.9}$$

where F_1 is the single-shot damage threshold value, F_{inf} is the resistance limit of the optical surface, and Δ describes the decrease of the characteristic damage curve with the increasing number of pulses S. These parameters are typically calculated using the least-squares approximation method. Recently, lifetime evaluation has been explored using a Bayesian inference approach [88]. By integrating experimental damage data with probabilistic modeling, this method refines damage threshold estimations and provides a robust statistical framework for reliability assessments. There are multiple other empirical lifetime extrapolation functions, derived based on the material fatigue behavior [89–92]. However, these models are typically tailored to specific materials or behaviors and do not fully account for the underlying physical mechanisms of fatigue.

1.4 LIDT scaling laws

There are a lot of various laser systems with different output parameters. The LIDT of a certain optical element depends on various irradiation parameters such as wavelength, beam diameter, time, history of exposure, pulse repetition rate, and pulse duration, as well as material properties and its synthesis method. Each parameter affects the damage threshold or optical lifetime differently, highlighting the necessity of scaling laws.

1.4.1 Pulse duration scaling

1.4.1.1 Glasses and dielectric coatings

Laser pulse duration is known to be one of the most critical parameters affecting laser damage performance. Various studies [6, 13, 15, 29, 71, 93–104] were conducted on glasses and dielectric coatings, and reported the LIDT dependence on pulse duration. According to the present knowledge, nonlinear absorption and ionization, as well as fatigue processes, govern the damage threshold of optics in a pulsed regime. Stuart et al. [6] investigated LIDT scaling laws of fused silica substrates, multi-layer dielectric at IR (λ = 1053 nm) and VIS (λ = 526 nm) wavelengths within 140 fs – 1 ns pulse durations. It was experimentally demonstrated that catastrophic multi-pulse LIDT of dielectrics scales

with pulse duration as $\sim \tau^{0.5}$ for the entire ps – ns pulse duration range, while for shorter pulses this scaling law deviates (see Fig. 1.8a)). LIDT scaling was further investigated in the femtosecond regime by Lenzner et al. [93] and Mero et al. [94] for dielectrics and single-layer coatings. Experiments carried out with $\lambda = 800$ nm wavelength indicated $\sim \tau^{0.3}$ dependence below ∼20 ps as well as direct correlation with bandgap.

Multiple other studies seem to reproduce $\tau^{0.3} - \tau^{0.5}$ scaling laws [13, 15, 71, 97–104]. For pulses longer than a few μs, LIDT is no longer governed by the electronic processes but rather thermal heating and melting, as Bliss [95] and Wood [29] demonstrated. Thus, a thermal balance between deposited and dissipated power defines the damage threshold of the optical element. In the CW regime, it is more convenient to use irradiance as a threshold unit (W/cm^2 – average power per effective area) as it remains constant while changing pulse duration. Constant threshold irradiance scales linearly with pulse duration when converted to units of fluence (see Fig. 1.9).

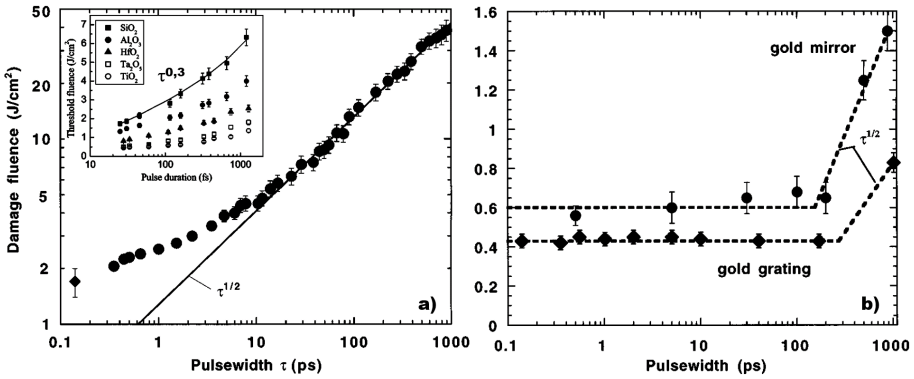

Figure 1.8: Pulse width dependence of threshold damage fluence for a) fused silica at 1053 nm [6] (the inset shows the pulse width scaling in 10 – 2000 fs at 800 nm for several dielectrics [94]) and for b) gold coating and grating [6].

1.4.1.2 Metals and metallic coatings

Studies on LIDT scaling laws on pulse duration are limited for metallic coatings. Historically, the high absorptance of metallic coatings resulted in a relatively low LIDT compared to dielectric coatings, restricting their use in high-power applications. Consequently, metallic coatings have been primarily employed in low-power imaging [105], spectral analysis [106, 107], and sensor applications due to their broadband reflectivity, cost-effectiveness, and surface plasmon resonance properties [108]. Apart from gold coatings on polished copper optics in CO_2 lasers, metallic mirrors have been largely replaced by dielectric multilayer coatings in high-power laser systems. In a previously mentioned study by Stuart [6], LIDT scaling on gold coating and grating was also evaluated

(see Fig. 1.8b)). It was demonstrated that the LIDT is independent of pulse duration in the fs – ps range, while for nanoseconds it scales as $\tau^{0.5}$. Only a few other investigations have explored LIDT scaling with pulse duration in metals and metallic coatings. The complexity arises from the simultaneous influence of multiple material parameters. Wood theoretically estimated (the model will be presented in Sec. 3.1) that LIDT scales linearly with pulse duration in the CW regime (see Fig. 1.9). In contrast, in the pulsed regime, it is independent of the pulse duration [29], contradicting the study by Stuart et al. Sparks et al. [109] examined copper and aluminum films with 100 ns pulses and gold and silver films with 150 ps pulses, showing that the LIDT depends on various parameters such as pulse length, pulse shape, number of pulses, and optical properties (e.g., absorption and reflectivity). Furthermore, LIDT was found to be linearly dependent on coating thickness up to the optical penetration depth, after which the threshold approaches the bulk material damage threshold, particularly for pulses ranging from 200 fs to 10 ps [110, 111]. Under the investigated conditions, the effect of coating thickness on LIDT became minimal for coatings thicker than 50 – 500 nm, depending on the material being studied.

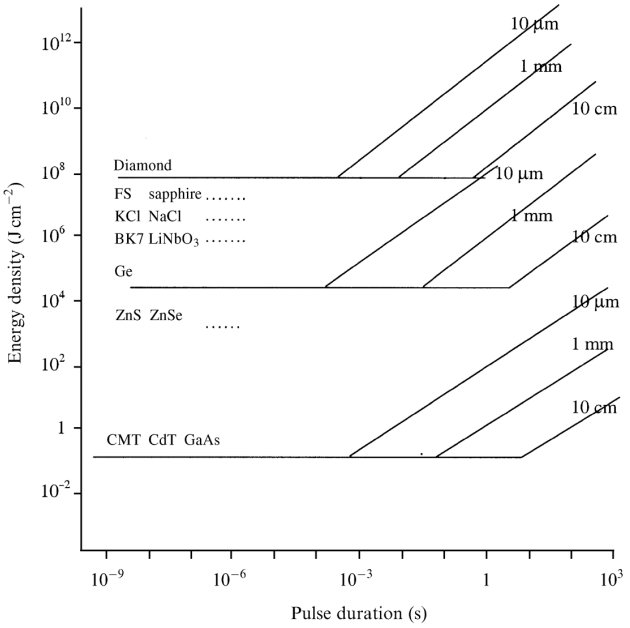

Figure 1.9: Thermally induced LIDT as a function of pulse duration and beam diameter [29].

The LIDT scaling with pulse duration is also important for micro- and macro-machining [112, 113]. Ablation studies have partially confirmed the predictions by Wood, showing that in the 500 fs – 10 ps range, the ablation

threshold exhibits only a weak dependence on pulse duration for materials such as copper and silicon [114]. Similar trends were observed for aluminum, copper, nickel, and tungsten in the 15 – 100 fs regime [115], although scaling laws were not explicitly stated in some studies [116, 117]. In contrast, Hashida et al. [118] showed that in the 70 fs – 5 ps range, the ablation threshold scales with the pulse duration as $\tau^{0.25-0.67}$, depending on the ablation depth. Y. Zhu et al.[119] recently reported opposite dependence in SiO_2-coated aluminum mirrors at 1030 nm wavelength, with pulse widths ranging from 0.2 ps to 11 ps, indicating that the LIDT deviates from the square root scaling law ($\tau^{-0.063}$) as the pulse width decreases below 10 ps.

1.4.1.3 Nonlinear crystals

The LIDT scaling with pulse duration in nonlinear crystals has been less extensively studied. However, several notable investigations provide valuable insights. For example, the bulk damage threshold of uncoated KDP crystal was found to scale with $\sim \tau^{0.3}$ for 250 ps – 16 ns pulses at IR [120, 121] and UV [122] wavelengths. Furukawa et al. performed single-shot LIDT measurements in LBO bulk material [71] at 1064 nm, 532 nm, and 355 nm wavelengths. They reported $\sim \tau^{0.45}$ LIDT dependence on pulse duration and noticed that shorter wavelength also results in lower LIDT.

1.4.2 Beam diameter scaling

Both thermal damage (CW lasers) and electronic damage (pulsed lasers) in transparent media are influenced by the laser beam diameter [29]. Generally, the LIDT scales inversely with the square of the beam radius, following a $1/\omega^2$ dependence [123]. This effect is particularly pronounced for nanosecond pulses due to the probabilistic nature of damage initiation, which depends on the likelihood of encountering pre-existing defects within the irradiated area. Experimental studies on single-layer HfO_2 coatings confirm that LIDT increases with decreasing beam diameter [9, 123], as smaller beams are statistically less likely to intersect damage-initiating defects [67, 124]. Above a certain beam size ($\sim$250 – 350 μm), the threshold tends to plateau, reflecting a saturation in defect sampling [125].

In contrast, damage becomes more deterministic for ultrashort pulses (fs – ps regime), governed primarily by nonlinear ionization rather than defect-assisted absorption. Sanner et al. showed that in fused silica irradiated with 450 fs pulses, LIDT decreased with increasing beam diameter in the 0.8 – 10 μm range [126]. This trend arises because smaller beam waists concentrate peak intensity, reducing the influence of sub-micron defects and allowing the intrinsic material threshold to dominate. Although ultrashort pulses reduce statistical variation in damage onset, beam diameter still affects measured thresholds and

must be considered in experimental design and data interpretation.

1.4.3 Wavelength scaling

The LIDT of optical materials exhibits a pronounced dependence on the irradiation wavelength, reflecting underlying differences in material response mechanisms at varying photon energies. Generally, a decrease in wavelength, corresponding to an increase in photon energy, reduces the LIDT. This trend is attributed to enhanced linear and multiphoton absorption processes at shorter wavelengths, facilitating the initiation of defect states and material breakdown. In the case of nonlinear optical crystals such as LBO, long-term exposure to UV radiation at 355 nm – even at intensities well below the nominal LIDT – induces surface degradation processes not observed under infrared or visible illumination [82, 127]. Specifically, UV light promotes photo-assisted chemical reactions at the surface, forming amorphous layers on the crystal surface, such as SiO_2, from environmental contaminants. These secondary layers substantially modify the surface optical properties and eventually precipitate catastrophic damage. Similarly, for dielectric thin films, systematic studies under fs – ps multipulse irradiation at UV – IR wavelengths demonstrate a distinct wavelength dependence of LIDT, with damage thresholds decreasing at shorter wavelengths [85, 101]. The observed behavior is linked to the lower number of photons required to bridge the bandgap energy at higher photon energies, thus increasing the probability of nonlinear absorption mechanisms like multiphoton ionization and avalanche breakdown. Additionally, the incubation effect becomes more pronounced at UV wavelengths due to increased absorption cross-sections for defect states. Moreover, UV-induced damage processes are often amplified in high-power, high-repetition-rate systems, where thermal effects, material impurities, and surface quality become critical factors.

1.5 Discussion

Despite considerable progress in studying laser-induced damage, critical gaps persist in understanding how damage evolves under practical, long-term laser operation. While catastrophic damage mechanisms are relatively well established, current LIDT scaling laws are often limited to idealized single-shot or low-pulse-count conditions. These models often fail to capture the full complexity of multipulse exposure scenarios common in real laser systems. Moreover, studies frequently report inconsistent scaling exponents, indicating the need for broader experimental validation and more robust theoretical frameworks.

A major limitation is the persistent focus on catastrophic damage, while non-catastrophic damage modes in the scientific literature, such as color change, remain under-represented. These forms of damage occur below the catas-

trophic threshold and may evolve gradually, yet their onset mechanisms, long-term behavior, and influence on optical performance remain poorly understood. Color change, for example, is often attributed to the formation of color centers through multiphoton ionization. However, it remains unclear whether the formation of color centers is the only possible mechanism, whether an LIDT onset for color change exists, and whether multiphoton ionization alone determines color change formation.

Equally underdeveloped are models for optical lifetime prediction. Current approaches rely on short-term S-on-1 tests and empirical extrapolation, often neglecting the complex defect accumulation dynamics observed under prolonged exposure. While some studies, such as those by Mero et al. and Emmert et al., have proposed fatigue models based on rate equations and trap density evolution, they do not account for sub-catastrophic degradation. There is no widely accepted predictive model that connects short-term fatigue data to reliable, long-term lifetime estimates across materials and laser conditions.

In parallel, nonlinear absorption – particularly multiphoton absorption – is recognized as a key initiator of damage in transparent optical materials, yet temporal absorption dynamics remain poorly resolved. Standard methods like Z-scan and calorimetry provide spatially integrated, time-averaged data and cannot capture the evolution of real-life absorption. This lack of temporal resolution is a major obstacle to connecting absorption behavior directly to damage initiation and LIDT, especially in fs – ps regimes where the energy deposition is highly dynamic.

Although significant advancements have been made in laser-induced damage studies, key uncertainties remain regarding damage evolution under realistic, long-term irradiation conditions. The absence of scaling laws that account for sub-catastrophic modes, the scarcity of reliable long-term fatigue models, and the limited temporal characterization of absorption all point to a need for deeper physical insight and expanded experimental scope. Bridging these gaps is essential for developing predictive models and improving the resilience of optical coatings in high-intensity laser applications.

2. Experimental methods and characterization techniques

This Chapter consists of a list of laser sources used in all experiments, summarized by publication chronology and laser beam diagnostics, LIDT evaluation protocols, as well as LIDT and absorption testing setups and techniques.

2.1 Laser sources and beam diagnostics

A broad range of laser sources was employed to investigate LIDT and absorption characteristics in various dielectric, metallic, and semiconductor coatings, covering pulse durations from 10 fs to 10 s.

For LIDT experiments in [**A1**], three pulsed lasers were used at 1 kHz repetition rate and beam diameter ranging from 29 to 35 μm at $1/e^2$ level:

- a Legend (Coherent) amplifier with HE-TOPAS OPO (Light Conversion) generating 50 fs pulses at 1064 nm and 355 nm;
- a Yb:KGW Pharos laser (Light Conversion) for 200 fs – 10 ps pulses at 1030 nm and 343 nm with external harmonic generation;
- an Atlantic 80 (Ekspla) laser for 10 ps – 9 ns pulses at 1064 nm and 355 nm, with third harmonic generation achieved internally (10 ps) or externally (150 ps and longer) and subsequent harmonic filtering.

LIDT tests in [**A3**] were performed using the Pharos laser at 1030 – 257 nm with external harmonic generation, 10 ps pulse duration, and 50 kHz repetition rate, with a focused beam diameter of approx. 60 μm at $1/e^2$ level.

LIDT tests on metallic and semiconductor coatings in [**A4**] were performed at 100 Hz repetition rate and beam diameter at approximately 200 μm at $1/e^2$ level with:

- a NAGLIS OPCPA system [128] delivering 9.5 – 10 fs pulses at 1030 nm (beam diameter was 100 μm at $1/e^2$);
- a Pharos laser for 200 fs – 10 ps pulses at 1030 nm and 343 nm using external harmonic generation;
- an injection-seeded Nd:YAG laser (Innolas) for 9 ns pulses at 1064 nm;
- an Yb-doped fiber laser (IPG Photonics) for CW exposures from 1 ms to 10 s at 1070 nm.

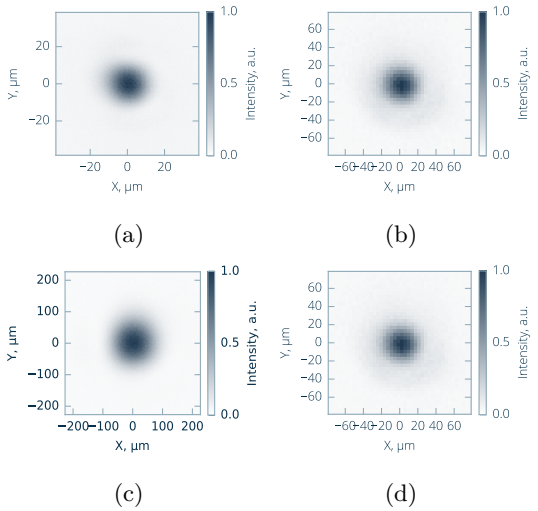

Figure 2.1: Typical beam diameter profiles used in LIDT measurements across all pulse durations and wavelengths: (a) 1064 nm in **[A1]**, (b) 355 nm in **[A3]**, (c) 1064 nm in Sec. 3.1, (d) 355 nm in Sec. 5.2.

To ensure the comparability of LIDT data across the full range of pulse durations, irradiation conditions were carefully controlled despite the use of three different laser systems. At 10 fs, where a smaller beam diameter of ∼100 µm was used, the obtained LIDT values aligned with the overall trend (see Sec. 3.1), indicating negligible beam size influence.

LIDT tests **[A5]** were performed using the Atlantic 80 laser at 355 nm with internal harmonic generation, 10 ps pulse duration, and 1 MHz repetition rate, with a focused beam diameter of approx. 60 μm at $1/e^2$ level.

Absorptance measurements were carried out employing lasers operating at 1 MHz with a beam diameter ∼60 μm at $1/e^2$ level:

- a 10 ps pulsed Atlantic 80 laser at 1064 nm, 532 nm, 355 nm using internal harmonic generator, and 266 nm with an external harmonic generation in **[A2]** and **[A3]**;
- an Yb:KGW Pharos laser (Light Conversion) for 170 fs – 2 ps pulses at 343 nm with an internal harmonic generator in **[A5]**;
- a low-power CW HeNe probe at 633 nm was used to detect thermal lensing via modulation of the interference pattern in **[A2, A3, A5]** and Section 4.2.

Beam diameters in all experiments were measured after focusing optics and light attenuation with appropriate filters in the focal plane using a Chameleon CCD camera (CM3-U-13S2M-CS, FLIR) with a pixel size of 3.75 μm. Typical

beam diameter profiles at $1/e^2$ level used in LIDT and absorption experiments are illustrated in Figs. 2.1 and 2.2, respectively.

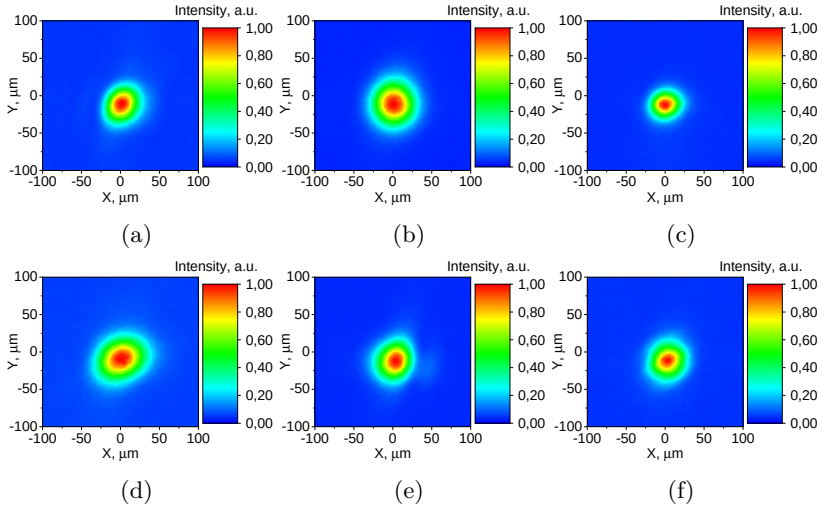

Figure 2.2: Typical beam diameter profiles used in absorption evaluation experiments with Atlantic laser at (a) 1064 nm, (b) 355 nm, (c) 266 nm, and with Pharos laser at (d) 1030 nm, (e) 343 nm, and (f) 257 nm.

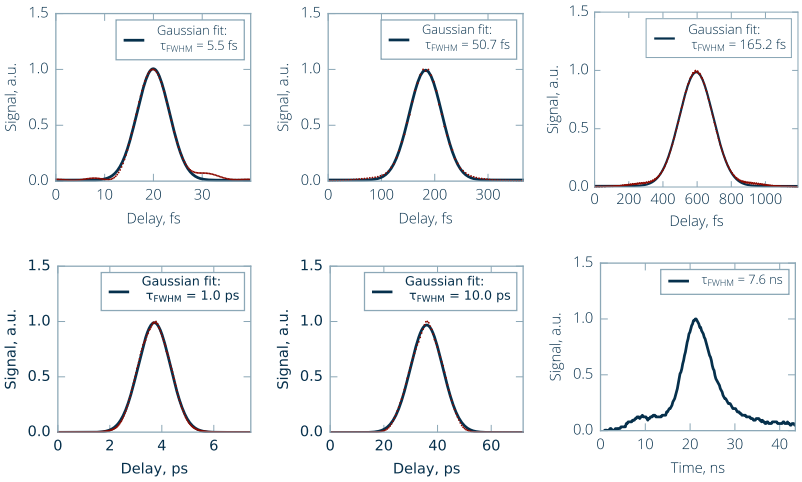

Figure 2.3: Typical temporal pulse shape and measured pulse durations used in experiments.

Various pulse durations were used during the experiments in this dissertation; therefore, several pulse duration evaluation methods were employed (typical pulse duration functions are summarized in Fig. 2.3). An 8 fs pulse duration was measured using the chirp-scan method [129]. Auto-correlation

functions for pulse durations in the range of 50 fs to 10 ps were measured using the Geco (Light Conversion), while longer pulses from 150 ps to 10 s were characterized with an oscilloscope. CW pulse widths showcased a rectangular shape.

2.2 LIDT metrology

Implementing a standardized LIDT measurement protocol, such as the one outlined in ISO 21254 [11], is essential for the reliable evaluation of optical components. ISO 21254 provides comprehensive guidelines for determining LIDT, ensuring consistent and comparable results across different laboratories and applications. This standardization is crucial for assessing the durability and performance of optics in various laser systems. By adhering to ISO 21254, manufacturers and users can confidently evaluate the resistance of optical components to laser irradiation, thereby enhancing system reliability and performance.

There are several LIDT testing protocols, each serving a different purpose for the LIDT evaluation. Typically, the sample is divided into a virtual test site matrix for each testing protocol. Every site is visually inspected using a Nomarski differential interference contrast (DIC) microscope before and after irradiation. Typically, in each testing protocol, the test starts with the lowest fluence where no damage is observed and increases (linearly or nonlinearly) until all irradiated sites exhibit damage. The subsequent sections discuss each LIDT measurement protocol in more detail.

2.2.1 1-on-1 testing

1-on-1 is a measurement protocol designed to estimate single-shot laser damage at individual test sites. For each fluence level, at least 10 distinct test sites are used, with a minimum spacing of three beam diameters to prevent interference from potential debris or laser annealing. The probability of damage at each fluence level is determined as the fraction of damaged sites relative to the total tested sites. This probability is then plotted as a function of the incident fluence, and the LIDT is extrapolated by identifying the fluence at which the damage probability is zero. While useful for a rough LIDT estimation, the 1-on-1 method can overestimate the threshold when defect density is low and the beam diameter is small. Additionally, it does not account for laser-induced fatigue or incubation effects, which are relevant for multi-pulse irradiation scenarios.

2.2.2 S-on-1 testing

S(series)-on-1 is a standard LIDT measurement technique (as per ISO 21254) employing a certain number of pulses for a single test site. The testing procedure is similar to 1-on-1 testing, except here each site is additionally monitored by an online scattering diode, which can record the moment the damage occurs. The irradiation is terminated upon detection of catastrophic damage or after the completion of pulses without detecting damage. After laser exposure, the test sites are monitored with an offline microscope. Following the damage inspection, the damage probability for each pulse class is calculated and plotted as a function of the number of pulses. This provides a characteristic damage curve, indicating the damage LIDT behavior at different exposure times. Often, the results of S-on-1 measurement are extrapolated to estimate the optical lifetime of optics. The ISO provides an LIDT extrapolation function. However, it is not applicable in all real-life scenarios. Interpretation and extrapolation of S-on-1 results are one of the main topics of this thesis and will be discussed in later chapters.

2.2.3 R-on-1 testing

R(ramp)-on-1 test procedure is suited for small-aperture optics where the space for LIDT evaluation is limited. This method repeatedly irradiates the same site with increasing fluence until damage is observed. This procedure is conducted across multiple test sites, with equal fluence increment steps. The damage probability is then plotted as a function of the incident fluence. Laser conditioning effects can occur during ramping tests, leading to an apparent increase in LIDT [12]. As a result, R-on-1 is not suitable for accurate LIDT determination compared to 1-on-1 or S-on-1 tests. Instead, this protocol is primarily used to assess the extent of laser conditioning effects.

2.2.4 Raster scan testing

The raster scan measurement technique is particularly effective for assessing the influence of small defects on LIDT. National Ignition Facility (NIF) in Livermore, USA [4], has developed a widely adopted test procedure for evaluating large-aperture optics using small-aperture witness samples [130, 131]. The procedure involves a sequence of raster scans over a 1×1 cm test area, followed by localized irradiation to assess damage growth. Raster scanning is performed by moving the optics in a zigzag pattern through a stationary laser beam. The fluence of the laser beam remains fixed during each scan. Since the incident laser beam is typically circular, overlapping neighboring pulses is necessary to create a nearly uniform fluence distribution across the scanned area. Most laser beams exhibit a Gaussian intensity profile, so the scanning step size is often

set to correspond to the beam width at 90% of the peak fluence. Each scan is conducted at a constant fluence, with subsequent scans performed at increasing fluence levels until the required fluence specification for the optics is reached. A witness sample is considered to have failed if at least one of the following conditions is met:

- Damage is present at more than 1% of the test (nominally 2400) sites.
- Damage site(s) are larger than 100 μm.
- Damage which grows under further illumination (considered catastrophic damage).

2.3 Laser-induced damage testing setups

Figure 2.4 illustrates a typical LIDT testing setup used for 1-on-1 and S-on-1 experiments, conducted in accordance with the ISO 21254-2 international standard [11]. In pulsed laser LIDT tests, the laser beam is first attenuated before reaching an energy-monitoring photodiode (D1) or power meter for calibration. The transmitted beam is then focused onto the test specimen by a lens. A scattering photodiode (D2) is positioned to detect back-scattered light, which signals the occurrence of catastrophic damage. Irradiation is automatically terminated either upon damage detection or after the completion of the designated exposure sequence without observed damage. For CW LIDT tests, the sample is placed outside the fiber imaging plane to ensure a near-Gaussian beam profile. An angle of incidence (AOI) of 10° is used to prevent back-reflection into the laser power fiber. In this regime, the laser provides uniform exposure by accurately controlling the output power and irradiation time.

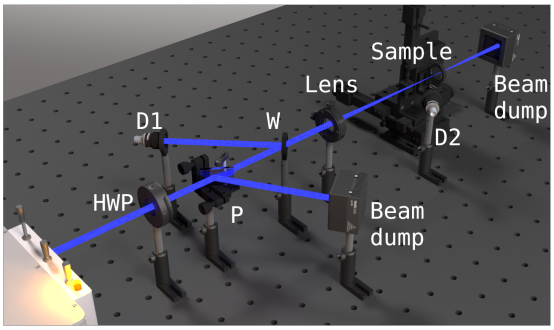

Figure 2.4: Schematic view of a standard LIDT testing system. HWP – half-wave plate, D1 – energy measuring diode, P – polarizer, W – wedge, D2 – scattering diode for damage detection.

Each measurement is carried out on a matrix of test sites, with a minimum spacing of three beam diameters between the sites to avoid cumulative effects. For reliable statistical analysis, at least 200 test sites are typically irradiated per test condition. Incident fluence is precisely controlled using a motorized attenuator and held constant for at least 10 sites before being increased in steps not exceeding 20% of the previous level. Near the damage threshold, additional fluence levels and test sites may be introduced to refine the LIDT estimation and minimize uncertainty.

Based on the analysis of irradiated sites, damage probabilities are calculated for each pulse class. For probabilistic damage, the LIDT is defined as the likelihood of damage at a given fluence or intensity. For deterministic damage, the LIDT is determined using the half-before-first-damage (HBFD) method – calculated as the average of the lowest fluence causing damage and the highest fluence not causing damage. The resulting damage thresholds are then plotted as a function of incident laser pulses, yielding characteristic damage curves for both catastrophic and color change damage modes.

2.4 Photothermal common-path interferometry

The surface absorptance of test samples is measured as a function of laser intensity using a commercial photothermal common-path interferometry (PCI) system (Stanford Photo-Thermal Solutions [132]). The system includes two laser beamlines: a low-power CW probe at 633 nm with a 200 μm focused spot and a pulsed pump beam for normal incidence exposure with a 60 – 90 μm focused spot. A schematic of the setup is shown in Fig. 2.5. The pump beam

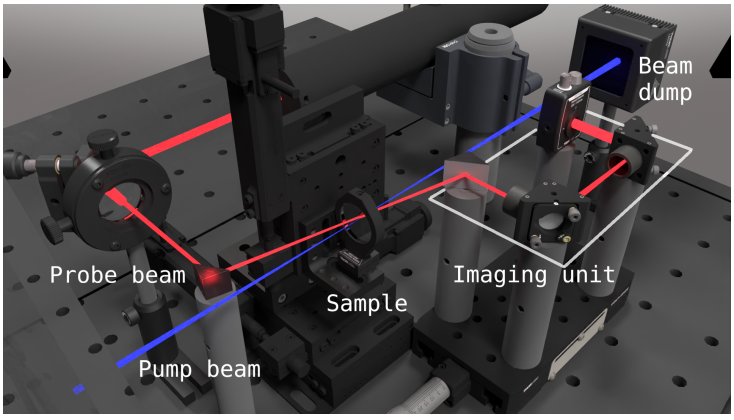

Figure 2.5: Schematic view of photothermal common-path interferometer setup. The imaging unit consists of a reflective prism, an expanding collimating telescope, and a Si detector which is connected to a lock-in amplifier.

is optically modulated at 390 Hz, creating a periodic in-time thermal lens in the sample, which is detected by the probe beam that irradiates the sample at AOI ∼10 degrees. The modulation depth of the resulting interference pattern is recorded using a Si photodiode and a lock-in amplifier. A reference sample with known surface absorptance is used for calibration.

Calibration of the PCI system means establishing the absolute absorption scale. To calibrate the system, the value of responsivity R should be estimated. It is defined as the modulation depth of the probe per unit of absorbed power (1/W):

$$R = \frac{AC_{\text{ref}}}{DC_{\text{ref}}} \frac{1}{\alpha_{\text{ref}} P_{\text{ref}}} \tag{2.1}$$

where α_{ref} is the absorptance of the reference sample, AC_{ref} and DC_{ref} are voltage signals acquired from the lock-in amplifier and photodiode, respectively, P_{ref} is the pump power at which the calibration was performed. With known R, the absorption of a tested sample can be calculated with raw data:

$$\alpha = \frac{AC}{DC} \frac{1}{P} \frac{1}{R}. \tag{2.2}$$

Two measurement protocols are employed in the absorptance experiments: transverse-scan (T-scan) and temporal measurement (Time-scan). In the T-scan, the sample is moved to measure absorptance in a fresh area along a line on the surface. Each site is exposed with a maximum of 100 ms integration time (the shortest integration time of the system is 50 ms), with a 50% overlap of the beam diameter. In contrast, the Time-scan captures the temporal dynamics of absorptance by exposing a stationary test site for a selected period of time.

2.5 Preparation of single-layer and AR dielectric coating samples

The studies in this dissertation (in publications **[A2]**, **[A3]**, **[A5]** and Section 4.2 examined several single-layer dielectric coatings deposited on 6.35 mm thick UV-grade fused silica substrates sourced from the same polishing batch. The coatings included HfO_2, SiO_2, Al_2O_3, and ZrO_2, each designed to have an optical thickness of six quarter-wave layers (6 QWOT) at 355 nm for normal incidence (AOI = 0°). Additionally, anti-reflection (AR) coatings consisting of HfO_2/SiO_2 multilayers were also investigated.

All coatings were deposited using the ion beam sputtering (IBS) technique at Optoman (Vilnius, Lithuania). Deposition occurred in a Cutting Edge Coatings GmbH IBS system, operating under high vacuum with a base pressure of 6–8 × 10^{-6} mbar. Oxygen gas was supplied during growth to ensure complete oxidation, resulting in a working pressure of 3–4 × 10^{-5} mbar. A radio-

frequency grid ion source bombarded the metallic targets (hafnium for HfO_2, zirconium for ZrO_2, and aluminum for Al_2O_3) at an angle of 55° using argon gas. Typical ion source parameters were 1650 V and 230 mA, yielding deposition rates of 0.75 – 0.8 Å/s. Film thicknesses were monitored in real time via an integrated broadband transmission optical monitoring system operating between 400 and 1000 nm, ensuring precise control of thickness.

Following deposition, coatings were subjected to three different post-processing conditions: as-deposited (room temperature, RT), and thermally annealed at either 350°C or 500°C for one hour. All annealed coatings remained amorphous, consistent with previous studies indicating hafnia crystallization occurs only above 600°C [133].

Optical characterization involved reflectance and transmittance measurements using an RT Photon spectrophotometer (Essent Optics) at near-normal incidence. The coating thickness and refractive index dispersion were extracted using Fresnel equations. By fitting the experimental spectra with virtual spectra based on Sellmeier functions, the refractive index values were obtained. The extinction coefficient and absorption coefficient were then deduced from an energy conservation relation, considering reflection, transmission, absorption, and negligible scattering. Absorption bandgap values were extracted by fitting the linear portion of the absorption edge using the Tauc method with the following expressions [52]:

$$\alpha = \frac{4\pi k}{\lambda} \tag{2.3}$$

$$\alpha h\nu = \xi(h\nu - E_g)^r \tag{2.4}$$

where α is the absorption coefficient, k is the extinction coefficient, λ is the wavelength, $h\nu$ is the photon energy, E_g is the material bandgap, $r = 1/2$ for direct allowed transitions, and ξ is a fitting parameter. The physical thicknesses, refractive indices, and bandgap values of all coatings are summarized in Table 2.1.

Table 2.1: Physical and spectral parameters of single-layer dielectric coatings and AR (@355 nm) coatings (only annealed at 350 °C).

Coating	Treatment	Thickness (nm)	Bandgap (eV)	n_{1064}	n_{532}	n_{355}	n_{266}
HfO_2	RT	261.00	4.12	1.94	1.97	2.04	–
	350°C	272.40	5.14	1.90	1.92	1.98	–
	500°C	271.65	5.20	1.88	1.92	1.99	–
SiO_2	RT	352.69	5.21	1.45	1.49	1.51	1.53
	350°C*	352.69	∼9	1.45	1.49	1.51	1.53
	500°C*	352.69	∼9	1.45	1.49	1.51	1.53
ZrO_2	RT	234.49	3.63	–	–	2.21	–
	350°C	235.24	4.65	–	–	2.19	–
Al_2O_3	RT	321.85	4.08	–	–	1.70	–
	350°C	321.85	6.63	–	–	1.68	–
HfO_2/SiO_2(AR)	HfO_2 layer	15.7	5.14	–	–	1.98	–
	SiO_2 layer	77.6	∼9*	–	–	1.51*	–

*For the annealed SiO_2 samples, the coating was indistinguishable from the substrate. Therefore, the bandgap values of SiO_2 are taken from the literature, and the thickness and the refractive indices are assumed to be unchanged after annealing.

3. Laser-induced damage threshold scaling laws on pulse duration

Laser-induced damage is a complex phenomenon influenced by a wide range of laser parameters, with pulse duration being one of the most frequently varied. Understanding the limitations of optical components with respect to exposure time and pulse duration is essential for reliable system performance. While numerous studies have explored LIDT scaling with pulse duration, most have been limited to narrow pulse duration ranges and have sometimes produced contradictory conclusions. Consequently, the development of comprehensive and consistent LIDT scaling laws remains a critical area of investigation. This chapter presents LIDT scaling results for metallic and dielectric coatings and provides an overview of the work published in [**A1**] and [**A4**], which were also presented at conferences [**C1**], [**C3**] – [**C5**], [**C8**], and [**C12**].

3.1 LIDT scaling on pulse duration in metallic coatings

Motivation

Metallic coatings were essential in the early development of laser technology – silver-coated mirrors enabled light amplification in the first ruby lasers [134]. However, their low LIDT led to their replacement by dielectric multilayers in modern high-power systems. As a result, metallic materials have been relatively underexplored in LIDT studies, particularly regarding how damage thresholds scale with pulse duration.

Recent advancements in ultrafast laser applications have renewed interest in metallic and metal-dielectric hybrid coatings. These coatings offer advantageous features such as broadband reflectivity and low dispersion over wide AOI ranges, making them especially valuable in femtosecond systems [135–137]. Despite these advantages, a limited LIDT of the metallic coatings remains a bottleneck, especially under varying exposure conditions.

To better understand the behavior of LIDT, various theoretical models have been developed. One of the first approaches is a one-dimensional heat flow calculation model described by Wood [29], where a semi-infinite medium (without coating) is assumed with temperature-independent absorption properties. While being just a first-order approximation, the model predicts that LIDT scaling for thermal damage is governed by the balance between the deposited power and the dissipated power in the CW regime and the thermal capacity of

the exposed area for pulses shorter than the heat diffusion time.

However, the applicability of this model is constrained by assumptions of stationary heat flow. More advanced modeling approaches, like the Two-Temperature Model (TTM), are needed to describe the non-equilibrium energy transfer processes that dominate under short-pulse excitation [138]. Experimental data for metallic coatings over a broad pulse duration range are scarce, making it difficult to validate the theoretical models or identify consistent material behavior. Furthermore, inconsistencies in reported data across different studies underscore the need for systematic experiments.

This study addresses these gaps by performing a comprehensive experimental investigation of LIDT scaling from femtosecond to CW pulse durations on a diverse set of metallic and semiconductor coatings. Specifically, an experimental study was conducted on seven metallic coatings (aluminum, gold, silver, tantalum, titanium, tungsten, and chromium) and two semiconductor coatings (silicon and germanium) for pulse durations ranging from 10 fs to 10 s. LIDT measurements (see Sec. 2) are performed according to ISO standards [11] using the 1-on-1 and S(1000)-on-1 protocols in the near-infrared spectral range (1030 nm, 1064 nm, 1070 nm) at 100 Hz repetition rate with beam diameters of $\sim$200 μm at $1/e^2$ level.

Materials

All coatings were deposited at the Laser Zentrum Hannover (LZH, Germany) using a Denton Desktop Pro sputtering system with two magnetrons. Borofloat® glass substrates (60 mm diameter) were coated with metallic and semiconductor layers ranging from 45 nm to 1775 nm in thickness (see Table 3.1). Metal layers were deposited via DC magnetron sputtering (sputtering current – 600 mA), and dielectric layers via RF magnetron sputtering (RF power – 144 mW). Most coating stacks include an Al_2O_3/Al adhesive layer, and the main coating material. Adhesion layers were omitted for Ge, Si, and Ti. A SiO_2 overcoat (less than 10 nm thick) was added to Ag, Al, Ta, and Ti to prevent oxidation. Coating thickness was verified by focused ion beam cross-sectioning and scanning electron microscopy imaging. Coating reflection coefficient was measured by evaluating the ratio of incident and reflected power with 1064 nm linearly polarized beam at AOI = 3-5°(scattering was neglected).

Methodology of thermal modeling

A thermal model was used to estimate the theoretical LIDT by comparing the calculated surface temperature to the metal's melting point. Gold and silver were chosen as representative materials due to their well-characterized properties, though the same method is applicable to other metals using appropriate parameters.

Table 3.1: List of material coatings, their parameters, and properties. Reflectivity (measured in this work), specific heat capacity, and melting point are gathered from various literature sources [29, 139, 140]. Deposition rate is in nm/min, h – layer thickness in nm, R – reflection coefficient (measured in this work) in %, C – specific heat capacity in J/(kgK), T_{melt} – melting temperature in °C.

Coating material	**Adhesive layer**	**Prot. layer**	**Depos. rate**	h	R	C	T_{melt}
Ag	Al_2O_3 + Al	SiO_2	3.5	45	95.11	900	962
Al	Al_2O_3 + Al	SiO_2	3.2	271	88.22	520	660
Au	Al_2O_3 + Al	-	1	292	96.4	450	1064
Cr	Al_2O_3 + Al	-	8.4	198	33.95	710	1907
Ge	-	-	5	1775	42.32	140	938
Si	-	-	5	1774	32.95	130	1410
Ta	Al_2O_3 + Al	SiO_2	2.8	686	44.93	129	3020
Ti	-	SiO_2	2.5	296	33.08	235	1725
W	Al_2O_3 + Al	-	5.05	234	59.24	320	3522

Heat-flow model

For CW irradiation, thermal diffusion must be accounted for, and the temperature rise in the stationary regime at the surface may be approximated by the equation [29]:

$$\Delta T = \frac{PA}{2\rho C r \pi D}, \tag{3.1}$$

where ΔT is the temperature difference between T_{melt} melting point and T_{init} initial temperature, P is incident power, A is absorptance, ρ is the volumetric density, C is specific heat capacity, D is the diffusivity, r is the beam radius. This means that the temperature rise of homogeneous material scales with the linear power density (expressed in W/cm). When converted to fluence ($F = P\tau/\pi r^2$), where τ is pulse width, the LIDT can be expressed as:

$$F = \frac{2\rho C D \tau (T_{\mathrm{melt}} - T_{\mathrm{init}})}{Ar}. \tag{3.2}$$

Note that threshold fluence becomes directly proportional to pulse duration and inversely proportional to beam radius and absorptance. In the pulsed regime, energy deposition is instantaneous, and thus heat conduction is negligible, leading to the temperature rise:

$$\Delta T = \frac{P\tau A}{\rho C V}, \tag{3.3}$$

where $V = \pi r^2 h$ is the irradiated volume, h is the thickness of the material. When melting is used as a damage criterion, Equation 3.3 can be rewritten for

threshold fluence, substituting power for energy ($E = Pt$):

$$F = \frac{T_{\text{melt}} - T_{\text{init}}}{\rho C h A}. \tag{3.4}$$

Consequently, the LIDT (expressed in J/cm^2) becomes constant in the pulsed regime, independent of the pulse duration or beam radius for pulses shorter than the thermal decay constant.

Two-Temperature Model

The Two-Temperature Model (model parameters are summarized in Table 3.2) [138] describes energy transfer in metals via coupled heat equations for electron T_{e} and the lattice T_{l}.

$$C_{\text{e}} \frac{\partial T_{\text{e}}}{\partial t} = \nabla(K_{\text{e}} \nabla T_{\text{e}}) - g(T_{\text{e}} - T_{\text{l}}) + S(z,t), \tag{3.5}$$

$$C_{\text{l}} \frac{\partial T_{\text{l}}}{\partial t} = \nabla(K_{\text{l}} \nabla T_{\text{l}}) + g(T_{\text{e}} - T_{\text{l}}), \tag{3.6}$$

where C_{e} and C_{l} are the electron and lattice heat capacities (J/m^{3}K), K_{e} and K_{l} are the corresponding thermal conductivities (W/mK), g (W/m^{3}K) is the electron-phonon coupling coefficient, and $S(z,t)$ is the heat source term due to laser absorption. Laser absorption was modeled using the Beer-Lambert law:

$$S(z,t) = \alpha A I(t) e^{-\alpha z}. \tag{3.7}$$

In this expression, A is the absorptance, *I(t)* is the laser intensity as a function of time (Wm^{-2}), α is the absorption coefficient (m^{-1}), and z is skin depth thickness (m^{-1}). In the following simulations, a pulse of constant intensity during the pulse width will be considered. The material parameters in Equations 3.5 and 3.6, heat capacities and thermal conductivities, depend on both the electron and lattice temperatures.

Finite Element Method simulations were performed in COMSOL using axisymmetric geometry and a Gaussian beam (200 µm waist). Boundary insulation was applied due to the substrate size. Pulse energy was increased until the surface temperature reached the melting point (1064°C), defining the damage threshold. All thermal parameters were treated as temperature-dependent.

Table 3.2: Model parameters for gold and silver coatings on a fused silica substrate [29, 141, 142].

Material	Gold	Silver	Fused silica
Refractive index	0.08-4.6i	0.27-8.7i	-
Specific heat capacity (J/(Kg K))	130	235	830
Density (kg/m^{-3})	19400	10500	2200
Thermal conductivity (W/(m K)	-	-	1.2
Lattice thermal conductivity (W/(m K))	320	430	-
Lattice volumetric heat capacity (J/m^3 K)	2.5×10^6	2.5×10^6	-
Thermal diffusivity (m^2/s)	1.28×10^{-4}	1.72×10^{-4}	6.57×10^{-7}
Melting point (°C)	1064	962	-
Electron heat capacity (J/m^3 K)	$67.6 \times T_e \leq 2000$ K	$63.3 \times T_e \leq 4000$ K	-
Electron-phonon coupling coefficient	2.5×10^{16} for $T_e \leq 3000$ K	1.5×10^{16} for $T_e \leq 5000$ K	-
Electron thermal conductivity	$K_e = \frac{\nu_F^2 C_e(T_e)}{3BT_l + AT_e^2}$ $A = 1.2 \times 10^7$ K^{-2}s^{-1}, $B = 1.23 \times 10^{11}$ K^{-2}s^{-1}	$K_e = K_l \frac{T_e}{T_l}$	-

Results

Experimental LIDT data and empirical scaling laws

This section presents experimental LIDT results in the range of 10 fs to 10 s at IR wavelengths (1030 nm, 1064 nm, 1070 nm) and discusses the empirical laws used to describe the tendencies. Figure 3.1 summarizes the LIDT data at all pulse durations and materials investigated for single-shot and multi-shot (for CW regime, LIDT was defined only for the 1-on-1) testing protocols.

To evaluate the dependence of LIDT on pulse duration, an empirical power-law approximation is applied (LIDT $\sim \tau^x$). This scaling law was applicable in both pulsed and CW regimes:

- **Pulsed regime (10 fs $< \tau <$ 8 ns):** the dependence of LIDT on the duration of the pulse is weak, with empirical exponents ranging from 0.01 to 0.15 for damage thresholds of 1-on-1 and from 0.05 to 0.23 for S(1000)-on-1 thresholds. The stronger dependence observed under multipulse conditions suggests that repeated exposure weakens the material, potentially altering its reflectivity due to surface modifications [143, 144].

- **CW regime (1 ms $< \tau <$ 10 s):** in this regime, the dependence of LIDT on the duration of the pulse is nearly linear, with power-law exponents ranging from 0.77 to 1.

The reduction in LIDT under multipulse exposure is attributed to the effects of material fatigue [144, 145]. For metallic films, absorbed laser irradiation induces thermal expansion, which leads to strain in the near-surface region. If laser-induced stress exceeds the film strength, irreversible deformation occurs, increasing surface roughness and absorption [146]. Repeated thermal cycling

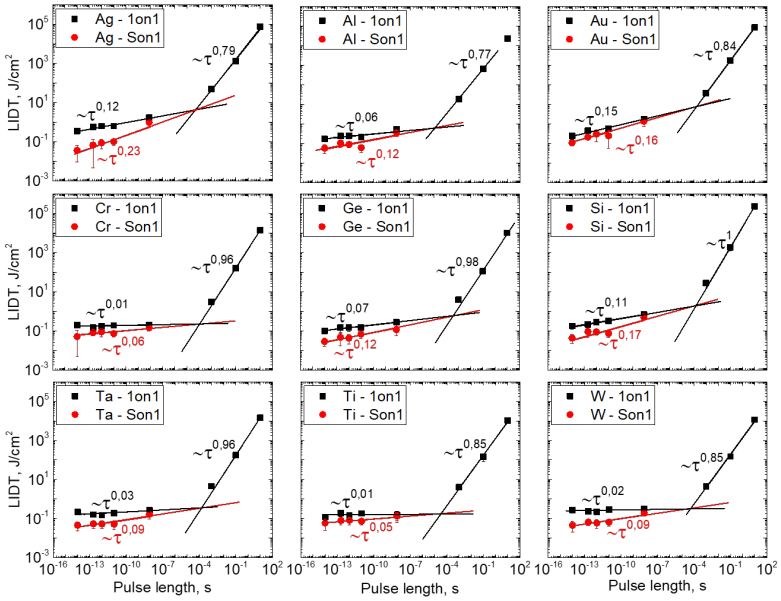

Figure 3.1: Experimental data on 7 metallic and 2 semiconductor coatings with 1-on-1 and S(1000)-on-1 protocols. Solid lines represent empirical power-law fits. The cross-point between pulsed and CW regimes indicates the thermal decay constant.

can also cause micro-structural changes, contributing to optical failure [73], as well as surface oxidation at high temperatures, which can further modify absorption.

A critical feature in Figure 3.1 is the transition point between the pulsed and CW regimes, corresponding to the thermal decay constant (TDC). This represents the characteristic time for the material to cool between pulses [29]. If the period between repetitive pulses is shorter than the TDC, heat accumulates over time, which may lead to delayed melting or thermal fatigue in the S(1000)-on-1 regime. For pulse durations longer than the TDC time, heat dissipates efficiently during the pulse, reducing the sensitivity of LIDT to the pulse duration. Interestingly, both the 1-on-1 and the S(1000)-on-1 approximations converge at the same TDC, indicating that while fatigue influences the LIDT scaling, the TDC remains a fundamental material property.

To quantify the relationship between TDC and material parameters, we performed a polynomial regression analysis (see Fig. 3.2). The best-fit empirical model is:

$$\begin{aligned} \tau_{\mathrm{TDC}} &= 0.2353 - 3.269 \times 10^{-4} C + \\ &(C - 392.67)(h - 300.06)(-4.85 \times 10^{-7}) + 2.424 \times 10^{-4} h \end{aligned} \tag{3.8}$$

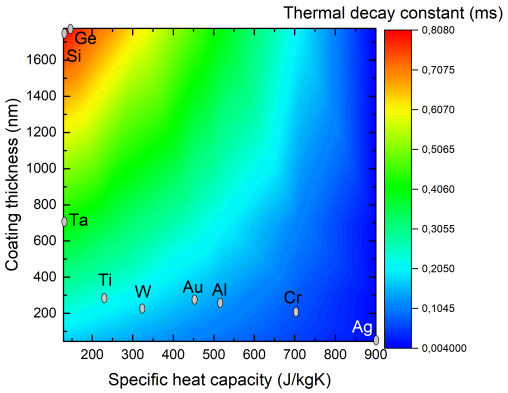

Figure 3.2: 3D map showing the relationship between the thermal decay constant, coating thickness, and specific heat capacity.

where τ_{TDC} (ms) is the thermal decay constant, C (J/(kgK)) is the specific heat capacity and h (nm) is the thickness of the material. This model suggests a complex dependence of τ_{TDC} on the heat capacity and thickness, with an interaction term $(C - 392.67)(h - 300.06)$ indicating a coupled effect between these properties.

Role of absorptance in LIDT

According to the heat flow model [29], LIDT should inversely correlate with the absorptance of the material. In Fig. 3.3, the experimental LIDT for all coatings is shown as a function of inverse absorptance $(1/(1-R))$ for two representative pulse durations, assuming negligible scattering (and transmission for Ag due to the comparable thickness to the skin depth of the coating) losses, and corresponding to the pulsed and CW regimes.

In the CW regime (100 ms, right Y-axis), a clear trend is observed: lower absorptance correlates with higher damage thresholds, which is consistent with theory and recent findings on hybrid metal-dielectric coatings under CW irradiation [147]. As expected, in the CW regime, the accumulation of heat in both the coating and substrate eventually leads to melting, following the predicted trend.

However, in the pulsed regime (10 ps, left Y axis), deviations arise primarily due to thermal capacity of the coating. For example, tungsten (W), with a high melting point (∼3422°C), requires more energy to melt, leading to higher LIDT values. In contrast, silicon (Si) exhibits the highest resistance to laser damage when deposited on a transparent target. This is due to its partial transparency in the near-infrared range [148], which reduces energy absorption and thus increases LIDT.

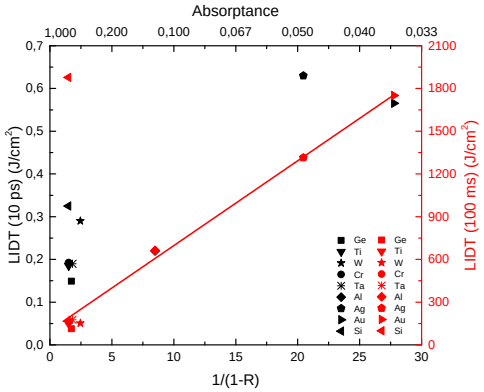

Figure 3.3: LIDT as a function of inverse absorptance for 10 ps and 100 ms pulse durations for all coatings.

Numerical LIDT simulations of gold and silver coatings

Figure 3.4A) illustrates direct comparison of the single shot experimental LIDT results for gold and silver coatings with first-order heat flow approximations (Equations 3.2 and 3.4, dashed curve) and numerical simulations using the TTM (solid curves). In the pulsed regime, there is insufficient time for radial or longitudinal diffusion during the pulse. For long pulses, heat loss to the substrate becomes significant, making the thermal properties of the substrate the dominant factor, as shown in Figure 3.5. Thus, we used the material parameters of gold and silver for short pulses and the heat diffusion parameters of glass for CW.

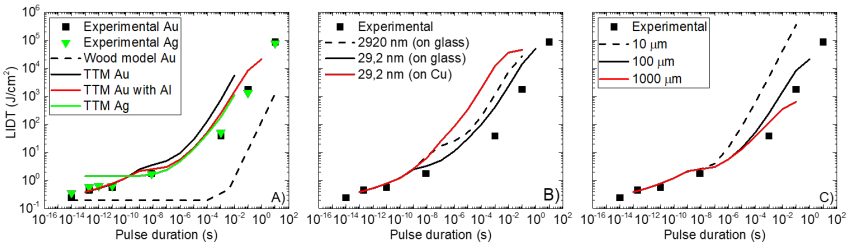

Figure 3.4: A) LIDT simulations for gold and silver coatings using the model presented by Wood [29] and TTM, indicating the influence of the adhesive layer within the coating stack. B) Effect of the gold layer on glass and copper substrates using TTM, C) effect of different beam diameters using TTM.

The first-order approximation predicts a transition from pulse width independence to a linear dependence on the pulse width. However, it lacks accuracy and fails to estimate LIDT correctly in absolute terms, as it neglects transient

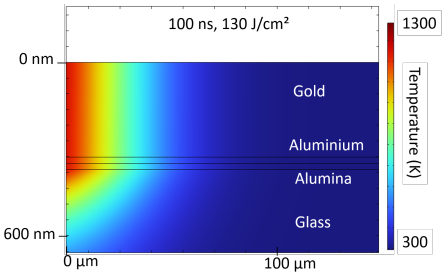

Figure 3.5: Electron temperature distribution at the end of the laser pulse (100 ns).

effects such as electron dynamics in the femtosecond regime, layer structure, and cylindrical geometry.

In contrast, the TTM closely matches the experimental data in the pulsed regime, with LIDT scaling as $\tau^{0.18}$ for short pulses (<10 ns). For long pulses (>100 ns), the LIDT scales as $\tau^{0.82}$, but the simulated values (black curve) were slightly higher than the experimental data. This discrepancy occurred because the melting point of the aluminum underlayer (660°C) was not initially considered. After accounting for the aluminum underlayer melting point (red curve), the experimental data were better reproduced with TMM.

To assess the applicability of TTM, we also simulated a use-case scenario of silver coating. In this case, the thickness of the Ag layer is comparable to the optical penetration depth, which limits the thermal diffusion along the depth of the layer. Consequently, a constant LIDT is expected across pulse durations. However, the TTM does not account for energy transport within the underlying Al buffer layer, introducing a limitation in the model. In reality, electronic heat diffusion within the Al layer may enhance energy dissipation, suggesting that the actual LIDT could be lower than predicted by the model.

To assess the sensitivity of the scaling law to coating thickness and substrate thermal conductivity, LIDT was calculated for gold layers of 29.2 nm and 2920 nm – one-tenth and ten times the nominal thickness (292 nm). Additionally, a high-conductivity copper (Cu) substrate was modeled in place of glass. As shown in Figure 3.4B), for long pulses where thermal diffusion is significant, LIDT increases with both coating thickness and substrate conductivity, consistent with previous studies [110, 111]. For short pulses, where the thermal diffusion length is smaller than the film thickness, heat remains confined within the coating, rendering substrate effects negligible. Notably, substrate influence becomes relevant at pulse durations around 1 ns and longer.

The impact of beam diameter on thermal diffusion was also simulated. As shown in Figure 3.4C), smaller beam sizes (10 µm and 100 µm vs. 1 mm) lead to increased radial heat loss in the CW regime, resulting in higher LIDT values, in agreement with observations by Wood [29].

Discussion

The scaling of LIDT with pulse duration in metallic and semiconductor coatings was evaluated across a broad temporal range from 10 fs to 10 s. The experimental results demonstrated a power-law dependence of LIDT on pulse duration (LIDT $\sim \tau^x$), with distinct behaviors observed in the pulsed and CW regimes. In the pulsed regime (10 fs – 9 ns), the LIDT exhibited only weak dependence on pulse duration, with scaling exponents ranging from 0.01 – 0.15 for 1-on-1 and 0.05 – 0.23 for S-on-1 conditions. In contrast, the CW regime (1 ms – 10 s) showed a near-linear scaling, with exponents between 0.77 and 1.00.

The transition between pulsed and CW regimes was governed by the thermal decay constant, which in turn depends on coating thickness and material-specific properties such as specific heat capacity. These findings align well with theoretical predictions by Wood [29], which postulate that in both transparent and absorbing materials, LIDT is largely independent of pulse duration in the ultrashort regime and scales linearly in the CW regime. However, Wood's model assumes a semi-infinite solid, and thus does not fully capture the behavior of thin metallic coatings on dielectric substrates. To address this limitation, the TTM was employed, yielding improved agreement with the experimental data, especially in the ultrafast and transition regimes.

Experimental data further revealed an inverse correlation between LIDT and absorptance, consistent with previous work on hybrid metal-dielectric systems [147]. Still, certain deviations in the pulsed regime – particularly for tungsten and tantalum – indicated that specific heat capacity and melting temperature also play important roles. Fatigue effects under multi-pulse irradiation were found to enhance the LIDT dependence on pulse duration, likely due to cumulative mechanical or structural degradation.

In addition to intrinsic material properties, substrate characteristics and laser beam diameter were identified as influential parameters. TTM simulations demonstrated that coatings deposited on substrates with high thermal diffusivity achieve higher LIDTs, due to improved heat dissipation. Furthermore, modeling results confirmed that the thermal decay constant is not only a function of material composition but is also affected by coating thickness and lateral heat transport.

While the TTM accurately captured LIDT trends, additional refinement is necessary for CW regimes, particularly to model substrate and interface effects more precisely. Overall, the observed weak scaling in the pulsed regime supports the conclusion that LIDT in metals is limited by ultrafast energy transfer dynamics, whereas CW behavior is governed by slower heat diffusion and bulk thermal response. These findings offer a comprehensive framework for predicting damage resistance in metallic and semiconductor coatings over broad temporal scales.

Conclusions

The results reveal a weak power-law dependence of LIDT on pulse duration in the pulsed regime ($\tau^{0.01–0.23}$), with a nearly linear scaling ($\tau^{0.77–1.00}$) observed in the CW regime. The transition between regimes is governed by the thermal decay constant, which depends on the coating's specific heat capacity and thickness. Both experimental data and numerical modeling confirmed that substrate thermal diffusivity and beam diameter also influence LIDT behavior.

Additionally, LIDT was found to be inversely correlated with material absorptance, though deviations in the pulsed regime point to further contributions from thermal capacity and melting temperature. Fatigue effects were evident under multipulse exposure, enhancing the pulse duration dependence in the pulsed regime.

The Two-Temperature Model provided more accurate predictions than classical heat flow models, particularly in the sub-nanosecond range, and demonstrated the need for refined modeling in CW conditions. However, the study was limited to fixed wavelengths and beam sizes, which may constrain its applicability across broader spectral or geometric domains.

3.2 LIDT scaling on pulse duration in dielectric coatings

Motivation

AR coatings are widely used in imaging and laser systems to minimize photon losses and maximize optical transmission. However, the maximum output power in high-power laser systems is ultimately limited by the LIDT of the optical components. AR-coated nonlinear crystals are frequently the limiting elements in such systems, yet available LIDT data for these coatings remain scarce. Previous studies have largely focused on short-term exposure, typically limited to single-pulse or a few-hundred-pulse conditions per test site. In practical applications, however, optical components are subjected to prolonged irradiation, where cumulative effects such as laser-induced fatigue become significant. Fatigue can reduce the optical lifetime well below the single-shot damage threshold, even when no immediate degradation is observed.

For example, Möller [82] reported performance deterioration in LBO crystals after 192 hours of third-harmonic generation (THG) at 1.6 W. Similarly, Hong et al. [127] observed the onset of damage in a THG setup after 130 hours of exposure ($P_{\mathrm{IR}} = 97$ W, $P_{\mathrm{UV}} = 20.2$ W), with 15% power loss occurring after 371 hours.

Evidence for separate failure modes also arises from damage morphology. Studies have shown that multi-pulse irradiation can result in either catastrophic

damage (craters) or non-catastrophic modifications such as laser-induced color changes, observable via DIC Nomarski microscopy [14, 16, 149]. Color change tends to appear at lower fluences or earlier in exposure time compared to catastrophic damage. Although the precise nature of this failure mode remains unclear, it has been attributed to the generation of color centers via multiphoton ionization, which alters refractive index and absorption properties [14, 16, 149].

To date, no systematic study has examined LIDT behavior in AR-coated nonlinear crystals while accounting for both fatigue effects and failure mode analysis over the fs – ns pulse duration range. This gap is particularly pronounced in the ultraviolet spectral region, where LIDT scaling remains largely unexplored.

The objective of this work is to address these gaps by conducting a case study on LIDT scaling of two types of AR coatings on LBO crystals. The investigation spans IR (1030 nm, 1064 nm) and UV (343 nm, 355 nm) wavelengths and covers pulse durations from 50 fs to 9 ns at the repetition rate of 1 kHz and beam diameter $\sim$30 μm at $1/e^2$ level. Both 1-on-1 and S(10^5)-on-1 testing protocols are employed, along with detailed failure mode characterization.

Materials and methods

Four LBO crystals (12 × 12 × 10 mm, $\theta = 42.2°$, $\varphi = 90°$, AOI = 0°) were prepared to ensure sufficient area for statistical LIDT analysis. All crystals were polished in the same batch and coated simultaneously via ion beam sputtering (IBS). The entrance surface (S_1) was AR-coated for 1064 nm + 532 nm wavelengths using zirconia, and the exit surface (S_2) was deposited with AR 355 nm using sapphire as a high-index material. Silica was used as a low-index material in both cases:

- S_1: AR $< 0.2\%$, 1064 nm + 532 nm (n_L – SiO_2, n_H – ZrO_2);
- S_2: AR $< 0.2\%$, 355 nm (n_L – SiO_2, n_H – Al_2O_3).

LIDT was measured using S-on-1 tests: 1, 10, 100, 1000, 10000, and 10^5 pulses per test site, spaced by three beam diameters ($\sim$100 μm) at AOI = 0. In 50 fs – 10 ps range, damage was deterministic, and LIDT was defined as the average between the highest non-damaging and lowest damaging fluences. For 150 ps and longer pulses, damage became probabilistic; LIDT was then extracted from fitted damage probability curves at 0% probability. Pre- and post-exposure inspection via Nomarski microscopy allowed classification into no damage, color change, or catastrophic damage.

Methodology of analysis

To interpret experimentally obtained LIDT results, the electron generation model was considered – SRE suggested by Stuart et al. [6]. In Fig. 3.6, the

role of each factor in SRE on LIDT scaling law is illustrated using a simplified fictitious dielectric material. To generate this graph, a multi-photon process (6 photons) is assumed, along with avalanche ionization (AI) and carrier recombination (RE). A critical free-electron density ($\sim 10^{21}$ cm^{-3}), corresponding to the plasma frequency, is used as the damage criterion.

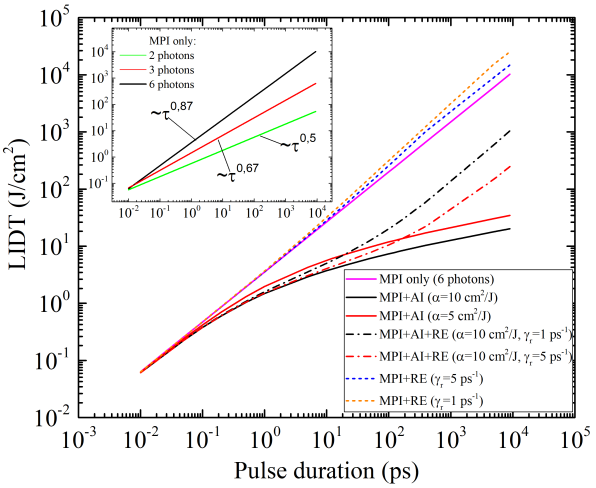

Figure 3.6: Effect of individual parameters of SRE model on LIDT scaling law.

The inset in Fig. 3.6 shows how bandgap (or wavelength) affects LIDT scaling when only MPI is considered. For a 6-photon process, scaling follows $\sim \tau^{0.87}$, while a 2-photon process gives $\sim \tau^{0.5}$. Including AI reduces LIDT sensitivity to pulse duration, especially in the long-pulse regime. RE also affects scaling, causing LIDT to increase at pulse durations exceeding the recombination time. When only MPI and RE are included, recombination steepens the scaling slightly. These results show that LIDT scaling is not universal but depends on material and irradiation conditions. An exponent of 0.5 or more indicates MPI and RE dominance, while a lower exponent signals AI influence. The model also shows that the dominant mechanism can shift with pulse duration or wavelength.

While the SRE model captures the main trends of electronic excitation, it ignores carrier energy in the conduction band, limiting its completeness. Kaiser [35] and Rethfeld [34] introduced the MRE model, which accounts for both electron density and kinetic energy in the conduction band. To simplify the complexity of the MRE, Déziel et al. [100] recently proposed a delayed-rate equation (DRE) approach. DRE tracks the mean kinetic energy of electrons and holes with a single equation, unlike MRE, which requires multiple equations

for each electron level.

$$\frac{d\rho}{dt} = w_{\mathrm{MPI}}\rho_{\mathrm{n}} + \sum_{s=e,h} \gamma_{\mathrm{n}}^{\mathrm{s}}\zeta^{\mathrm{s}}\rho - \gamma_{\mathrm{R}}\rho. \tag{3.9}$$

Here, electron generation is weighted by the density of neutral atoms $\rho_{\mathrm{n}} = \rho_{\mathrm{mol}} - \rho$, where ρ_{mol} is the molecular density of the material. The fraction of carriers (holes and electrons) that have an energy higher than the critical is calculated by

$$\zeta^{\mathrm{s}} = \mathrm{erfc}(r_{\mathrm{s}}) + \frac{2r_{\mathrm{s}}}{\sqrt{\pi}}\exp(-r_{\mathrm{s}}^2), \tag{3.10}$$

where $s = (e, h)$ and

$$r_{\mathrm{s}} = \sqrt{\frac{3E_{\mathrm{c}}}{2E_{\mathrm{k}}^{\mathrm{s}}}}. \tag{3.11}$$

Here E_{c} is the critical energy of the electron that is required to trigger an impact ionization event, and $E_{\mathrm{k}}^{\mathrm{s}}$ is the gained mean kinetic energy of the carriers. Further in the study, the DRE model is used while interpreting experimental results.

Results and discussion

Damage morphology

Two types of damage could be distinguished, namely, catastrophic damage – features ablation craters (causing scattering of light: not shown here) and non-catastrophic damage – a laser-induced modification, barely apparent as color change. It typically reproduces the shape of the beam and does not cause any light scattering in damage detection. Sorting of damage morphology into different categories allowed interpreting damage statistics for each failure mode separately as well as analyzing pertinent scaling laws individually.

In Fig. 3.7, damage morphologies initiated by IR wavelength at 1-on-1 and 10^5-on-1 pulses are outlined. In the case of short pulses (<10 ps), color change was observed at fluence levels below catastrophic damage for both single- and multi-shot irradiation. For single-shot color changes, some filamentation was observed in the bulk of the nonlinear crystal, which could have screened the color change damage. However, for multi-pulse exposure, no filamentation at the color change LIDTs was observed. Catastrophic damage was initiated in all cases for higher fluence. However, color changes are not apparent for pulse duration >10 ps, thus indicating the transition of the dominating damage mechanism.

In the case of UV irradiation, similar trends are observed (illustrated in Fig. 3.8). In all cases, laser-induced color changes are better observed for

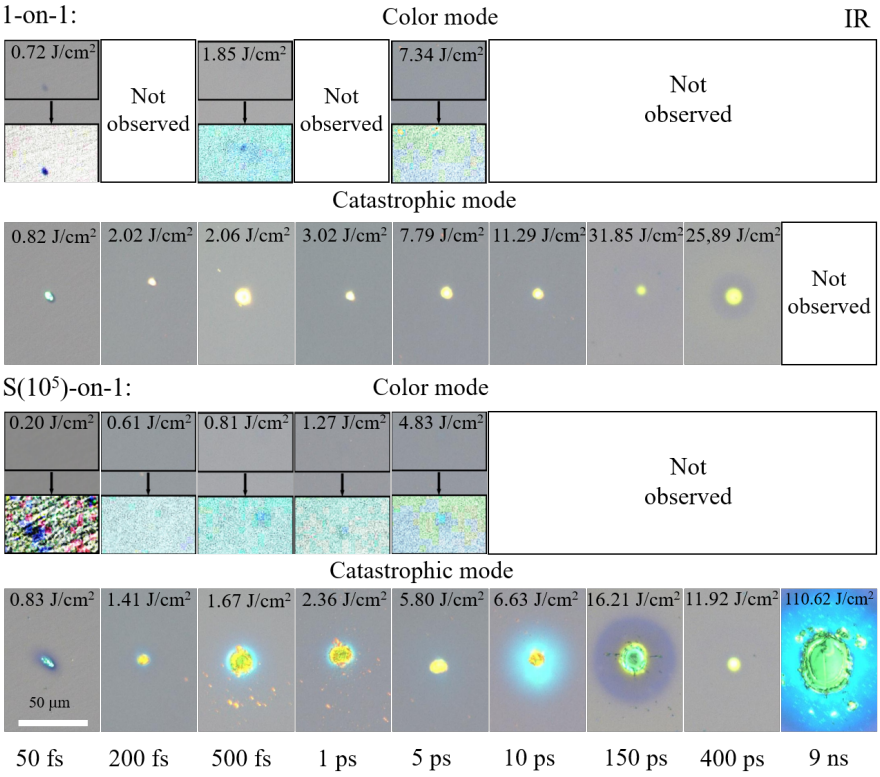

Figure 3.7: Damage morphology obtained at threshold fluence values (see Fig. 3.10 (a) and (b)) on S_1 coating at IR wavelengths for all the investigated pulse durations.

multi-shot irradiation with shorter pulse duration, while single-shot irradiation produces either negligible modifications or abrupt catastrophic damage.

Damage caused by extrinsic defects in the AR coatings and in the Beilby layer of the polished LBO crystal surfaces generally cannot be overlooked; however, in this case, a rather small beam diameter is used, and no pinpoint morphology is observed for color change type damage. Therefore, it is safe to assume that color change is not caused by Beilby layer defects. However, this is most likely the case for catastrophic damage.

LIDT results

Figure 3.9 illustrates normalized (to 1-on-1 value) LIDTs as a function of the incident number of laser pulses per test site. Each curve was obtained for an individual failure mode (either catastrophic damage or color change). Figures 3.9(a), (b) show that both coatings begin to degrade after only 10 – 100 pulses, with a continuous decrease in LIDT observed at both wavelengths (color

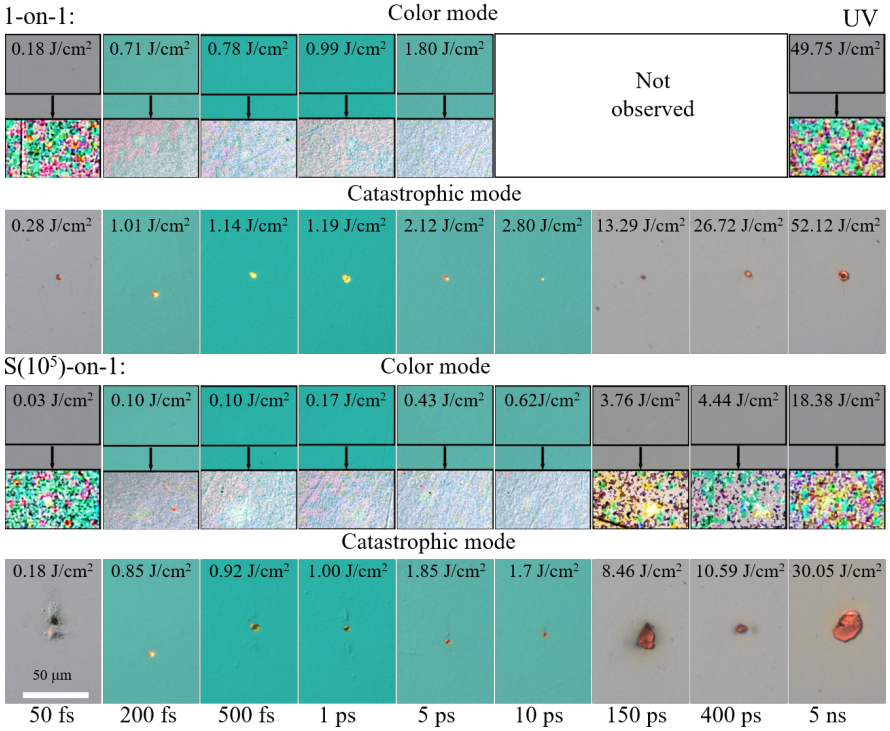

Figure 3.8: Damage morphology obtained at threshold fluence values (see Fig. 3.10 (c) and (d)) on S_2 at UV wavelengths for all the investigated pulse durations.

change at 5 ps was only observed after 10^5 pulses, therefore it is normalized to single-shot catastrophic LIDT). Notably, color mode fatigue is wavelength-dependent: at IR, the LIDT decreases by 35 – 70% from its initial value, while at UV, the decrease reaches 65 – 90%. However, when normalized, the fatigue trend exhibits weak or no dependence on pulse duration for a fixed wavelength.

In contrast, catastrophic damage (Figs. 3.9(c), (d)) displays a pulse-duration-dependent fatigue response at both IR and UV wavelengths: the longer the pulse, the more pronounced the LIDT decrease. At IR, the LIDT decreases only slightly at 50 fs, but drops by up to 55% at 400 ps. At UV, the LIDT decreases by 12 – 60%, depending on the pulse duration. In most cases, catastrophic damage fatigue saturates after approximately 1000 pulses, indicating a fatigue limit; however, in some instances, further LIDT decrease continues. These distinct behaviors suggest fundamentally different initiation mechanisms for color change and catastrophic damage, as previously discussed by Smalakys et al. [16].

The strongest fatigue is associated with color mode and the shortest pulse durations, indicating a strong correlation with the MPI regime and electronic

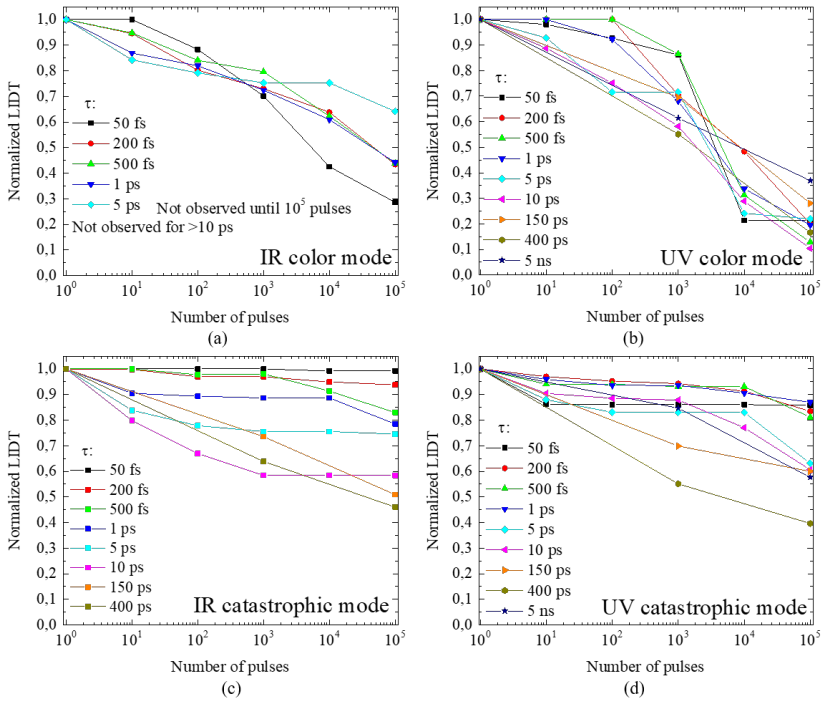

Figure 3.9: Fatigue effect of color mode and catastrophic damage: (a) color mode at IR (on S_1; at 5 ps color mode was observed only after 10^5 pulses – LIDT at lower number of pulses are from catastrophic data for guidance), (b) color mode at UV (on S_2), (c) catastrophic damage at IR and (d) catastrophic damage at UV.

excitation-induced modifications. Given the multi-shot nature of the effect, it is likely driven by the accumulation of atomic-scale lattice defects rather than macroscopic ones. In contrast, catastrophic damage is typically linked to macroscopic defects and shows weaker fatigue at long pulse durations in the IR range [16]. Since thermal decay times are much shorter than the pulse repetition period, thermal accumulation is not expected to play a significant role in the observed fatigue [150].

Empirical scaling laws

In this section, the analysis of 1-on-1 and S(10^5)-on-1 LIDT results is presented in absolute scale as a function of pulse duration. When experimental LIDT data are plotted on a log-log scale, each failure mode appears to be represented by a linear trend (see Fig. 3.10), allowing the data to be approximated by a power-law relation of the form $LIDT = a\tau^b$. It becomes apparent that the scaling

behavior of the two failure modes is distinct, thus necessitating their separate analysis.

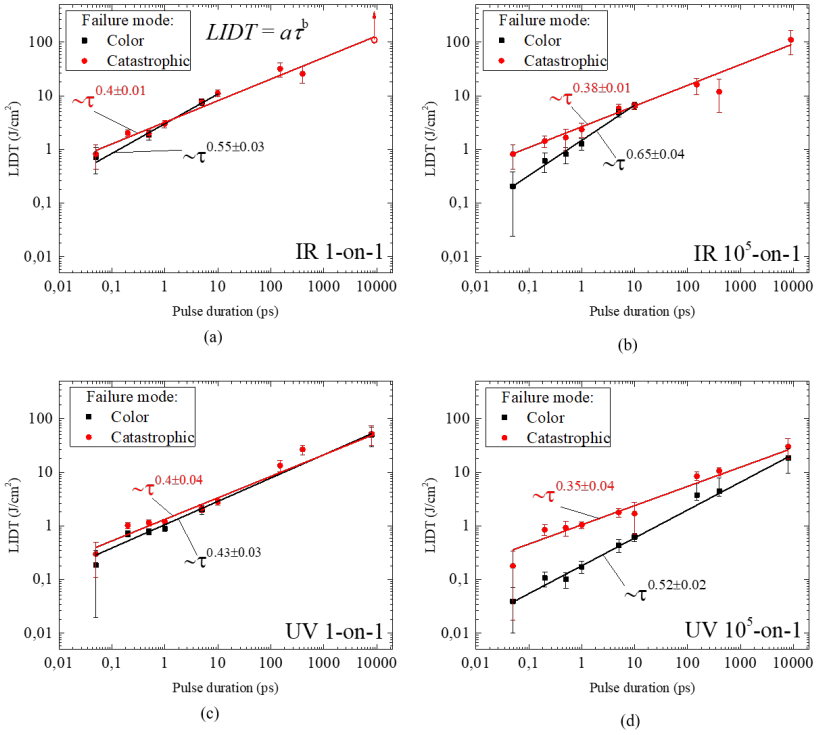

Figure 3.10: LIDT scaling laws for damage modes: (a) – 1-on-1, (b) – 10^5-on-1 pulses at IR wavelength on S_1, (c) – 1-on-1 and (d) – 10^5-on-1 pulses at UV wavelength on S_2. Data were approximated with a power-law curve, and the respective scaling is shown in the graphs.

For single-pulse exposure, color change and catastrophic LIDTs at both IR and UV wavelengths showed negligible differences, with color mode scaling as $\tau^{0.55}$ and catastrophic damage as $\tau^{0.4}$ in the IR (Figs. 3.10(a), (b)). Catastrophic damage was absent (red arrow in Fig. 3.10(a)) at the longest IR pulse (9 ns) even at ~110 J/cm^2, suggesting a higher intrinsic threshold or low defect density. With 10^5 pulses, greater divergence appeared: IR color mode scaled as $\tau^{0.65}$, while catastrophic damage remained near $\tau^{0.38}$. This divergence was more pronounced at femtosecond durations and aligned with previous studies [71, 120, 121].

For UV (Figs. 3.10(c), (d)), single-pulse color and catastrophic damage scaled as $\tau^{0.43}$ and $\tau^{0.4}$, respectively. Multi-shot UV exposure revealed clear separation across 50 fs – 9 ns: color mode scaling was $\tau^{0.52}$, catastrophic damage $\tau^{0.35}$.

The UV color mode followed a $\sim \tau^{0.5}$ scaling, while catastrophic damage showed $\tau^{0.35-0.4}$ for both wavelengths. Catastrophic damage was less sensitive to pulse count, whereas color mode scaling increased with pulses, indicating a cumulative process likely driven by nonlinear absorption and color center formation. Color mode scaling also depended more strongly on wavelength: $\tau^{0.55-0.65}$ (IR) vs. $\tau^{0.43-0.52}$ (UV). These suggest two competing or linked damage mechanisms per failure mode, discussed further later.

Comparison with other studies [6, 94, 99, 120] on dielectric coatings and glasses showed no clear ps – fs scaling transition at IR wavelengths. Defect-driven catastrophic damage depends on material properties and defect density for longer pulses, making the sampled area and test method statistically significant. Color changes, often subtle, may have been missed as damage precursors. Notably, IR color changes emerged near the 20-ps transition point, where shorter pulses produce color changes, and longer pulses cause catastrophic damage.

Damage mechanisms

To interpret LIDT data and damage physics, the DRE approach is used. Since each AR coating has high (H) and low (L) index layers, analysis focuses on the H material, which limits LIDT due to its lower band gap [94]. Two failure modes per coating are described with a single set of material parameters (Table 3.3), assuming different damage criteria for each mode.

Two critical criteria are considered: critical electron density at plasma frequency, $\rho \approx 10^{21}$ cm^{-3}, and sub-critical density, $\rho \approx 10^{18}$ cm^{-3}, initiating color changes. Both UV and IR coatings were examined.

Theoretical LIDT curves are obtained by varying fluence for each pulse duration until damage criteria are met: first sub-critical density (color changes), then critical density (catastrophic damage). Predictions are compared with experimental data (Fig. 3.11), plotted alongside 10^5-on-1 catastrophic and color change cases.

Table 3.3: Dielectric material parameters associated with theoretical simulations. Plasma damping γ (fs^{-1}), energy bandgap E_g (eV), recombination rate γ_r (ps^{-1}), effective mass of an electron (m_e) and hole (m_h) are set by fitting the data. σ (10^{-25}/m^2), ρ_{mol} (10^{22} cm^{-3}) and n are gathered from [100].

	γ	γ_r	m_e	m_h	E_g	σ	ρ_{mol}	n
$\mathbf{ZrO_2}$	1.0	2.0	0.4	0.7	4.0	6.175	1.0	2.2
$\mathbf{Al_2O_3}$	1.0	0.3	0.2	0.2	6.0	13.3	1.0	1.76

Catastrophic damage requires all processes (MPI + AI + RE) for an accurate description, though MPI-only curves are shown for clarity. MPI dominates LIDT at short pulses (<50 fs), consistent with prior studies [93, 100, 151]. For

longer pulses, avalanche ionization and recombination cause deviations from MPI-only curves and a characteristic transition (IR and UV) as predicted by the Keldysh model [27, 100, 151] (Fig. 3.11 (a)).

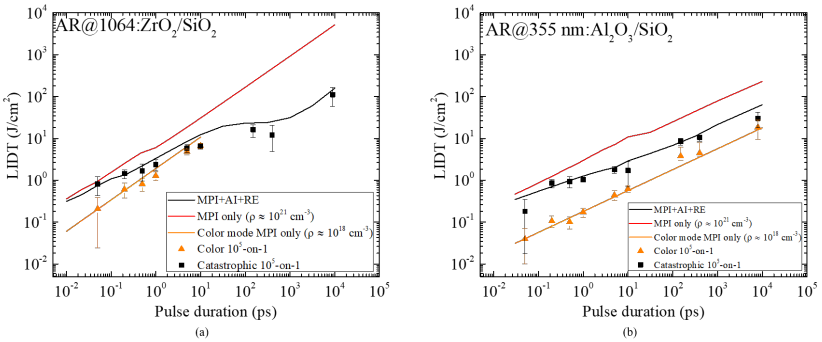

Figure 3.11: Experimental data approximated by DRE model [100]: (a) – AR coating for IR wavelength, (b) – AR coating for UV wavelength. In both cases, different critical electron density was used: for 1-on-1 catastrophic and color damage – 10^{21} cm^{-3} and for 10^5-on-1 color mode - 3×10^{18} cm^{-3}.

Color mode data cannot be described by the critical plasma density criterion. The MPI-only model with reduced electron density ($\rho \approx 10^{18}$ cm^{-3}, Fig. 3.11 (a), orange curve) reproduces color change data using the same parameters. This suggests color changes arise from MPI-driven excitation without AI, which requires higher fluence and plasma density. Each pulse induces nonlinear excitation, causing gradual cumulative modifications, detectable by DIC microscopy. Preliminary evidence indicates this may eventually lead to catastrophic damage, though further study is needed. In IR, color changes are screened by catastrophic damage for pulses >10 ps.

In UV (Fig. 3.11 (b)), S(10^5)-on-1 damage trends align with IR catastrophic damage, driven by MPI and AI across pulse durations. Recombination effects are negligible in the nanosecond range. Color mode requires lowering the threshold to $\rho = 3 \times 10^{18}$ cm^{-3}. Unlike IR, color mode appears for all measured durations after 10^5 pulses with no mode screening, attributed to two-photon ionization. The damage mode gap in UV is larger than in IR.

Discussion

The LIDT scaling behavior in dielectric coatings was investigated using AR-coated LBO crystals under IR and UV irradiation. The study focused on two distinct failure modes: catastrophic damage and sub-catastrophic color change. For the first time, laser-induced color changes were evaluated in terms of their LIDT scaling with pulse duration.

The experimental results demonstrated that LIDT scaling in dielectric coatings is strongly dependent on failure mode, wavelength, and number of pulses. Color change damage exhibited a clear square-root-like dependence on pulse duration, with scaling exponents ranging from $\tau^{0.55-0.65}$ at IR and $\tau^{0.43-0.52}$ at UV wavelengths. These values are consistent with 2PA as the dominant mechanism, supported by simulations based on the SRE model [6]. The SRE model predicts an exponent of 0.5 for 2PA, while higher exponents indicate the possible involvement of higher-order multiphoton absorption processes. In contrast, catastrophic damage exhibited weaker scaling, with exponents in the range of $\tau^{0.35-0.4}$ across the full investigated range (50 fs – 9 ns). These lower exponents suggest the involvement of avalanche ionization, which becomes significant at higher electron densities and leads to plasma formation. The distinction between failure modes is further supported by electron density criteria: catastrophic damage corresponds to reaching a critical plasma density ($\sim \rho^{21}$ cm^{-3}), while color change damage is associated with a sub-critical density ($\sim \rho^{18}$ cm^{-3}).

Numerical simulations using both the SRE and DRE models showed that the same material parameters can reproduce both damage modes, provided that distinct electron density thresholds are applied. These findings emphasize that the scaling of LIDT is not a universal property of the material but rather depends on the physical mechanism leading to damage and the specific damage threshold employed. Fatigue effects were also found to vary between damage modes. Catastrophic fatigue displayed increasing sensitivity to pulse duration under multi-pulse exposure, particularly at longer pulse durations and for both IR and UV wavelengths. In contrast, color change fatigue was largely insensitive to pulse duration under prolonged exposure, indicating different accumulative damage mechanisms.

In general, the LIDT behavior in dielectric coatings was shown to depend not only on pulse duration but also on other parameters, including wavelength, bandgap, and pulse count. Multiphoton ionization dominates the initial stages of damage for both failure modes, particularly in the fs – ps regime, but plays a different role depending on whether the process terminates in color change or catastrophic breakdown. In particular, multiphoton absorption acts as a precursor for avalanche ionization in catastrophic damage [6, 15, 35], while it independently drives color change at sub-critical densities. The observed behavior also aligns with previous studies on nonlinear crystals and AR-coated optics, which report similar trends in catastrophic LIDT scaling and wavelength dependence [71, 82, 120]. However, the present results extend this understanding by clearly separating the scaling behavior of distinct failure modes and providing experimental validation over a broad pulse duration range.

Ultimately, LIDT scaling in dielectric coatings emerges as a multi-factorial process, where wavelength, bandgap, fatigue effects, and the dominant ion-

ization mechanisms interact to define the observed behavior. While classical scaling laws such as $\tau^{0.5}$ remain useful, these findings suggest that damage prediction requires nuanced consideration of damage mode, irradiation conditions, and material-specific parameters.

Conclusions

For the first time, laser-induced color changes of AR coatings on LBO crystals under IR and UV irradiation were analyzed in the context of LIDT scaling with pulse duration. A direct comparison between experimental LIDT data and rate equation models (SRE and DRE) reveals that LIDT scaling is not universal, but failure mode dependent. Multiphoton absorption dominates damage initiation at short pulse durations and also drives color change formation at longer durations, particularly under prolonged multipulse exposure. Accordingly, MPA-driven color changes exhibit a clear dependence on the material bandgap and laser wavelength. Experimentally, LIDT scaling exponents for color changes induced by 1 to 10^5 pulses were found to be $\tau^{0.55-0.65}$ at IR wavelengths and $\tau^{0.43-0.52}$ at UV wavelengths.

SRE simulations associate an exponent of $\tau^{0.5}$ with two-photon absorption, while larger exponents imply involvement of higher-order photon processes. Both failure modes were reproduced using the same material parameters, but with different damage thresholds – sub-critical and critical free electron densities – for color change and catastrophic damage, respectively.

LIDT scaling for catastrophic damage was consistent across both IR and UV wavelengths, with $\tau^{0.35-0.4}$ observed over the 50 fs to 9 ns range under both 1-on-1 and 10^5-on-1 conditions. The exponent below 0.5 suggests a dominant role of avalanche ionization in catastrophic damage formation.

Fatigue analysis showed that catastrophic damage exhibits a clear dependence on pulse duration at both wavelengths, whereas color change fatigue was largely insensitive to pulse duration. This insensitivity is consistent with an MPA-driven mechanism, as color changes were not observed for pulse durations longer than 10 ps. In contrast, the pulse duration dependence of catastrophic damage may reflect the additional influence of avalanche ionization, particularly at longer pulse durations.

4. Impact of nonlinear absorption on LIDT

Previous experiments on LIDT and the investigation of different damage modes have indicated that absorption may play a significant part in the damage formation, especially for the color change damage mode. As such, careful consideration of these factors is essential when designing coatings for advanced laser systems. While the general mechanisms of absorption in transparent materials are well established, their specific impact on LIDT and optical lifetime remains an active area of research. To understand the influence of absorption, it is first necessary to investigate its temporal evolution and dependence on laser parameters. Therefore, this Chapter focuses on both linear and nonlinear absorption behavior in dielectric coatings and how it varies with laser intensity, wavelength, and pulse duration.

The work presented in this Chapter is based on paper [**A2**] and unpublished data, and was also presented at conferences [**C6**], [**C7**] and [**C12**].

4.1 Nonlinear absorption behaviour in dielectric coatings

Motivation

The intense optical fields produced by laser systems subject optical components to significant stress. These effects are especially critical in dielectric and metallic coatings, which, while essential for controlling reflection, transmission, and dispersion, inevitably absorb a portion of the incident light. This absorbed energy is converted into heat, leading to gradual performance degradation and ultimately limiting the maximum achievable power and operational lifetime of the system. This degradation is largely driven by laser-induced absorption processes. As intensities increase, nonlinear absorption mechanisms – such as multiphoton absorption – begin to dominate over linear processes, introducing additional challenges for preserving optical performance.

To address these challenges, and in response to the growing demand for high-power ultrafast lasers in industrial and scientific applications, many studies have focused on measuring and understanding nonlinear absorption. These efforts aimed to clarify how laser and material parameters influence the onset and progression of optical damage.

While the fundamental principles of nonlinear absorption phenomena are well established, several aspects related to optical coatings remain insufficiently

understood. This is due to multiple contributing factors. First, because optical coatings are typically thin and exhibit very low absorption, extended integration times are required to detect measurable thermal responses using most absorption measurement techniques [30, 54]. Investigating nonlinear effects further necessitates the use of both high intensity and high average power. As a result, acquiring a single absorption data point often requires continuous laser exposure over several minutes, during which thermal or structural changes in the coating may occur. Second, optical coatings are not perfectly homogeneous. They contain intrinsic defects and impurities [49, 52, 152] and consist of multiple layers composed of different materials. This inherent complexity impedes systematic absorption studies [32, 153–155].

To examine the effects of thermal and laser annealing, as well as the influence of pump wavelength on nonlinear absorption, a case study was conducted using single-layer hafnia coatings in both as-deposited and thermally treated states (RT, 350°C and 500°C, see Table 2.1). The measurements were performed using a highly sensitive PCI technique [132]. A high-power laser source operating at wavelengths of 1064 nm, 532 nm, and 355 nm, with repetition rates of 1 MHz and 400 kHz and a pulse duration of 10 ps, was employed. The experimental results are further supported by an analysis of the nonlinearity order and are discussed in detail to provide a comprehensive understanding of the observed absorption behavior.

Analysis of nonlinear response

For the interpretation of absorption data, both linear and intensity-dependent MPA mechanisms are considered [30, 49, 53, 54]:

$$\alpha = (\alpha_0 + \sum_{\mathrm{n}=1}^{\mathrm{m}} \beta_{\mathrm{m}} I^{\mathrm{m}}) \times h. \tag{4.1}$$

Here, α_0 denotes the linear absorption coefficient, β_{m} represents the m-th order nonlinear absorption coefficient, and $m = \lfloor \frac{E_{\mathrm{g}}}{h\nu} \rfloor$ is the number of photons required for the MPA process (E_{g} is the material bandgap, and $h\nu$ is the photon energy). The parameters I and h correspond to laser intensity and coating thickness, respectively. Since absorption coefficients depend on thickness, h is explicitly included in the model [30, 54]. The MPA process occurs when the total energy of m photons equals or exceeds the bandgap; however, nonlinear responses sometimes appear at lower photon orders, implying sub-bandgap states may be involved. Photon energies used here were 1.17 eV (1064 nm), 2.33 eV (532 nm), and 3.49 eV (355 nm). For each sample and wavelength, the effective MPA order was first identified, then Eq. 4.1 fitted to data including all terms up to that order. MPA is defined by its highest contributing order. α_0 and β_{m}were treated as free fitting parameters, while I and h were fixed. The

parameter α_0 captures the linear absorption, the coefficient β_m determines the slope and magnitude of the nonlinear absorption contribution.

Results

Spectral analysis

The investigation began with evaluating linear absorptance via reflection and transmission measurements for all three coatings (transmission-reflection measurement methodology is described in Sec. 2.5). Bandgap values were estimated by tangential fitting to the linear region of the absorption edge spectrum (Fig. 4.1), with extracted E_g values for HfO_2 agreeing with those in [53, 156]. Thermal annealing at 350°C increased the bandgap by about 1 eV (Table 2.1), while annealing at 500°C caused only a slight further increase and reduced the UV refractive index. The absorption spectrum's bending toward lower pho-

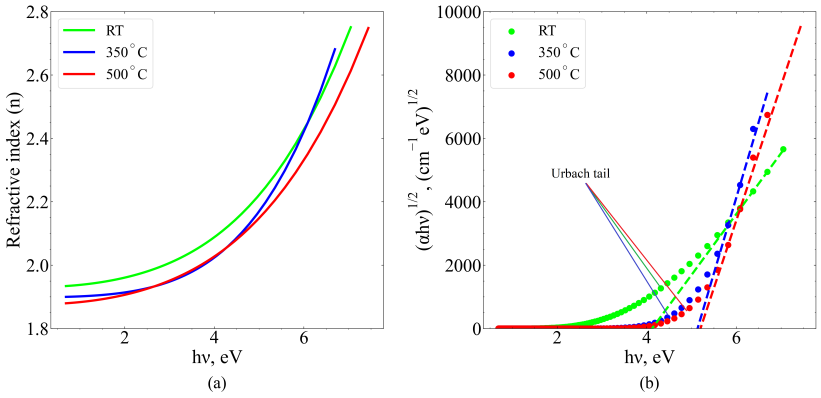

Figure 4.1: Spectral characteristics of HfO_2 thin films: (a) – refractive index dependence on the wavelength, (b) – bandgap evaluation using Tauc method at different annealing temperatures according to [52].

ton energies suggests impurities or structural disorder, linked to the Urbach tail [52, 157], indicating mid-gap states in as-deposited coatings, possibly from incomplete oxidation. Similar trends of increasing bandgap and decreasing absorptance with annealing have been reported [51, 156], with the Urbach tail's endpoint in annealed films aligning with the as-deposited optical bandgap. In nonlinear absorption, the Urbach tail may affect multiphoton absorption, causing a lower apparent order than expected from the nominal bandgap.

Characterization of temporal absorptance

As described in Sec. 2.4, two measurement protocols were employed to assess coating absorptance. Figure 4.2 shows Time-scan results at the highest intensity for each wavelength. The initial signal peak or dip corresponds to

repositioning the sample to a fresh site. Absorptance increases with decreasing

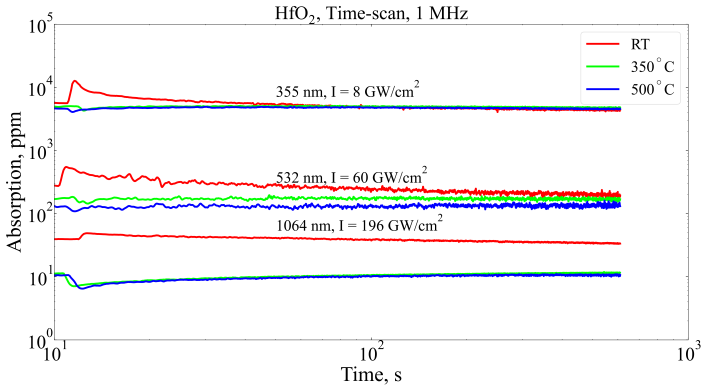

Figure 4.2: Raw time-scan data for HfO_2 RT, 350°C and 500°C samples at 1064 nm, 532 nm and 355 nm. The initial peak indicates the measurement start by moving the sample to the fresh site.

wavelength due to HfO_2 spectral properties. At 1064 nm, absorptance is minimal; it rises sharply near the band edge as photon energy increases. Longer wavelengths require higher intensities to induce nonlinear absorption. RT coatings show high initial absorptance that gradually decreases, likely from laser annealing via shallow defect excitation and localized heating [51, 52, 55, 56], potentially completing oxidation during repeated low-intensity exposure.

Annealed coatings start with low absorptance that grows over time, indicating cumulative processes like multiphoton-induced bond-breaking and defect formation via STEs [63, 65, 87, 94, 158, 159]. These long-lived excitons accumulate with repeated pulses. Typical oxide shallow traps manifest as spectral tails near the bandgap [87, 94, 158, 159]. Defects relax through delocalized and localized carriers [158], promoting color center formation and cumulative absorption increases.

Color center formation may also occur in RT samples, but emerges only after extended exposure (data not shown). While laser annealing reduces absorptance initially, cumulative absorption grows in annealed coatings under the same conditions. At low intensities, annealing dominates; at higher intensities, multiphoton absorption generates mid-gap states, driving cumulative absorptance increase.

Nonlinear absorption and laser annealing

To illustrate the difference between Time-scan (average of the last 10 s where the absorptance signal is stable) and T-scan measurements, as well as the effect of repetition rate, absorptance results at 355 nm are first examined. Figure 4.3 shows both scan types for two pulse repetition rates.

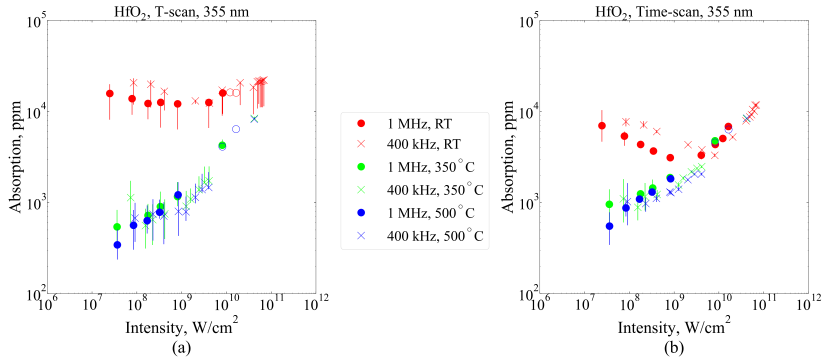

Figure 4.3: Comparison of absorptance at 1 MHz and 400 kHz at 355 nm. (a) – T-scan comparison, (b) – Time-scan comparison.

For the RT sample, T-scan data at 1 MHz (Fig. 4.3(a)) show a decrease in absorptance with increasing intensity, stabilizing at a minimum – indicative of laser annealing reducing linear absorption. A similar trend is seen in the Time-scan data (Fig. 4.3(b)), though with lower overall absorptance, due to annealing effects over time. At 400 kHz, nonlinear absorption at high intensities appears suppressed, likely masked by dominant linear absorption and concurrent annealing. In contrast, thermally annealed samples show no annealing and minimal linear absorption, with absorptance increasing across the entire intensity range due to nonlinear effects.

When Time-scan values exceed those of the T-scan, it suggests a strong cumulative absorption process. The T-scan data for annealed samples show little dependence on repetition rate, whereas the Time-scan indicates faster annealing in RT samples at 1 MHz. This may be related to the higher thermal load the material experiences at a higher repetition rate. Additionally, the PCI system benefits from reduced noise at higher average power, making 1 MHz preferable for accuracy. Therefore, subsequent measurements were conducted at this repetition rate.

Effect of pump wavelength

Figure 4.4 summarizes T-scan and Time-scan absorptance data for all samples at three wavelengths, with Time-scan values taken after 10 minutes of irradiation. The general trends observed in Fig. 4.3 are confirmed across all wavelengths. At 1064 nm, absorption remains largely linear across the intensity range, and laser annealing effects are minimal due to the low absorptance level. Limited laser power prevented reaching nonlinear absorption during T-scans, although some nonlinear behavior emerged in thermally processed samples following temporal exposure. This suggests that linear absorption dominates at this wavelength, and temperature rise is insufficient to drive annealing effi-

ciently.

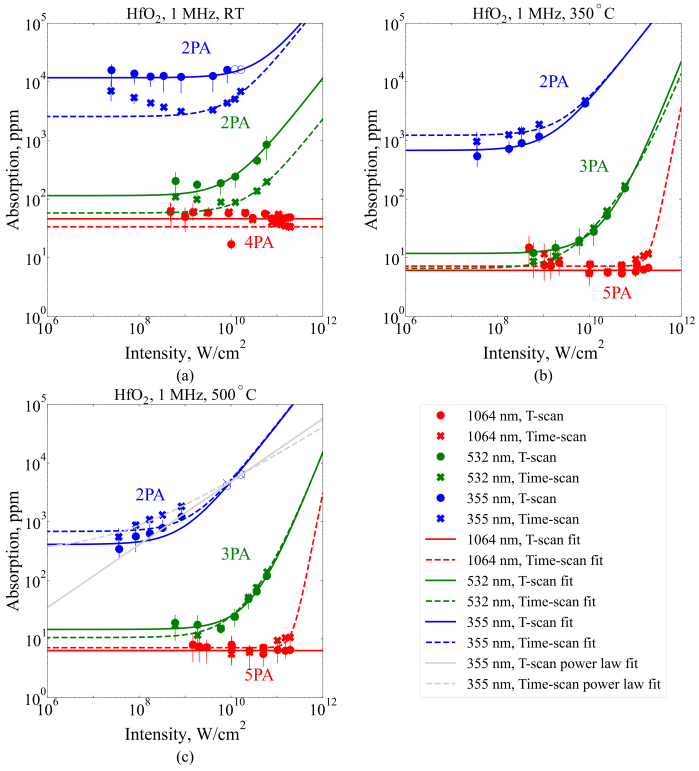

Figure 4.4: Absorptance data for HfO_2 thin films at 1064 nm, 532 nm, and 355 nm for each measurement protocol: (a) – room temperature, (b) – low temperature annealing, (c) – high temperature annealing. Solid lines represent T-scan data fit and dashed lines represent time-scan data fit using Eq. (4.1). Grey lines represent an empirical power-law fit of nonlinear absorption at 355 nm.

In contrast, 355 nm and 532 nm showed significantly stronger laser annealing due to higher absorptance and resultant local heating. At 355 nm, two high-intensity T-scan points deviated from the trend, likely due to system response lag and fast annealing (fastest measurement integration time was 100 ms, meaning 10000 pulses passed before the first data point is recorded). These points were excluded from further analysis. Notably, in thermally processed coatings, Time-scan and T-scan results aligned well – except at 355 nm, where a pronounced absorptance increase was observed, attributed to color center formation. At high intensities, T-scan and Time-scan absorptance converged, indicating that nonlinear absorption becomes dominant and linear contributions diminish.

Polynomial fitting was applied (from Eq. (4.1)) to derive the dominant multiphoton absorption order (XPA, where X stands for a number of photons), with results shown in Table 4.1. Absorption behavior generally followed a transition from linear to nonlinear regions, influenced by wavelength and annealing. At 532 nm, a mixed 2PA/3PA response was observed, while at 355 nm for the 500°C sample, deviations from the 2PA trend prompted an empirical power-law fit $A = xI^y$ (x and y are fitting parameters). The resulting exponents – 0.54 for T-scan and 0.47 for Time-scan – closely matched the photon-to-bandgap energy ratio.

Table 4.1: Linear and nonlinear coefficients according to the absorption model, $\alpha_0 = [\mathrm{cm}^{-1}]$, $\beta_\mathrm{m} = [\mathrm{cm}^{2\mathrm{m}-1}/W^\mathrm{m}]$.

Sample	**Scan type**	**1064 nm**		**532 nm**			**355 nm**	
HfO_2		α_0	$\beta_4 \times 10^{-46}$	α_0	$\beta_1 \times 10^{-11}$	$\beta_2 \times 10^{-22}$	$\alpha_0 \times 10^{1}$	$\beta_1 \times 10^{-8}$
RT	T	1.77	-	4.39	43.88	-	44.94	1.00
	Time	1.29	-	2.22	8.68	-	9.80	0.91
350°C	T	0.22	-	0.44	4.18	7.62	2.49	1.63
	Time	0.26	1.37	0.24	7.33	4.33	4.50	1.61
500°C	T	0.23	-	0.54	3.18	5.33	1.88	1.63
	Time	0.26	1.14	0.39	4.63	5.12	3.25	1.67

While literature values for nonlinear constants in dielectric coatings are limited, our results align well with reported 2PA and 3PA values for HfO_2 by Chen et al. [53]. Studies accounting for coating thickness also report comparable nonlinearity magnitudes [30, 54]. Overall, nonlinear and linear absorption behaviors vary significantly with coating process conditions, and annealing generally reduces both coefficients, in line with trends observed in [52].

Discussion

This study investigated how absorption in HfO_2 dielectric coatings evolves during laser exposure, with particular attention to its dependence on pulse duration and exposure history. The primary objective was to discern whether and how sub-threshold absorption behavior – prior to the onset of LID – scales temporally. Time-resolved photothermal common-path interferometry measurements revealed two distinct processes:

- A reduction in absorptance attributed to local laser annealing, observed predominantly in as-deposited coatings.
- An increase in absorptance due to cumulative defect generation, more prominent in thermally annealed coatings.

These findings show that both mechanisms can coexist but exhibit different dominance depending on the initial film condition and irradiation history.

Prior studies have focused on extracting nonlinear absorption coefficients, such as two- and three-photon absorption, using techniques like Z-scan [32, 47] and calorimetry with ArF lasers [30]. These studies highlighted dependencies on film thickness and substrate type [53], suggesting that nonlinearity is a complex interplay of material and structural parameters. However, these techniques are inherently limited by slow data acquisition and lack of temporal resolution [48]. In contrast, the photothermal methods provide enhanced temporal insight. Prior work using photothermal heterodyne imaging showed a steady decline in absorption in HfO_2 under prolonged exposure, attributed to structural reorganization rather than surface damage [55].

The observed decrease in absorptance during the initial stages of irradiation, especially in as-deposited coatings, is interpreted as local laser annealing. This phenomenon likely corresponds to the finalization of oxidation processes or the rearrangement of sub-bandgap defect states. The fact that atomic force microscopy measurements in previous studies reported no surface morphology changes further supports the hypothesis of atomic-level structural refinement rather than material removal or roughening [55]. Conversely, the gradual increase in absorptance seen in annealed films aligns with cumulative defect generation. At higher intensities, nonlinear excitation – e.g., via 2PA – can lead to electron trapping and the formation of color centers. These defects elevate sub-bandgap absorption, particularly under repeated or prolonged exposure [63]. The stronger influence of this effect in thermally treated samples suggests a reduced initial defect density, allowing laser exposure to act as a primary driver of defect creation. Most importantly, the current study demonstrated that both processes – laser annealing and increasing absorption – can happen simultaneously; however, the laser annealing influence is negligible in annealed coatings.

While the present study offers new insight into time-dependent absorption dynamics, several limitations remain. Quantitative modeling of competing mechanisms was not addressed in this work. A coupled rate-equation model incorporating thermal diffusion and defect-state population kinetics would provide a more predictive framework. Additionally, the assignment of sub-bandgap absorption to defect states was based on indirect evidence, such as deviations in multiphoton absorption order, without direct spectroscopic validation. This limits the certainty with which the contribution of mid-gap states can be characterized and calls for complementary studies using methods such as photoluminescence or electron paramagnetic resonance.

The ability to monitor real-time absorption changes under laser irradiation reveals the presence of both beneficial and detrimental processes that shape the long-term behavior of dielectric coatings. The balance between laser-induced

annealing and defect generation is not fixed but tunable via repetition rate, intensity, and prior thermal treatment. These findings emphasize the importance of dynamic, time-resolved characterization techniques in assessing the true optical resistance of materials used in high-power laser systems.

Conclusions

This study investigated the nonlinear optical characteristics of single-layer hafnia coatings fabricated via IBS and subjected to three post-deposition treatments: as-deposited, annealed at 350°C, and annealed at 500°C. Nonlinear absorption measurements conducted across wavelengths from 1064 nm to 355 nm revealed distinct intensity-dependent behaviors. Specifically, the weakest nonlinearity, scaling approximately as I^1 (indicative of two-photon absorption), was observed at 355 nm, while a combination of I^1 and I^2 dependencies – suggesting simultaneous two- and three-photon absorption – was identified at 532 nm.

Time-scan analysis indicated the presence of two concurrent mechanisms during laser exposure: laser-induced annealing, which reduced overall absorptance, likely by mitigating shallow defect states, and bond-breaking, likely followed by the formation of color centers, which increased absorptance. These findings highlight the interplay between thermal and electronic processes in determining the dynamic absorption behavior of hafnia coatings under high-intensity irradiation from 1064 nm to 355 nm.

4.2 Nonlinear absorption dependence on pulse duration

Motivation

Absorption is one of the key processes initiating laser-induced damage in high-power dielectric optical materials [6, 27]. At high intensities, the simultaneous absorption of multiple photons promotes electrons from the VB to the CB. If the electron density becomes sufficiently high, avalanche ionization may occur, rapidly increasing free carrier density and potentially causing damage [27].

To simulate MPA-induced plasma generation in dielectric materials, rate equation models have been developed [6, 34, 35, 100]. These models are often used to accurately predict single-shot LIDT and its scaling with pulse duration in the femtosecond to nanosecond regime. However, they do not account for cumulative effects under multi-pulse or prolonged irradiation effects, which often lead to laser-induced fatigue [10, 15, 93].

To address long-term behavior of optics, these models have been extended to include energy absorption via intermediate defect states within the bandgap,

allowing predictions for fatigue and cumulative damage [75, 87]. Possible defect states – formed by oxygen vacancies [61], dangling or broken bonds [59, 60], or laser-induced lattice disruptions [62, 63] – act as absorption centers that accumulate during irradiation and progressively increase absorptance [10]. Mann et al. demonstrated that absorptance in CaF_2 crystal increases with pulse count until damage occurs [160]. Conversely, some studies report absorption decrease due to laser conditioning or localized annealing [55, 56, 58]. Previous work in this dissertation has shown that increasing and decreasing absorption mechanisms can co-exist and evolve dynamically over time.

These findings suggest that absorption is not static but evolves with irradiation parameters and time. For example, Samad et al. showed that the nonlinear absorption coefficient and refractive index of TiO_2 nanoparticles increased with ablation duration [161]. At the same time, analogous changes in optical properties were reported in semiconductors [162, 163].

The consequences of such absorption-driven material modifications are strongly pulse-duration- and wavelength-dependent [6, 13, 34, 94, 99]. Yet most existing studies focus on time-averaged properties, overlooking the temporal dynamics of absorption during laser exposure – an essential factor in real-world system performance. Conventional models assume absorption depends on material bandgap and intensity, suggesting pulse-duration independence. However, when material contains localized defect states and is irradiated for a long time, the nonlinear response is not only a function of intensity but also total exposure history.

To address this gap, the pulse duration-dependent nonlinear absorptance in three dielectric coatings (thermally annealed single-layer HfO_2, SiO_2, and a two-layer AR HfO_2/SiO_2 coating) was investigated. The temporal absorptance was measured using PCI at UV wavelengths (355 nm and 343 nm), employing a 1 MHz laser source with a beam diameter of $\sim$60 μm at $1/e^2$ level and pulse durations ranging from 170 fs to 10 ps. The experimental results are directly compared to classical electron generation models with and without the consideration of the intermediate states to assess their predictive validity.

Results and discussion

Figures 4.5A) – C) present Time-scan absorptance (average of a 10 min measurement) as a function of fluence for pulse durations ranging from 170 fs to 10 ps. Across all coatings, three characteristic regions are observed: (1) a decrease in absorptance at low fluences (notably in SiO_2), (2) a fluence-independent linear regime, and (3) a nonlinear increase at higher fluences. At 2 ps, nonlinear absorption could be obtained only in the HfO_2 single-layer coating, while in SiO_2 and AR coatings, absorption remained linear. Therefore, 2 ps results are not shown for these two coatings.

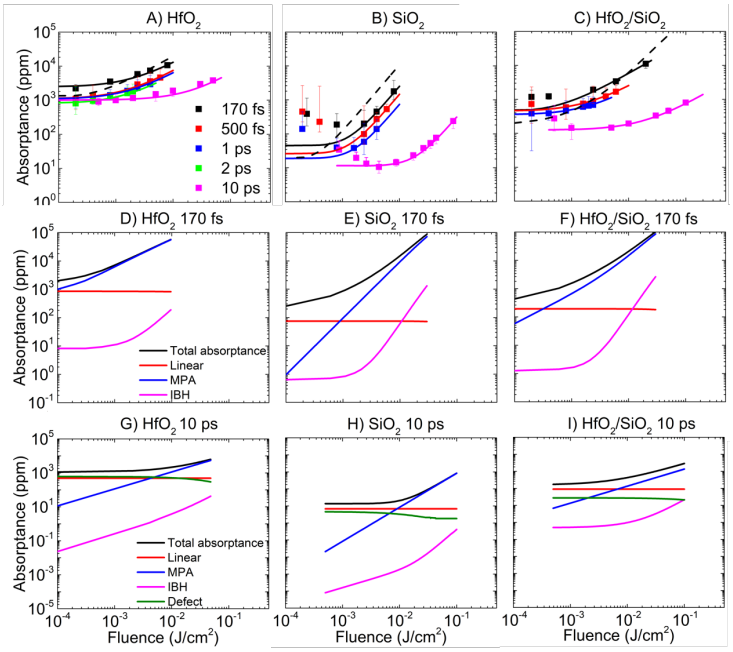

Figure 4.5: Time-scan absorptance as a function of fluence for A) HfO_2, B) SiO_2, and C) AR HfO_2/SiO_2 coatings. The dashed lines represent Eq. 4.3 simulations without Eq. 4.4, where D) – F) illustrate the contribution of each absorption mechanism to the total absorptance in each coating at pulse durations of 170 fs (highest peak intensity). The solid lines represent absorptance approximations using the full model in Eq. 4.3, where G) – I) represent the contribution of each absorption mechanism at 10 ps (most effective laser annealing).

In Fig. 4.5A), the absorptance of the HfO_2 coating converges to a similar linear absorption level across pulse durations. By contrast, SiO_2 (Fig. 4.5B)) exhibits different linear absorption levels and an anomalous increase of absorptance with decreasing fluences, attributed to laser annealing effects [55, 58]. This behavior aligns with previous study in this dissertation, linking absorptance reduction to thermally driven oxidation processes (see Sec. 4.1). The AR coating (Fig. 4.5C)), consisting of HfO_2 and SiO_2 layers, displays a behavior reflecting contributions from both materials.

To characterize energy deposition and find different effect contributions, rate equation model was employed, which is based on MPA, free carrier absorption, carrier recombination, and absorption via an intermediate defect state:

$$\frac{dI}{dz} = -\alpha I - \beta_{\mathrm{K}} I^{\mathrm{K}} - \sigma(\rho_0 + \rho) I - \sigma_{\mathrm{Kd}} I^{K_{\mathrm{d}}} \rho_{\mathrm{d}} \tag{4.2}$$

$$\frac{d\rho}{dt} = \frac{\alpha I}{\hbar\omega} + \frac{\beta_{\mathrm{K}} I^{\mathrm{K}}}{K\hbar\omega} + \frac{\sigma(\rho_0 + \rho) I}{\hbar\omega} + \frac{\sigma_{\mathrm{K_d}} I^{K_{\mathrm{d}}} \rho_{\mathrm{d}}}{K_{\mathrm{d}}\hbar\omega} - \frac{\rho}{\tau_{\mathrm{rec}}} \tag{4.3}$$

$$\frac{d\rho_{\mathrm{d}}}{dt} = -\frac{\sigma_{\mathrm{K_d}} I^{K_{\mathrm{d}}} \rho_{\mathrm{d}}}{K_{\mathrm{d}} \hbar\omega} \tag{4.4}$$

where *I(z, t)* is intensity of the propagating laser pulse within the coating, α is linear absorption coefficient, K is integer representing MPA order (integer ratio of the bandgap and photon energies), β_{K} is nonlinear absorption coefficient, $\hbar\omega$ is photon energy, $\rho(z,t)$ is the electron concentration excited to CB ($\rho(z, t = 0) = 0$), σ refers to cross-section of absorption via inverse bremsstrahlung (IBH), ρ_0 is intrinsic electron concentration, τ_{rec} is carrier recombination time, ρ_{d} is defect concentration in the intermediate state ($\rho_{\mathrm{d}}(z, t = 0) = \rho_{\mathrm{initial}}$, ρ_{initial} is initial density of defects), σ_{Kd} is the MPA cross-section of the defect state, and K_{d} is MPA order from the defect state (set to 1 in our case). The energy level of the defect state was such that single photon absorption was sufficient for electron excitation. The schematic of the

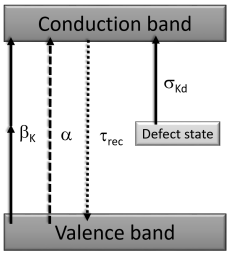

Figure 4.6: Schematic diagram of energy levels and transitions of a modeled wide-bandgap dielectric material.

electron transitions is illustrated in Figure 4.6. The recovery of the defect states was not modeled: it is assumed that defect state recovery rate is very low and takes much longer time than pulse duration. The Fresnel reflection from the surfaces was also included, accounting for real and complex refractive indices varying in time due to generation of quasi-free electrons in conduction band. The energy deposition was estimated for Gaussian beam profile accounting beam fluence distribution.

Firstly, the role of MPA was investigated, excluding the defect-induced absorption terms in Eqs. 4.2 and 4.3. A single set of material parameters was used in the simulations for each coating across the investigated pulse durations, as summarized in Table 4.2. For representative comparison purposes, only simulations at 170 fs for each coating are included, as the trends were similar at all investigated pulse durations.

The model without defect-induced absorption term (dashed lines in Figs. 4.5A) – C)) predicts steeper absorptance trends due to two-photon absorption (2PA) for HfO_2, three-photon absorption (3PA) for SiO_2, and a combination of 2PA/3PA for the AR coating compared to the experimental data.

To identify the source of the discrepancy, each absorption term in Eq. 4.3,

Table 4.2: Simulation parameters for single-layer coatings and AR layers from Eq. 4.3 excluding Eq. 4.4. ρ_0 denotes the fraction of the critical electron concentration.

	α, cm^{-1}	β_K, cm^{2K-3}/W^{K-1}	ρ_0	τ_{rec}, fs
HfO_2	35	5.27×10^{-8}	1×10^{-4}	3000
SiO_2	0.25	8.15×10^{-19}	1×10^{-5}	130

excluding Eq. 4.4, was analyzed (Figures 4.5D) – F)), showing that with the shortest pulse duration, linear absorption and MPA contribute comparably at low fluences, while MPA dominates at high fluences. Absorption due to IBH is negligible at 170 fs within the investigated fluence range. This suggests that a better model agreement with the data could be reached with a larger influence from the linear absorption.

The 2PA model for HfO_2 coating clearly resulted in an overly strong intensity dependence and deviated from the experimental data, therefore, the additional effect of the intermediate bandgap states on the nonlinear response was investigated. The experimental data could not have been accurately approximated using a single set of material parameters across all pulse durations due to the sensitive nature of the laser annealing to the pulse duration. Therefore, in the simulations, the linear and nonlinear absorption coefficients, and the density of defect concentration was varied (see Table 4.3). The rest of the simulation parameters were left unchanged.

Table 4.3: Fitting parameters for single-layer and AR coatings of HfO_2 and SiO_2. β_K units: for HfO_2 in 10^{-8} cm^{2K-3}/W^{K-1}, for SiO_2 in 10^{-19} cm^{2K-3}/W^{K-1}, and for respective layers in AR coating; ρ_d is in 10^{17} cm^{-3}; α is in cm^{-1}. $\sigma_{K_d} = 3.36\times10^{-17}$ cm^{2K}/W^{K-1} for HfO_2, $\sigma_{K_d} = 1.21\times10^{-16}$ cm^{2K}/W^{K-1} for SiO_2 and its layer in AR, $\sigma_{K_d} = 1.61\times10^{-17}$ cm^{2K}/W^{K-1} for HfO_2 layer in AR, $\alpha = 30$ cm^{-1} for HfO_2 layer and $\alpha = 10$ cm^{-1} for SiO_2 layer in AR coating.

τ, ps	HfO_2 (Single)			SiO_2 (Single)			HfO_2 (AR)		SiO_2 (AR)	
	α	β_K	ρ_d	α	β_K	ρ_d	β_K	ρ_d	β_K	ρ_d
0.17	20.0	2.81	25.27	1.00	2.09	0.0042	21.15	4.22	0.65	210.6
0.5	20.0	4.75	9.82	0.50	9.31	0.0012	26.36	3.38	0.65	84.26
1	13.0	7.56	9.82	0.20	18.61	0.0008	40.42	3.38	0.65	77.25
2	13.0	15.82	5.62	–	–	–	–	–	–	–
10	13.0	9.35	12.04	0.20	7.31	0.0013	17.15	1.96	0.60	52.21

The consideration of the additional absorption via defect state allowed reproducing the experimental behavior more accurately across all pulse durations. The model fits suggest that the effect of laser annealing, resulting in the minimum of linear absorption coefficient for the HfO_2 single-layer coating, decreases with increasing pulse duration (solid lines in Fig. 4.5A)). With shorter pulses, the laser annealing is weaker due to shorter interaction time during the irradiation (shorter pulse duration for the same repetition rate and Time-scan

duration results in a shorter effective irradiation period), which explains the highest linear absorption at 170 fs. Similar trends are seen for the SiO_2 and AR coatings, as shown in Figs. 4.5B) and C). In the case of the AR coating, the linear absorption coefficients for both layers were fixed, and only β_K (for the HfO_2 layer) and ρ_d (for both layers) were varied. This is reasonable, as the HfO_2 layer dominates the absorption and electron generation, and in multilayer coatings, the laser-induced damage typically initiates at the low-high refractive index layer interface [33].

Figures 4.5G) – I) illustrate the effect of 1PA transition from the defect state to the CB at 10 ps (lowest peak intensity and longest effective irradiation duration across investigated pulse durations). The results show that with increasing fluence, the absorption via defect state decreases, indicating saturable absorption [164].

Figure 4.7A) illustrates the pulse-duration dependence of the nonlinear absorption coefficient β_K, which increases across all coatings. A deviation observed at 10 ps is attributed to the use of a different irradiation wavelength (355 nm for 10 ps vs. 343 nm for 170 fs – 2 ps), reflecting a change in spectral response. The differences in β_K between the single-layer coatings and their corresponding layers in the AR structure are linked to differences in layer thickness – approximately 17-fold for HfO_2 and 4.5-fold for SiO_2. These thickness variations result in a one order of magnitude difference in β_K for HfO_2 and a several-fold difference for SiO_2, consistent with prior studies showing that nonlinear coefficients are thickness-dependent [30, 53]. These findings confirm

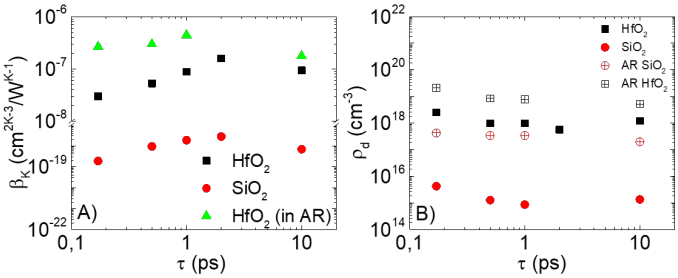

Figure 4.7: A) Nonlinear absorption coefficients obtained at every pulse duration from the numerical modeling for single-layer coatings and the HfO_2 layer in AR coating. B) Density of the defect states after the irradiation.

that the absorption behavior of dielectric coatings is not only pulse-duration dependent but also influenced by accumulated irradiation (i.e., pulse count). Longer pulses provide increased interaction time, which may enhance the depletion of defect states (see Fig. 4.7B)), thereby modifying the optical response of a material.

Discussion

Although previous studies have reported irradiation-time-dependent changes in nonlinear optical parameters [161–163], our findings reveal an additional sensitivity of laser annealing to pulse duration, highlighting a more nuanced evolution of material properties under realistic laser exposure conditions. The consideration of intermediate bandgap states introduced saturable absorption, which enabled a more accurate reconstruction of the experimental absorptance trends across all pulse durations. Future work should consider the role of local laser annealing during prolonged irradiation at low fluences in the linear absorption region, as well as incorporate more advanced electron generation models, such as those in Ref. [87], which include the full dynamics of both shallow and deep defect states.

Conclusions

Experimental results indicated that linear Time-scan absorption depends on the irradiation history, while nonlinear absorption also depends on pulse duration. Classical rate-equation models, which assume absorptance depends solely on peak intensity and neglect temporal changes in material properties, cannot fully explain the absorption dependence on pulse duration.

Theoretical modeling overestimated the absorption dependence on pulse duration compared to experimental data, indicating that an MPA-only model is insufficient. The results suggest the presence of at least two absorption processes, one of which may involve an additional defect level leading to saturable absorption. Incorporating defect-assisted single-photon absorption significantly improves agreement between the model and experimental data across all pulse durations.

5. Impact of absorption on the fatigue effect

The previous research presented in this dissertation has shown that material degradation under intense laser irradiation is a highly complex process involving multiple phenomena simultaneously. Fatigue evaluation in dielectric coatings for non-catastrophic color change damage indicated no observable fatigue limit, in contrast to the fatigue behavior associated with catastrophic damage. At the same time, theoretical considerations based on rate equations suggest that color change may evolve into catastrophic damage through MPI. The physical phenomena underlying the optical lifetime are still under investigation. Typically, lifetime can be roughly estimated using multiple S-on-1 tests. However, these tests often span only minute-long irradiation durations, which are relatively short compared to the thousands of hours typical in real-world optics operation. Alternatively, lifetime can be assessed by irradiating the component continuously for several hundred hours, but this approach is both time-consuming and cost-inefficient. The cumulative nature of the fatigue effect suggests that absorption processes play a critical role in the formation of long-term damage. Therefore, this Chapter will discuss the effect of absorption on the fatigue of optics.

The work presented in this Chapter is based on papers [**A3**] and [**A5**], and were presented at conferences [**C9**] – [**C11**], and [**C13**].

5.1 Role of absorbed dose in lifetime of optics

Motivation

Fatigue characterization is critical for predicting the lifetime of optical materials but remains experimentally demanding, requiring long-term irradiation and suitable predictive models. Short-term fatigue can be assessed via the S-on-1 method [11], which yields a characteristic LIDT curve as a function of pulse number. This multi-shot LIDT is typically lower than the single-shot threshold and, when combined with extrapolation models, can be used for rough lifetime prediction. However, current models largely focus on catastrophic damage, and no predictive frameworks exist for non-catastrophic fatigue.

Given the cumulative nature of fatigue and mounting evidence that absorption plays a critical role in damage formation, it is reasonable to consider that laser-induced fatigue may be governed by the overall irradiation dose accumulated over time. Building on previous work, this study investigates the relationship between laser-induced fatigue – an accumulative process linked to

both linear and nonlinear absorption – and the total absorbed dose required to initiate cumulative damage under various laser intensities and wavelengths. The focus is placed on fatigue associated with the color mode in two sets of single-layer dielectric coatings, HfO_2 and SiO_2 (RT 350°C and 500°C, see Table 2.1). Fatigue behavior is examined using S(10^7)-on-1 LIDT testing, complemented by absorption measurements via PCI across different irradiation conditions. By analyzing the correlation between fatigue onset and irradiation dose, this approach aims to support the development of a dose-dependent predictive framework for estimating the long-term durability of optical coatings under extended laser exposure.

Methods

For LIDT measurements, samples were irradiated using a Pharos laser (Light Conversion) at 1030 nm, 515 nm, 343 nm, and 258 nm, with 10 ps pulses at 50 kHz and a beam diameter of 60 μm ($1/e^2$ level). Post-irradiation, test sites were analyzed via Nomarski microscopy and categorized as undamaged, color-changed, or catastrophically damaged. Damage probabilities were determined for each pulse count, yielding characteristic curves for both damage modes. Since catastrophic damage was not the primary focus, it is included for comparison only.

Some limitations affected the color mode LIDT measurements: in certain coatings, LIDTs exceeded the substrate's self-focusing threshold, inducing nonlinear propagation, bulk damage, and surface breakthrough. For SiO_2, back-surface damage due to self-focusing was observed. No color change was detected at 258 nm for the 500°C sample, or at 515 nm for the 350°C and 500°C samples. In HfO_2, the color mode at 1030 nm appeared only in the RT sample. At 258 nm, thresholds beyond 10^5 pulses could not be determined due to detector sensitivity limits. Despite these constraints, general fatigue trends correlated with absorptance were identified.

Absorptance was measured at 1064 nm, 532 nm, 355 nm, and 266 nm using 10 ps pulses at 1 MHz and a 60μm beam diameter. T-scan and Time-scan (10 min exposure, 100 ms integration) protocols were used to assess immediate and time-evolving absorptance. While PCI provides absolute absorptance values *A(I)*, the absorption coefficient α was calculated using the Beer-Lambert law [26], neglecting reflection:

$$\alpha = \frac{-\ln(1 - A(I))}{h} \tag{5.1}$$

where α is the absorption coefficient, I is the peak intensity at which *A(I)* was measured and h is the physical thickness of the coating. Then, the absorption coefficient is plotted as a function of intensity and fitted with the following approximation [30, 49, 53, 54] to extract the linear and nonlinear absorption

coefficients for each sample at the wavelengths of interest:

$$\alpha(I) = \alpha_0 + \sum_{\mathrm{n}=1}^{m} \beta_{\mathrm{m}} I^{\mathrm{m}}. \tag{5.2}$$

Results and discussion

LIDT results

This section discusses damage threshold results for hafnium dioxide (HfO_2) and silicon dioxide (SiO_2). Figure 5.1 illustrates color changes in both materials after exposure to 10 million laser pulses.

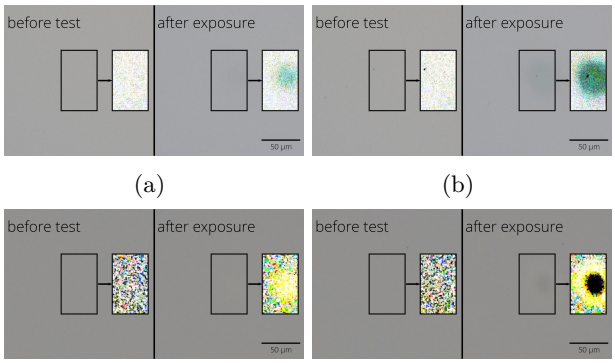

Figure 5.1: Typical morphological examples of color change at 10^7 pulses. SiO_2 – (a) 0.087 J/cm^2 and (b) 0.288 J/cm^2, HfO_2 – (c) 0.085 J/cm^2 and (d) 0.291 J/cm^2.

To quantify the fatigue phenomenon, both catastrophic damage thresholds and color changes were examined. Figure 5.2 shows characteristic damage curves for HfO_2 coatings. Catastrophic thresholds (differences between RT and annealed samples appear diminished due to the logarithmic scale) remain stable up to 10^7 pulses, while color change thresholds are significantly lower and decline with pulse count. This fatigue behavior is strongly wavelength-dependent. For instance, at 258 nm (Fig. 5.2(a)), the threshold declines steadily with pulse number, whereas at 1030 nm (Fig. 5.2(d)), color change appears only after 10^5 pulses. These findings support previous results suggesting that the color change threshold may approach zero with extended irradiation, posing reliability concerns for long-term laser operation. As high-power systems typically operate below the S-on-1 threshold, such fatigue-driven degradation can lead to performance loss well before catastrophic failure occurs [70]. Moreover, fatigue in HfO_2 weakens and is delayed at longer wavelengths, emphasizing the importance of spectral dependence.

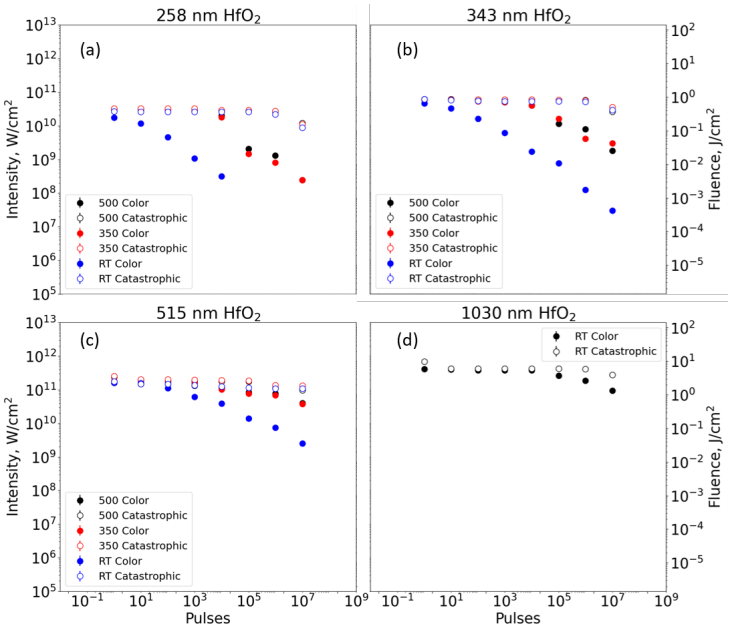

Figure 5.2: HfO_2 LIDT data of catastrophic and color damage modes for all three types of annealing. (a) – at 258 nm, (b) – at 343 nm, (c) – at 515 nm, (d) – at 1030 nm.

Annealing also plays a significant role: RT samples consistently show lower thresholds compared to annealed coatings, correlating with smaller bandgaps and higher absorptance. A reduced bandgap increases the probability of multiphoton excitation, contributing to the enhanced fatigue sensitivity in RT samples.

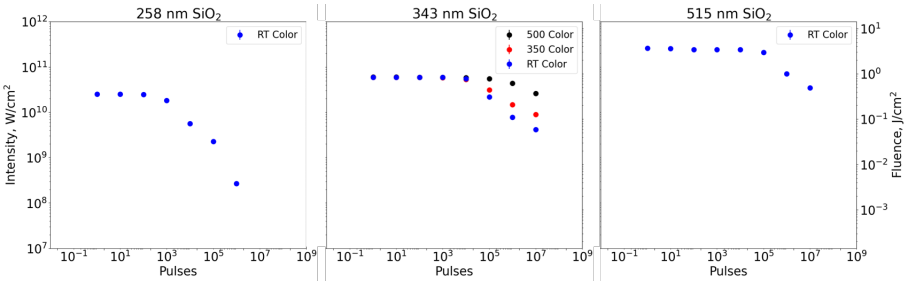

Figure 5.3: SiO_2 LIDT data of color damage mode for all three types of annealing. (a) – at 258 nm, (b) – at 343 nm, (c) – at 515 nm. Catastrophic data could not be obtained due to self-focusing.

SiO_2 coatings show similar wavelength-dependent fatigue behavior (Fig. 5.3), though differences between RT and annealed samples at 343 nm are less pronounced than in HfO_2.

These findings highlight the connection between color change, absorption, and bandgap in HfO_2 and SiO_2 coatings. Absorption under equivalent irradiation will be examined in the following sections. Consistent with prior studies, no clear onset is observed for color change damage – unlike catastrophic damage – indicating distinct mechanisms and the need for separate fatigue models [75, 87, 89].

Temporal absorption characteristics

The absorptance analysis begins with an overview of raw Time-scan data presented in Figure 5.4. Measurements were conducted at high relative intensities for each wavelength, remaining below catastrophic damage levels for at least 10 minutes. The initial peak or dip in the signal corresponds to the repositioning of the sample to a fresh site.

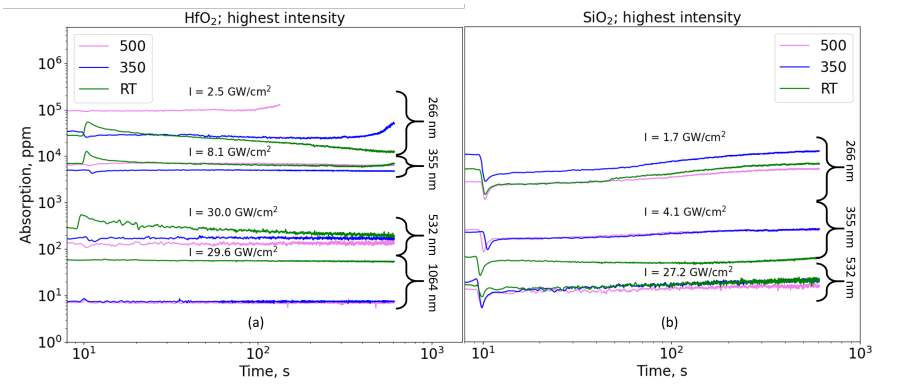

Figure 5.4: Time-scan data for HfO_2 samples at 1064 nm – 266 nm (a) and SiO_2 samples at 532 nm – 266 nm (b). The initial peak or dip marks the start of the measurement when the sample is repositioned to a fresh site.

At 1064 nm (Fig. 5.4(a)), the RT hafnia sample exhibits absorptance approximately an order of magnitude higher than that of the 350°C and 500°C samples, with no significant temporal variation. At 532 nm, the RT sample also shows higher initial absorptance, which decreases over time. In contrast, annealed samples display an initial dip followed by a rapid rise to a stable level. At 355 nm, the RT sample again demonstrates a decrease followed by a later increase. At 266 nm, the annealed samples show a more pronounced increase, with the 500°C sample measurement halted due to signs of imminent damage, as indicated by a sharp absorptance increase. The gradual reduction in RT absorptance is likely a result of localized laser heating and annealing, which enhance coating structure through improved oxidation [55]. The subsequent increase in absorption, particularly before damage onset, is consistent with cumulative defect incubation processes, such as the formation of long-lived STEs

and color centers under repetitive exposure [63, 65, 87, 94, 158]. Higher absolute absorptance at shorter wavelengths aligns with expectations based on proximity to the absorption edge, as previously reported for HfO_2 samples in Sec. 4.1.

For silica coatings, temporal variability is generally less pronounced than for hafnia. At 355 nm, a minor decrease followed by an increase is observed only in the RT sample (Fig. 5.4(b)). In all other cases, absorptance consistently rises over time. Thermal treatment has less effect on silica coatings, with absorptance values at 532 nm remaining comparable across all samples. At 355 nm, thermally treated silica coatings unexpectedly show higher absorptance than RT, and at 266 nm, the 350°C sample surpasses both RT and 500°C variants. This wavelength sensitivity suggests complex behavior requiring further investigation.

Nonlinear absorption

Nonlinear absorption was investigated using T-scan and Time-scan protocols as a function of peak intensity. Absorption coefficients were derived from absorptance using Eq. 5.1 and are summarized in Figs. 5.5 and 5.6 for single-layer hafnia and silica coatings, respectively. For Time-scan data, reported values

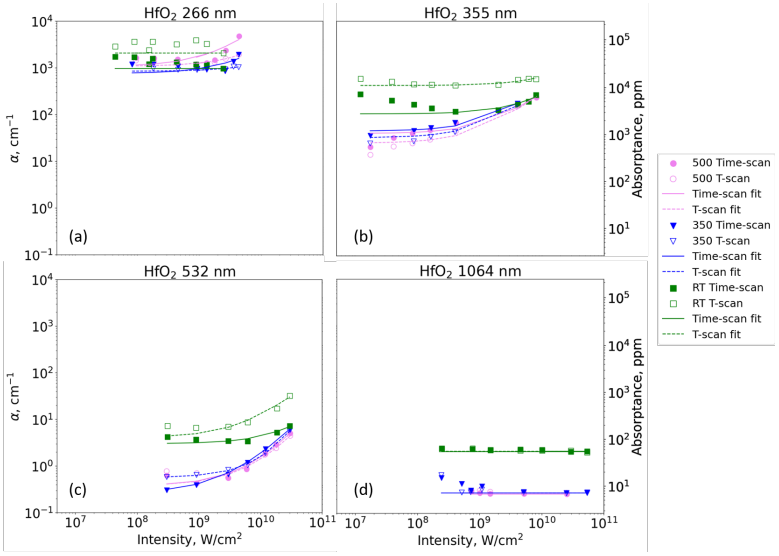

Figure 5.5: HfO_2 absorption coefficient as a function of intensity. (a) 266 nm, (b) 355 nm, (c) 532 nm, (d) 1064 nm. Dashed lines represent the MPA approximation for T-scan data; solid lines for Time-scan data.

represent the average over the final 10 s of the measurement. T-scan and Time-scan results were compared to evaluate linear and nonlinear absorption behavior and assess laser annealing effects. The absorptance behavior is first

discussed in detail for hafnia coatings at 355 nm.

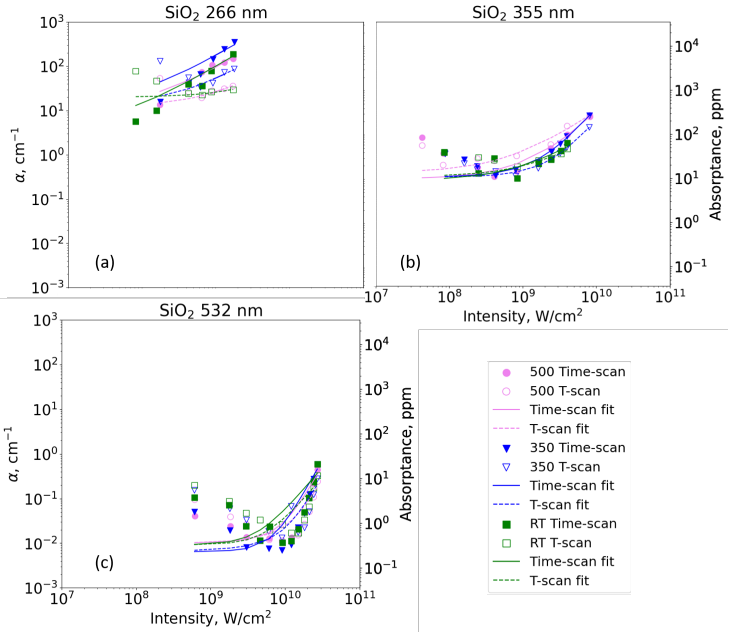

Figure 5.6: SiO_2 absorption coefficient results. (a) 266 nm, (b) 355 nm, (c) 532 nm. Dashed lines represent the MPA approximation for T-scan data; solid lines for Time-scan data.

At 355 nm (Fig. 5.5 (b)), the RT hafnia sample shows the highest absorption in T-scan measurements, remaining nearly constant, while Time-scan data reveal decreasing absorption with intensity and lower absolute values – consistent with progressive laser annealing [51, 58]. Nonlinear absorption becomes apparent in Time-scan data at higher intensities, but no annealing effects were seen in thermally treated samples.

Similar trends are observed at other wavelengths. At 532 nm (Fig. 5.5 (c)), behavior mirrors that at 355 nm. At 266 nm (Fig. 5.5 (a)), RT samples show one-photon absorption ($E_g = 4.12$ eV, $E_p = 4.66$ eV), with weak intensity dependence in T-scan data. MPA fitting for annealed samples was inaccurate, possibly due to the onset of avalanche ionization. However, Time-scan absorption again decreases with intensity due to strong laser annealing. At 1064 nm (Fig. 5.5 (d)), all coatings exhibited purely linear absorption, as the available intensity was insufficient to induce nonlinearity.

Absorption measurements for SiO_2 coatings (Fig. 5.6) revealed trends similar to those observed in hafnia samples. However, the MPA fit curves at 266 nm (Fig. 5.6 (a)) and 532 nm (Fig. 5.6 (c)) cannot fully align with the data due to strong annealing, possible self-focusing in the back of the substrate, and a combination of multiphoton and avalanche ionization processes involved. These

effects are pronounced at the applied intensities, which are comparable to those used in S-on-1 measurements.

Laser annealing

This section examines the temporal evolution of absorptance in thermally untreated hafnia coatings subjected to laser irradiation at two wavelengths, 266 nm and 355 nm, with focus on annealing behavior (Fig. 5.7).

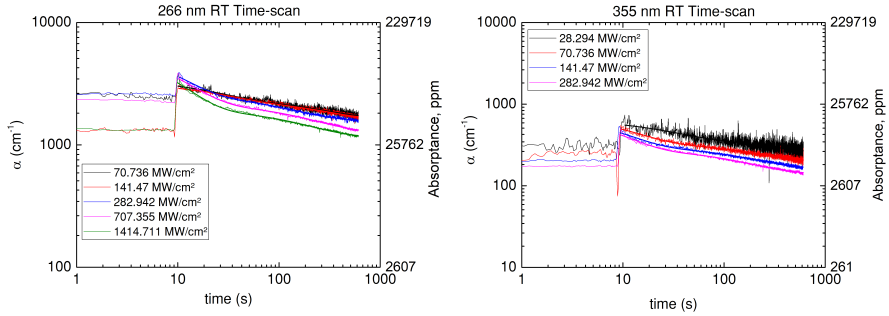

(a) (b)

Figure 5.7: Double exponent decay approximation for HfO_2 RT sample Time-scan data at 266 nm (a) and 355 nm (b) wavelengths.

The absorption signal diminishes non-uniformly over time and is described by a double exponential decay model [58]:

$$\alpha = y_0 + A_1 e^{-x/t_1} + A_2 e^{-x/t_2} \tag{5.3}$$

where x denotes the elapsed irradiation time in seconds; y_0 represents the lowest absorption coefficient attainable via laser annealing at a given intensity level; the sum of A_1 and A_2 defines the total change in absorption resulting from the annealing process; and t_1, t_2 are the characteristic fast and slow decay constants.

The time constants t_1 and t_2 reflect the multi-step nature of the annealing dynamics and vary with laser intensity (Fig. 5.8(a)). Both parameters are higher at lower intensities, decrease with increasing intensity, and eventually plateau at higher levels. This trend suggests a saturation of the annealing acceleration, beyond which further increases in intensity do not enhance the process.

The lowest achievable absorption level (y_0) decreases monotonically with intensity (Fig. 5.8(b)). This trend follows a power-law behavior and aligns well with the linear absorption coefficient determined from Eq. 4.1 in the Time-scan analysis. Thus, increasing either intensity or exposure duration

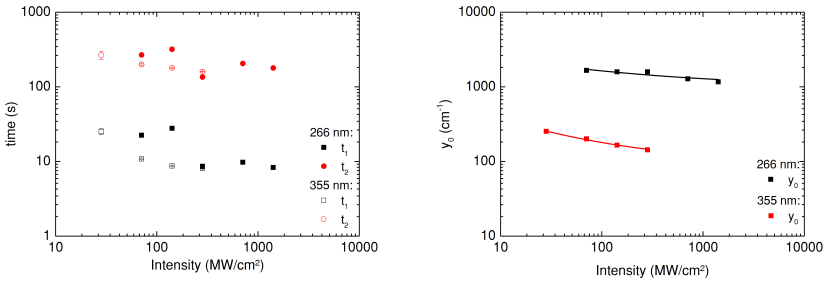

(a) (b)

Figure 5.8: Fitting parameters as a function of intensity for HfO_2 RT sample at 355 nm and 266 nm wavelengths: fast and slow decay constants (a) and onset absorption (b).

enables convergence toward the minimal absorption, allowing linear absorption of annealed coatings to be extrapolated from these results.

Despite the difference in absolute absorptance between 266 nm and 355 nm, the decay times at both wavelengths are comparable, indicating a likely common annealing mechanism. This is plausibly associated with linear absorption within localized states in the bandgap – such as the Urbach tail or defect states from incomplete oxidation.

Fatigue analysis

This chapter presents a framework for evaluating optical component lifetime below the single-shot color change LIDT. As previously discussed and consistent with earlier findings [14, 16, 88, 165], no clear onset of color mode damage was observed. Given the cumulative and deterministic nature of color change and its dependence on wavelength [14, 30, 75, 87, 92], the absorbed dose of irradiance in the S-on-1 regime can be defined as:

$$D_{\text{absorbed}}(I) = I_{\text{incident}} \times N \times A(I_{\text{incident}}), \tag{5.4}$$

where I_{incident} is the laser intensity at which damage occurs after N pulses, and *A(I)* is the absorptance at that intensity. Due to the time-dependence of absorptance, Time-scan measurements were used, averaging the last 10 seconds of exposure, when the absorption signal had stabilized. This approach was applied uniformly to all coatings and wavelengths. The RT HfO_2 sample is used as a representative example due to the most comprehensive data overlap.

Figure 5.9 (a) shows that the smallest total absorbed dose occurs at intensities near the respective 1-on-1 threshold (see Fig. 5.2), increasing with decreasing intensity. At low intensity, a deviation from trend is noted, where absorptance becomes linear. Two hypotheses are considered:

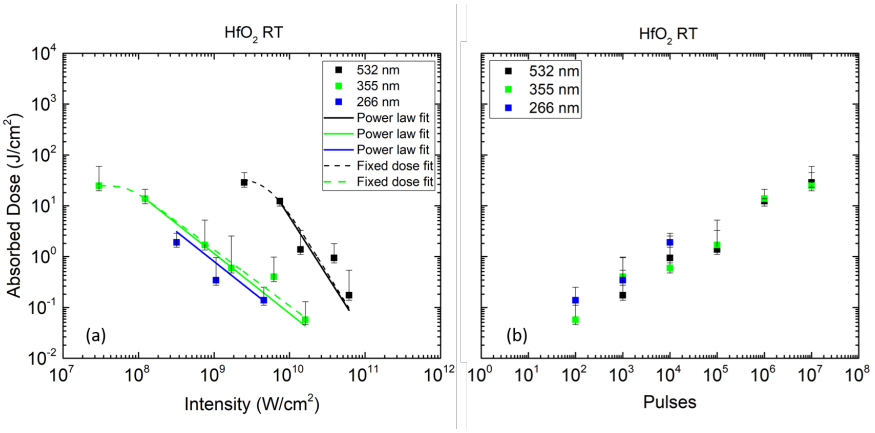

Figure 5.9: Absorbed dose as a function of intensity (a) and as a function of the number of pulses at threshold intensity (b) for HfO_2 RT sample.

1) A power-law only dose dependence on intensity:

$$D_{\text{absorbed}}(I) = cI_{\text{incident}}^{y} \tag{5.5}$$

where c, y are fitting parameters.

2) A composite model with constant dose at low intensity and power-law dependence above a critical intensity:

$$D_{\text{absorbed}}(I) = D_0 \left[1 + \left(\frac{I_{\text{incident}}}{I_{\text{crit}}}\right)^{\phi}\right]^{-\gamma}. \tag{5.6}$$

D_0 is a constant representing the total dose absorbed at the low intensity, I_{crit} indicates the critical intensity, where nonlinear absorptance becomes relevant, marking the shift from constant dose to power-law regions. D_0, ϕ, I_{crit}, and γ are fitting parameters.

Equations 5.5 and 5.6 are used to approximate the data illustrated in Fig. 5.9(a). The second model fits low-intensity data better, but neither can be definitively confirmed due to data limitations.

When total absorbed dose is plotted against pulse count (Fig. 5.9(b)), the values at threshold intensities show no wavelength dependence, suggesting a potential method for non-destructive lifetime estimation.

Using the knowledge of the total absorbed dose required to cause damage, an attempt is made to build a model that predicts the lifetime of optics. Assuming a power-law dose-intensity relationship, Eq. 5.4 and Eq. 5.5 are combined to predict the number of pulses required at a given intensity:

$$N(I) = \frac{D_{\text{absorbed}}(I)}{A(I) \times I_{\text{incident}}} = \frac{c I_{\text{incident}}^{y-1}}{A(I)} \tag{5.7}$$

where c, y and $A(I)$ are the free fitting parameters. Intensity-dependent absorptance can be expressed from Eq. 5.1 and Eq. 5.2:

$$A(I) = 1 - \exp\left[- \left(\alpha_0 + \sum_{\text{n}=1}^{m} \beta_{\text{m}} I_{\text{incident}}^{m} \right) h \right] \tag{5.8}$$

While approximating the total absorbed dose using Eq. 5.5, the exponent y was found to correlate with the material bandgap-to-photon energy ratio ($E_{\text{g}}/E_{\text{p}}$), potentially indicating the dominant MPA order. A similar observation was previously reported in the analysis of multiphoton absorption fitting exponents for hafnia coatings in Sec. 4.1. Substituting this observed relation into the equation yields:

$$N(I) = \frac{c I_{\text{incident}}^{\frac{E_{\text{g}}}{E_{\text{p}}} - 1}}{1 - \exp\left[- \left(\alpha_0 + \sum_{n=1}^{\text{m}} \beta_{\text{m}} I_{\text{incident}}^{\text{m}} \right) h \right]}. \tag{5.9}$$

The equation above introduces a simplified phenomenological model, describing how many laser pulses are required to induce the color change at the intensity of interest, depending on the material bandgap, the linear and nonlinear absorption coefficients, and the thickness of the coating. Although it is based on the power-law dose dependence assumption, other dose models, if known, can be used instead.

In this particular case, there is only one free parameter – c, which needs calibration for at least one data point of "time-to-failure" N at a given peak intensity I. Eq. 5.9 is applied to the experimental data using a least-squares method. Other model parameters can be estimated through non-destructive means. Once the coefficient c is determined, the lifetime of optics at lower intensities can be predicted – conditions that are otherwise difficult to assess experimentally due to the long exposure times required.

The predictive fatigue model of Eq. 5.9 (dashed 'Fatigue fit' curves) is compared in Fig. 5.10 to measured S-on-1 LIDT data and their empirical power-law fits (solid 'LIDT fit' curves), with both the fitted exponent y and the calculated E_g/E_p indicated. Overall, the model captures the low-intensity regime – its primary domain of interest – but shows deviations at higher fluences near the single-pulse threshold. For instance, in the RT HfO_2 coating at 355 nm and 532 nm (Figs. 5.10(c),(d)), it departs from both the LIDT measurements and

power-law behavior. Conversely, where linear absorption dominates (1064 nm and 266 nm; Figs. 5.10(a),(b)), the fatigue model closely parallels the empirical fit.

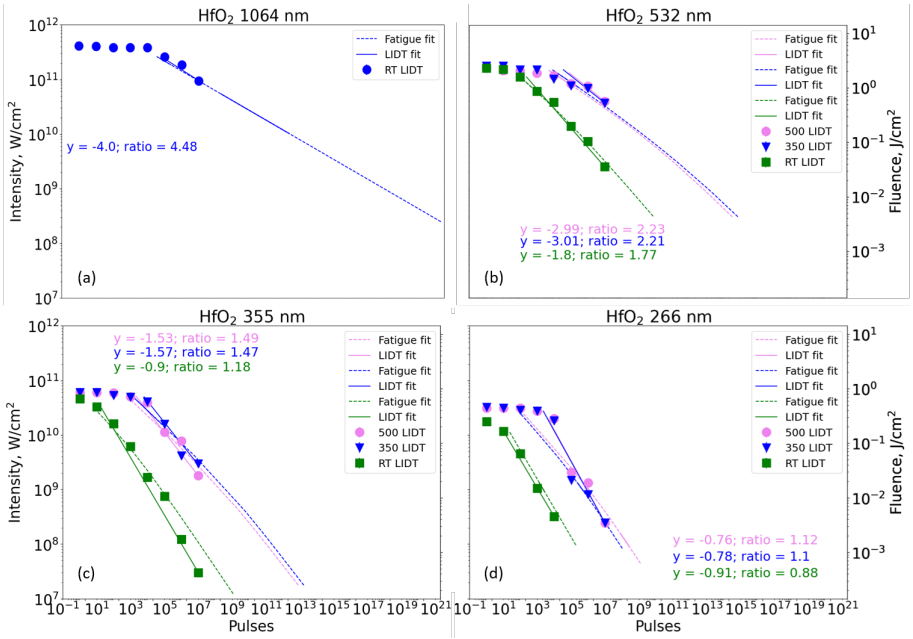

Figure 5.10: HfO_2 LIDT fit (solid lines) with Eq. 5.7 and fatigue extrapolation (dashed lines) with Eq. 5.9 at each wavelength. Colored text shows a comparison between the fitting parameter y and the *ratio* of the material bandgap and the photon energies.

When nonlinear absorptance is significant, the model reproduces the bend toward the 1-on-1 threshold – most clearly at 532 nm and 355 nm – yet discrepancies at 266 nm in annealed samples trace back to limited MPA region accuracy in Eq. 4.1 and uncertainties in the fitted parameters. Importantly, because the required absorbed dose is nearly constant across wavelengths, differences in absorptance alone account for the shift in fatigue behavior between untreated and annealed coatings. This confirms the cumulative, dose-dependent nature of color change fatigue – and reinforces the value of annealing in extending optical lifetime – even under predominantly linear absorption conditions.

Notably, color change is observed even where absorption is primarily linear, suggesting a dose-driven process relevant to CW damage as well. While nonlinear absorption accelerates this process, it may not be necessary to induce modifications. It also remains unclear whether color change progresses to catastrophic failure or simply results in spectral degradation.

For SiO_2, the model only succeeds at 355 nm, accurately predicting the bend of the fatigue curve toward the single-pulse limit. At 532 nm, it under-

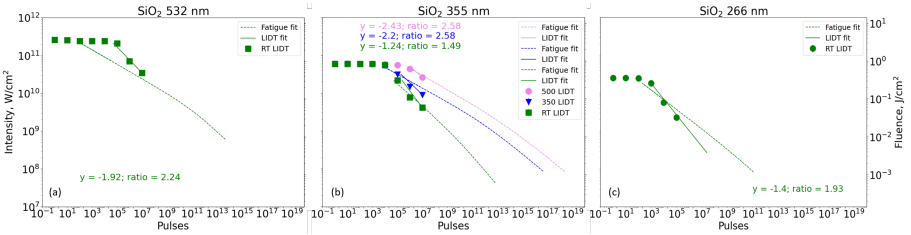

Figure 5.11: SiO_2 LIDT fit (solid lines) with Eq. 5.7 and fatigue extrapolation (dashed lines) with Eq. 5.9 at each wavelength. Colored text shows a comparison between the fitting parameter y and the *ratio* of the material bandgap and the photon energy.

predicts, and at 266 nm, it over-predicts fatigue, mirroring the discrepancies seen in annealed HfO_2 at 266 nm. These mismatches stem from both the MPA-approximation limits and challenges in measuring SiO_2 damage thresholds – complicated by difficult distinguishing the coating from the FS substrate and self-focusing – thereby undermining lifetime forecasts for the silica coatings.

Despite their phenomenological nature and inherent uncertainties, these absorbed dose and fatigue prediction models offer a valuable first-order framework for understanding and estimating the role of absorptance in long-term laser-induced degradation.

Discussion

This study investigated the long-term degradation of dielectric optical coatings by focusing on sub-catastrophic damage modes, particularly color change phenomena, and their relation to cumulative absorbed dose. While previous research has established that laser-induced fatigue is a cumulative process involving defect incubation [14, 75, 93, 146], most studies have emphasized catastrophic damage as the sole indicator of optical component failure. In contrast, this work demonstrated that non-catastrophic damage can either remain benign or precede catastrophic failure, depending on the underlying absorption mechanism.

A central contribution of this study was the implementation of PCI to monitor temporal absorptance at laser intensities comparable to those used in conventional LIDT measurements. This enabled direct estimation of the absorbed dose, providing a more accurate representation of the energy retained in the material than conventional metrics based on incident fluence alone.

The relevance of incident dose to optical degradation has long been acknowledged [160, 166, 167], with evidence showing that longer exposure at lower intensities leads to greater energy deposition. However, absorbed dose – the actual energy retained by the material – has not been systematically explored due to measurement challenges. Consequently, previous lifetime models

have remained incomplete, often relying on empirical scaling with shot number or catastrophic fatigue onset. Moreover, while several studies have observed color change as a precursor or byproduct of irradiation [14, 16, 53, 93, 146], it has typically been regarded as optically neutral, with minimal impact on device functionality. This assumption is increasingly inadequate, especially in high-precision applications where even minor changes in absorption can degrade optical performance.

This work introduced a phenomenological model based on intensity-dependent absorbed dose, which more accurately reflects the energy conditions under which color change occurs. The model offers a practical and scalable approach for lifetime prediction, particularly in applications involving extended sub-threshold exposure. It also underscores the necessity of measuring temporal absorption rather than relying on static, single-shot characterizations. Furthermore, the integration of PCI and LIDT measurements enables a multimodal diagnostic framework capable of identifying both benign and pre-failure damage modes. This represents a shift from purely threshold-based assessments toward mechanism-aware lifetime evaluations. However, the absorptance trends in SiO_2 coatings were found to be inconsistent and not fully explained, highlighting material-specific complexities that the model does not resolve. Specifically, the model does not account for potential self-focusing effects within the bulk substrate, which may distort absorptance measurements obtained via PCI and, in turn, compromise the reliability of the absorbed dose–based predictions.

Conclusions

In this study, the relationship between laser-induced color change fatigue and absorptance was investigated in single-layer HfO_2 and SiO_2 dielectric coatings deposited by ion beam sputtering, across a wavelength range of 1030 – 257 nm. Combining LIDT testing with nonlinear absorptance measurements, the results revealed that fatigue behavior is strongly wavelength-dependent. Materials exhibited higher absorptance at shorter wavelengths, particularly near their absorption edge, where lower-order multiphoton absorption processes dominate. Consistent with earlier findings, no clear threshold onset for color change damage was observed.

A key result of this work is that the absorbed dose required to initiate color change fatigue remains nearly constant across all investigated wavelengths for a fixed pulse duration and pulse count due to linear absorption. Furthermore, the total absorbed dose required for damage increases as laser intensity decreases due to nonlinear absorption. At intensities several orders of magnitude below the single-shot LIDT, the absorbed dose appears to converge toward a constant value, although additional investigations are needed to confirm this trend.

Time-scan measurements revealed a sharp increase in absorptance immedi-

ately preceding catastrophic damage, suggesting potential for predictive diagnostics. While laser annealing can be accelerated with increasing laser intensity, this process exhibits a saturation threshold.

To interpret these observations, a phenomenological model is proposed, linking the material bandgap, linear and nonlinear absorption, and wavelength to the total absorbed dose and optical coating lifetime. The model predicts that color change fatigue may arise from linear absorption at low intensities or from nonlinear absorption at higher intensities. These findings underscore the potential of absorption-based diagnostics as a non-destructive approach for predicting the lifetime of optical components under prolonged laser exposure.

5.2 Absorbed dose threshold in dielectric coatings

Motivation

This study follows directly from prior work, with a focus on correlating extended S-on-1 LIDT measurements with absorptance data taken at matched intensities and exposure times, to investigate absorbed dose behavior in the low-intensity regime.

Color change modification is associated with the formation of intermediate states via bond-breaking within the material bandgap, driven by multiphoton absorption processes [10, 63, 87]. Mann et al. observed that absorptance in CaF_2 crystals increases progressively with pulse count until catastrophic damage ensues [160]. Similar behavior has been demonstrated in metals, where higher pulse numbers lead to greater cumulative energy requirements for ablation [167]. Previous studies presented in this dissertation indicated that both single- and multiphoton absorption mechanisms can initiate color change in dielectrics, and suggested that this type of damage lacks a clear LIDT onset. Instead, a fixed absorbed dose threshold may be required for cumulative color change initiation.

Despite advancements in understanding short-term laser-induced damage, the long-term evolution of damage under extended irradiation remains insufficiently characterized. Most existing studies are constrained to relatively low pulse counts, while real-world applications typically involve substantially higher doses and exposure durations [70]. Furthermore, the material scope in many investigations remains limited. Addressing these gaps is critical for advancing the understanding of optical lifetime in relation to material properties and accumulated damage. Accordingly, this work expands the parameter space by exploring HfO_2, Al_2O_3, and ZrO_2 dielectric coatings (RT, 350°C and 500°C, see Table 2.1) and extending the irradiation time range to evaluate the existence of a consistent absorbed dose threshold for color change damage.

Methods

The experiments were performed using two different laser setups. The laser-induced fatigue experiments were performed using a modified S(10^{10})-on-1 LIDT testing, using 355 nm wavelength with 1 MHz repetition rate at 10 ps pulse duration. For each S-on-1 test in the range of $1 - 10^9$ pulses, an array of 50 sites was used, while for 10^{10} pulses, an array of 5 sites was used, with a spacing between sites of at least three beam diameters. After LIDT measurements, all test sites were analyzed using Nomarski microscopy and classified into one of the three groups: no damage, color change damage, and catastrophic damage.

The absorptance was measured using PCI according to the Time-scan protocol with comparable irradiation conditions. This protocol measures absorptance at a stationary sample site over a prolonged exposure duration. Absorptance was recorded at similar intensities and exposure times (defined by the number of pulses and repetition rate) as those used in the LIDT experiments, with the fastest integration time of 50 ms. For exposure times shorter than 50 ms (<10000 pulses), the initial absorptance value was used. In this context, linear absorption is considered a process where absorbed energy is directly proportional to incident light fluence, with absorptance being fluence-independent, while in nonlinear absorption, absorptance is a linear or polynomial function of fluence.

Results

LIDT results

LIDT as a function of the number of pulses for all investigated coatings is represented in Figure 5.12. The data in Fig. 5.12A) demonstrate that color

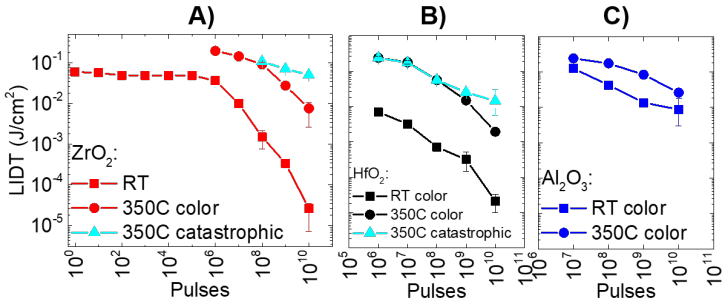

Figure 5.12: LIDT results for A) color change and catastrophic damage on ZrO_2 samples, B) color change and catastrophic damage on HfO_2 samples, and C) color change damage on Al_2O_3 samples. The lines on the graphs are for easier guidance.

change damage was observed throughout the entire pulse count range for the

RT ZrO_2 sample, while for the 350°C ZrO_2 sample, it was noted only from 10^6 pulses onward. For the annealed zirconia, the highest laser intensities were insufficient to induce color changes at lower pulse counts. Similarly, the catastrophic damage was observed only after 10^7 pulses. The intensities were not high enough to induce color change or catastrophic damage at $1 - 10^5$ pulses in HfO_2 (Fig. 5.12B) and at $1 - 10^6$ pulses in Al_2O_3 samples (Fig. 5.12C). A common feature across all investigated coatings is the difference in LIDT between RT and 350°C samples. The RT samples indicate a lower damage threshold, which correlates with the smaller bandgap of RT coatings.

This study included data on catastrophic damage for 350°C ZrO_2 and HfO_2 to highlight the differences between color change and catastrophic damage (catastrophic damage for Al_2O_3 could not be reached). The catastrophic damage of annealed ZrO_2 appears to diverge from the onset of color change. In the case of 350°C HfO_2, both catastrophic and color change LIDTs are very similar (note the log-log scale) for 10^6 to 10^8 laser pulses, thus suggesting that color change precedes long-term catastrophic damage. However, later at 10^9 to 10^{10} pulses, we begin to observe a clear difference, namely the approach of the possible onset of catastrophic LIDT, along with a widening gap between the catastrophic and color change LIDTs. In contrast to catastrophic failure, the color change does not show an indication of the onset of LIDT, consistent with previous findings at shorter irradiation times [14, 16]. These observations raise questions regarding the underlying damage formation mechanisms: it is uncertain whether color changes can also induce catastrophic damage at low fluence levels.

Morphological analysis

Morphological analysis was performed for color change and catastrophic damage for all investigated samples. For simplicity and clarity, typical damage morphologies are shown only for RT and 350°C HfO_2, 350°C ZrO_2, and 350°C Al_2O_3 coatings (Fig. 5.13), as these best exemplify the characteristic damage features observed across all samples. The color change damage in the RT HfO_2 coating (Fig. 5.13A)) follows the beam intensity profile. Time-scan absorptance measurements show a gradual decrease at 0.00047 J/cm^2 fluence and accelerated decline at 0.005 J/cm^2, likely due to laser annealing, which promotes oxidation and improves the coating structure [58]. The color change can be correlated with irradiation time and fluence and linked to changes in refractive index and absorptance, as seen in the difference between RT and thermally annealed samples (Table 2.1).

Although thermally annealed HfO_2 sample shows similar color change (Fig. 5.13B)), the morphology changes are less sensitive to fluence. The increasing absorptance over time suggests a nonlinear absorption-induced bond-breaking. At fluences of 0.088 J/cm^2 and 0.135 J/cm^2, a dark spot appears

in the middle, indicating the formation of catastrophic damage. This suggests distinct mechanisms for the formation of color changes in RT and thermally annealed HfO_2 samples. Both annealing (reducing absorption) and bond-breaking (increasing absorption) can occur simultaneously; however, laser annealing has a negligible effect on thermally annealed samples. For the 350°C ZrO_2 coating, the color change remains localized to the area of highest intensity, with no significant expansion in diameter at higher fluence (Fig. 5.13C). Similar behavior is observed for 350°C Al_2O_3 coating (Fig. 5.13D).

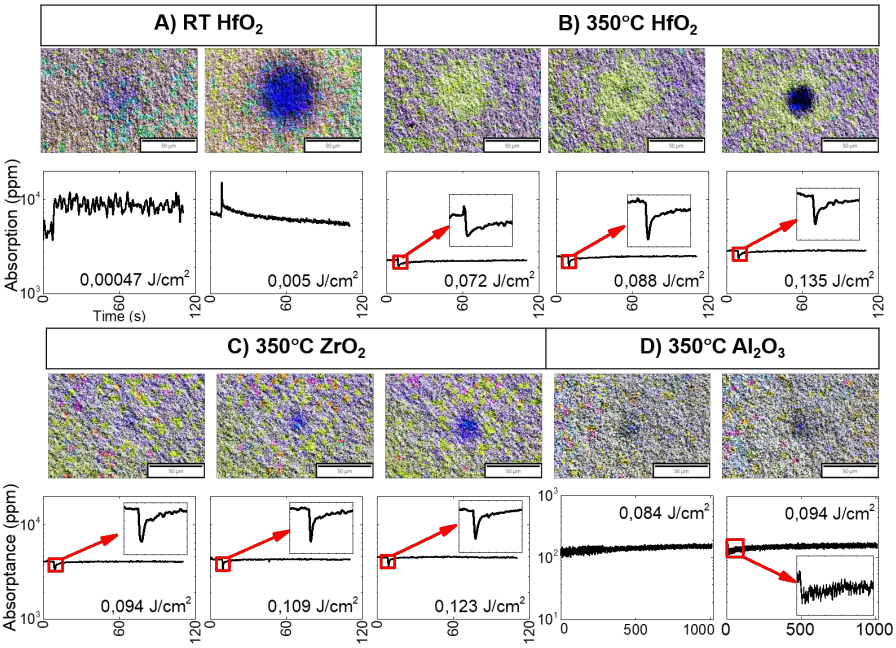

Figure 5.13: High-contrast (obtained from Nomarski differential interference contrast microscope) morphologies with respective temporal absorptance dynamics. The sharp increase or decrease of absorptance indicates the start of the measurement at a fresh site. A) Color change damage for RT HfO_2. B) Evolution of catastrophic damage emerging from color change damage in 350°C HfO_2. C) Color change damage in 350°C ZrO_2. D) Color change damage in 350°C Al_2O_3. The number of pulses for A) – C) is 10^8, while for D) it is 10^9.

Nonlinear absorption

Figure 5.14 summarizes Time-scan absorptance data (average of full Time-scan to ensure full history of irradiation) as a function of intensity. ZrO_2 coatings (Fig. 5.14A) show increasing absorption with intensity, and the RT ZrO_2 exhibits a higher absorptance than the annealed counterpart. Similar trends are observed for HfO_2 and Al_2O_3 coatings (Fig. 5.14B and C).

While both RT ZrO_2 and RT HfO_2 exhibit a high absorptance and a rather

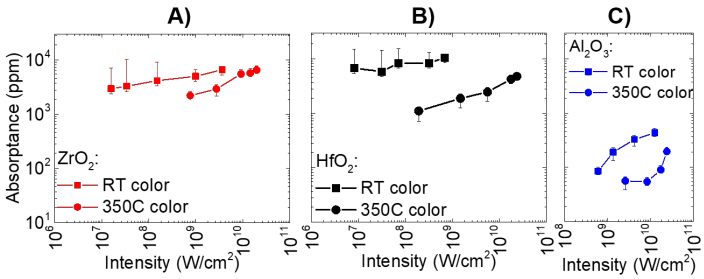

Figure 5.14: Temporal absorptance as a function of LIDT intensity for A) ZrO_2 samples, B) HfO_2 samples, and C) Al_2O_3 samples. Each data point represents the absorptance measured at the damage threshold intensity and irradiation time matching the LIDT measurement. The lines in the graph are for easier guidance.

weak intensity dependence, RT Al_2O_3 shows much smaller absolute absorptance and a clear dominant nonlinear response. This difference can be attributed to the high linear absorption in RT ZrO_2 and RT HfO_2, likely caused by the Urbach tail effect [157], which is observed as a deviation from the linear segment of the absorption spectrum edge towards lower energies (not shown here). In contrast, RT Al_2O_3 exhibits absorptance two orders of magnitude lower.

Absorbed dose estimation

By combining LIDT and absorptance measurements, the absorbed dose required to induce damage is estimated using the following expression [160]:

$$D_{\text{absorbed}}(I_{\text{inc}}) = I_{\text{inc}}\tau \times N \times A(I_{\text{inc}}) \tag{5.10}$$

where I_{inc} is incident LIDT intensity, τ is pulse duration, N is the number of pulses required to reach damage and $A(I_{\text{inc}})$ is the average steady-state absorptance at the LIDT intensity.

Although previous studies identify multiphoton ionization as a primary cause of laser damage [10, 63], findings in this study suggest that high absorbed dose accumulated via one-photon absorption might also be sufficient to cause a subsequent modification. To verify and confirm this assumption, the total absorbed dose required to achieve damage via Eq. 5.10 was calculated and plotted the experimental data as a function of laser intensity in Figure 5.15. for all the investigated materials. In addition, the previously suggested phenomenological model was applied as a fit:

$$D_{\text{absorbed}}(I) = D_0 \left[1 + \left(\frac{I}{I_{\text{crit}}}\right)^{\phi}\right]^{-\gamma}. \tag{5.11}$$

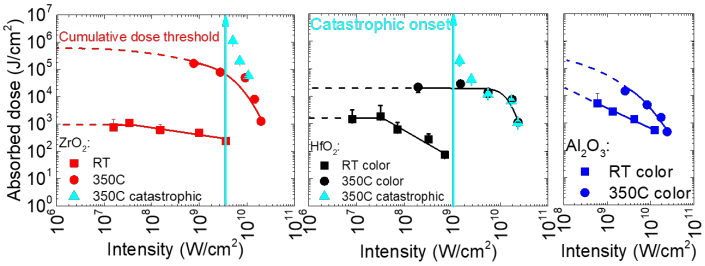

Figure 5.15: Total absorbed dose until damage as a function of LIDT intensity for A) color change and catastrophic damage on ZrO_2 samples, B) color change and catastrophic damage on HfO_2 samples, and C) color change damage on Al_2O_3 samples. The curves represent a phenomenological absorbed dose fit from Eq. 5.11. The arrow indicates catastrophic LIDT intensity onset.

where D_0 is a constant representing the total absorbed dose at low intensity, I_{crit} indicates the critical intensity, where nonlinear absorptance becomes relevant, marking the shift from constant dose to power-law region. D_0, I_{crit}, ϕ, and γ are fitting parameters.

As shown in Figure 5.15, the model effectively describes the absorbed dose for non-catastrophic damage at all materials and intensity levels, even with extended exposure durations. At higher intensities, color change is dominated by nonlinear absorption, which requires a smaller dose. As intensity decreases and number of pulses increases, the absorbed dose for color change becomes independent of intensity, characterized by a constant dose threshold, a feature of dominant linear absorption, regardless of pulse count.

A significant difference in the absorbed dose for the color change is observed between the RT and 350°C ZrO_2 coatings (Fig. 5.15A). The as-deposited coating requires two orders of magnitude less dose at low intensities, likely due to a smaller bandgap or higher dominant linear absorptance [168].

For catastrophic damage (Figs. 5.15A and B), nonlinear absorption dominates the damage formation. However, as intensity decreases, the absorbed dose threshold increases, potentially approaching an infinite dose threshold, which can lead to the onset of LIDT. In contrast, for damage type of color change, the absorbed dose approaches a region independent of intensity as intensity decreases, remaining within the dominant linear absorption regime. This means if irradiation was stopped within constant dose region, catastrophic damage would not occur, as indicate for 350°C HfO_2 in Fig. 5.15. However, there is a possibility of its occurrence with even longer irradiation times. A similar trend for color change is observed for Al_2O_3 coatings (Fig. 5.15C), although no fixed dose threshold was reached within the maximum irradiation time.

Discussion

This study extended previous investigations on the long-term degradation of dielectric optical coatings by examining color change damage and its relation to cumulative absorbed dose under extended irradiation conditions (up to 10^{10} pulses per test site) at a wavelength of 355 nm. The experimental scope included single-layer coatings of hafnia, zirconia, and sapphire.

The analysis distinguishes between two qualitatively different types of color change:

- **Stable, non-catastrophic color changes**, which arise under low-intensity, dominant linear absorption conditions. These were associated with minor reductions in absorptance over time, consistent with local laser annealing and possible completion of oxidation reactions.
- **Transitionary, failure-prone color changes**, which occur under higher-intensity, dominant nonlinear absorption regimes. These involve increasing absorptance over time, consistent with cumulative bond breaking and the formation of lattice-level defects.

Importantly, this study confirms the speculation presented in Section 5.1 that, under linear absorption conditions, the absorbed dose required to initiate color change damage remains approximately constant. In this regime, the total dose scales linearly with the number of pulses and incident intensity, supporting the idea that damage accumulates in a deterministic, energy-limited manner. Conversely, as multiphoton absorption becomes dominant at higher intensities, the absorbed dose threshold drops significantly. This nonlinear behavior indicates that additional defect-generation mechanisms – such as multiphoton absorption and avalanche ionization processes – accelerate degradation by enhancing the rate of lattice modification and sub-bandgap defect formation.

These findings challenge the conventional use of LIDT fatigue thresholds for optical lifetime estimation. In particular, the absence of a clear fatigue onset for color change damage renders traditional lifetime models – based on extrapolation from catastrophic LIDT data – inadequate for describing sub-catastrophic degradation processes.

Morphological analysis confirmed that surface features do not change significantly during the early stages of color change, reinforcing the interpretation that structural modifications occur primarily at the atomic or subsurface level. However, it should be emphasized that no topographical characterization techniques – such as atomic force microscopy, scanning electron microscopy, or surface profilometry – were employed in this study. As such, the physical nature of the color change remains unresolved. It is conceivable that the observed absorptance variations may also result from localized changes in coating thickness or internal structural rearrangements within the irradiated area – effects that cannot be excluded based on absorptance data alone.

Absorbed dose analysis further revealed that catastrophic damage follows a multiphoton absorption-driven process with a distinct fatigue onset, whereas color change damage occurs only after a fixed absorbed dose and shows no LIDT fatigue onset within the tested pulse range. Thermally annealed coatings consistently exhibited higher absorbed dose thresholds, suggesting that materials with larger bandgaps require greater energy input to initiate defect formation, thereby enhancing optical lifetime.

All experiments were conducted using dense ion-beam-sputtered (IBS) coatings, known for their low porosity and high packing density [169]. Coatings fabricated via alternative deposition techniques – such as electron beam evaporation [170] – typically exhibit lower density and different microstructural characteristics, which may significantly affect the onset and progression of laser-induced color change. Future studies should therefore include coatings produced by diverse fabrication methods and incorporate high-resolution topographical and structural diagnostics to develop a more complete understanding of the underlying color change modification mechanisms.

Chapter 5 has demonstrated that non-catastrophic damage mechanisms, such as color change, are both measurable and predictive of long-term optical degradation. By adopting an absorbed dose-based framework and employing time-resolved photothermal diagnostics, these studies shift the emphasis of lifetime assessment away from damage thresholds and toward a continuous-material response. The distinction between benign and failure-prone color change further underscores the need for mechanism-specific models to enable reliable lifetime predictions for optics operating under extended exposure conditions.

Conclusions

Two possible regions of the UV-absorbed dose threshold for color change were identified: one dominated by linear absorption, with a fixed absorbed dose threshold, and the other – nonlinear absorption, where the dose is intensity-dependent. In the nonlinear region, color change precedes catastrophic failure, while in the linear region, color change remains non-catastrophic within investigated absorbed dose levels. Two potential mechanisms for color change formation were identified: bond-creation via laser annealing in as-deposited coatings and bond-breaking via multiphoton ionization in thermally annealed coatings.

Absorbed dose analysis of zirconia and hafnia coatings at low fluence showed that the color change requires a fixed absorbed dose, with no onset of LIDT fatigue within the tested pulse range. Thermally annealed coatings exhibited higher absorbed dose thresholds, suggesting that materials with wider bandgaps require higher doses, thus improving the optical lifetime.

Santrauka

Įvadas

Lazerinės spinduliuotės ir medžiagos sąveika yra fundamentinis fizikinis procesas, apimantis plačią technologinę pažangą. Lazeriai turi itin svarų poveikį: nuo kasdienių pritaikymų, tokių kaip nano-litografija elektronikoje [1] ir tikslaus makro-struktūrų apdirbimo [2], iki milžiniškų iniciatyvų, tokių kaip kosmoso tyrinėjimai [3] ir inertinio izoliavimo termobranduolinė reakcija energijos gamybai [4]. Nepaisant savo universalumo, lazeriais grįstoms technologijoms būdingas bendras iššūkis – optinių komponentų veikimas ekstremaliomis sąlygomis, tokiomis kaip trumpa impulso trukmė, dideli spinduliuotės intensyvumai ir ekstremalūs bangos ilgiai. Tokie režimai neišvengiamai lemia lazerine spinduliuote inicijuojamą optinę pažaidą (LSIOP, angl. laser-induced damage), kuri išlieka pagrindiniu aukštos kokybės lazerinių sistemų vystymą ir patikimumą ribojančiu veiksniu [5].

Fotonikos srityje veikia daugybė lazerių, pasižyminčių įvairiais išėjimo parametrais. Šios sistemos naudoja optinius komponentus pluoštui nukreipti ir perduoti – tiek į lazerio išėjimą, tiek į norimą poziciją erdvėje, priklausomai nuo pritaikymo srities. Tokie komponentai dažnai yra dengti dielektrinėmis arba metalinėmis dangomis, kurios pasižymi skirtingomis optinėmis ir mechaninėmis savybėmis. Todėl jų atsparumas LSIOP stipriai priklauso nuo dangos medžiagos, jos struktūrinio dizaino ir konkrečių lazerio parametrų.

Tarp šių parametrų impulso trukmė [6], pasikartojimo dažnis [7], bangos ilgis [8] ir pluošto skersmuo [9] yra vieni pagrindinių veiksnių, lemiantys LSIOP pradžią ir raidą. Yra itin svarbu suvokti, kaip kiekvienas iš šių parametrų veikia optinį našumą ir kaip šis poveikis gali būti patikimai prognozuojamas. Lazerio parametrų įvairovė paskatino mastelio dėsnių (angl. scaling laws) kūrimą, siekiant modeliuoti ir įvertinti pažaidos lazerio spinduliuotei slenkstį (PLSS, angl. laser-induced damage threshold) esant skirtingoms apšvitos sąlygoms. Nors daugelis tyrimų nagrinėjo PLSS priklausomybę nuo atskirų lazerio parametrų, dažnai juos riboja siaura eksperimentinė imtis arba prieštaringi rezultatai.

Ypač svarbu pažymėti, kad dauguma PLSS mastelio dėsnių tyrimų buvo orientuoti į vieno ar kelių šimtų impulsų pažaidą, nors praktikoje optiniai komponentai dažniausiai yra veikiami ilgalaikės (daugiaimpulsės) lazerinės spinduliuotės. Tokiomis sąlygomis medžiagos gali nespėti visiškai atsigauti tarp impulsų, todėl pažaida kaupiasi. Šis reiškinys, žinomas kaip nuovargio efektas (angl. fatigue effect) [10], gali reikšmingai paveikti ilgalaikį optinių elementų našumą ir ilgaamžiškumą. Šiuo metu ilgaamžiškumo vertinimo metodai remi-

asi arba trumpalaikių daugiaimpulsinių PLSS rezultatų ekstrapoliavimu [11], kuris gali būti nepatikimas, arba ilgalaikiais bandymais, kurie yra itin imlūs laikui ir kaštams.

Nors pažanga PLSS mastelio dėsnių tyrimuose yra svari, iki šiol išlieka esminių spragų – ypač suvokiant, kaip kombinuoti lazerio parametrai ir ilgalaikė apšvita veikia optinių medžiagų elgseną bei kokios medžiagų savybės lemia šiuos atsakus. Dabartiniai modeliai dažnai remiasi supaprastintomis sąlygomis arba ribotais duomenų rinkiniais ir gali netiksliai atspindėti kaupiamąją pažaidos degradaciją, stebimą realiose lazerinėse sistemose. Tai pabrėžia poreikį sukurti išsamesnį ir prognozuojamą modelį, apjungiantį tiek pažaidos slenkstį, tiek optinį ilgaamžiškumą.

Disertacijos tikslas

Pagrindinis šios disertacijos tikslas – išnagrinėti pažaidos lazerine spinduliuote slenksčio mastelio dėsnius bei lazerinio nuovargio efektą, siekiant prognozuoti ir charakterizuoti optinių dangų ilgaamžiškumą.

Pagrindiniai disertacijos uždaviniai

Disertacijos tikslui pasiekti buvo iškelti šie uždaviniai:

- Išskirti bei išanalizuoti PLSS mastelio dėsnius impulso trukmės atžvilgiu skirtingoms pažaidos modoms plonose dielektrinėse dangose, pasitelkiant ultravioletinę ir infraraudonąją spinduliuotę.
- Atlikti kokybinius ir kiekybinius plonųjų metalinių dangų PLSS priklausomybės nuo impulso trukmės tyrimus; kritiškai įvertinti esamus nuspėjamuosius modelius bei juos patikslinti, remiantis teorine analize bei empiriniais tyrimais.
- Atlikti eksperimentinį tyrimą apie laikinį sugerties elgesį dielektrinėse dangose UV – IR bangos ilgių imtyje.
- Išplėtoti universalų optinio ilgaamžiškumo prognozavimo modelį dielektrinėms dangoms, veikiančioms ultratrumpųjų impulsų apšvitos sąlygomis.

Mokslinis naujumas ir praktinis pritaikymas

Nors katastrofinio PLSS mastelio dėsniai ir nuovargio elgsena buvo išsamiai tiriami, spalvinio pokyčio pažaidos įtaka katastrofinei pažaidai vis dar nėra

pakankamai suprasta. Be to, esami optinio ilgaamžiškumo prognozavimo modeliai daugiausia remiasi katastrofinės pažaidos nuovargio sotimi (angl. fatigue onset), nepaisant galimos spalvinio pokyčio pažaidos vaidmens ilgalaikėje optinėje degradacijoje.

- Pirmą kartą buvo tiriamas spalvinio pokyčio PLSS dielektrinėse dangose kaip impulso trukmės (τ) funkcija. Teorinė analizė, paremta laisvųjų elektronų generavimo lygtimis, rodo, kad laipsninio dėsnio (angl. power-law) laipsnio rodiklis priklauso nuo medžiagos draustinės juostos pločio ir lazerio bangos ilgio.

- Daugiaimpulsinio PLSS daugiasluoksnėse skaidrinančiose dangose analizė atskleidė, kad katastrofinės pažaidos nuovargis priklauso nuo impulso trukmės tiek IR, tiek UV bangos ilgiuose, o spalvinio pokyčio nuovargio elgsena, atrodo, beveik nekinta nuo impulso trukmės.

- Išsamus PLSS mastelio dėsnių tyrimas impulso trukmės atžvilgiu metalinėse ir puslaidininkių dangose parodė sudėtingą priklausomybę nuo dangos storio ir specifinės šiluminės talpos, kurią lemia medžiagos šiluminė vėsimo konstanta.

- Spalvinio pokyčio pažaidos morfologijų ir laikinės sugerties dinamikos analizė dielektrinėse dangose atskleidė skirtingą sugertos energijos dalies elgseną, priklausomai nuo to, ar medžiaga buvo termiškai atkaitinta, suteikdama gilias įžvalgas apie spalvinio pokyčio pažaidos formavimąsi ir ilgalaikę medžiagos elgseną.

- Dielektrinėse dangose buvo ištirta laikinė sugerties dinamikos priklausomybė nuo impulso trukmės. Sugertos dalies duomenų analizė, pasitelkiant elektronų generavimo lygtis, parodė, jog klasikinis daugiafotonės sugerties reiškinys savaime negali paaiškinti eksperimento tendencijų. Skaitinė analizė parodė, jog tarpinės pašalinės būsenos, esančios draustinėje juostoje, gali smarkiai paveikti medžiagos netiesines optines savybes, kurios priklauso ne tik nuo impulso trukmės, tačiau ir medžiagos savybių.

- Kartu pritaikius PLSS ir sugerties matavimo metodus, buvo galima analizuoti ryšį tarp sugertos energijos dalies ir lazerine spinduliuote inicijuojamo spalvinio pokyčio nuovargio, gilaus UV (angl. deep-UV) – IR bangos ilgių diapazone, esant fiksuotai impulso trukmei.

- Sugertos dozės analizė dielektrinėse dangose leido išvystyti fenomenologinį optinio ilgaamžiškumo prognozavimo modelį.

Ginamieji teiginiai

1. Pažaidos lazerine spinduliuote slenksčio mastelio dėsniai impulso trukmės atžvilgiu optinėse dangose nepaklūsta populiariam $\tau^{0.5}$ dėsniui, tačiau priklauso nuo pažaidos modos, krintančio bangos ilgio, impulsų skaičiaus ir medžiagos savybių.

2. Pažaidos lazerine spinduliuote slenkstis metalinėse dangose impulsiniame režime labiausiai yra lemiamas dangos specifinės šiluminės talpos, o nuolatinės veikos režime – pagrinduko šiluminės difuzijos.

3. Lazerinės spinduliuotės inicijuoti spalviniai pokyčiai dielektrinės dangose gali būti sukeliami tiek dėl tiesinės, tiek dėl netiesinės sugerties, su sąlyga, kad pasiekiamas sugertos dozės slenkstis.

4. Bendras sugertos dozės slenkstis, lemiantis optinį ilgaamžiškumą dielektrinėse dangose spalvinių pokyčių atžvilgiu smarkiai priklauso nuo medžiagos savybių ir fotono energijos, kurie kartu lemia sugerties eilę.

5. Lazerine spinduliuote inicijuoto spalvinio pokyčio pažaida dielektrinėse dangose gal kilti dėl bent dviejų fizikinių reiškinių: lazerinio atkaitinimo arba cheminių ryšių nutraukimo.

Autorių indėlis

Šios disertacijos autorius prisidėjo prie eksperimentų planavimo, atliko didžiąją dalį PLSS ir visus sugerties matavimo eksperimentus, išanalizavo visus eksperimentinius rezultatus ir parengė publikacijų rankraščius [**A1** – **A5**]. Autorius atliko skaitinę elektronų generacijos greičio lygčių ir morfologinę analizę publikacijoje [**A1**], sukūrė skaitinę sugerties ir optinio ilgaamžiškumo vertinimo analizę publikacijose [**A3, A5**], ir atliko skaitinę analizę publikacijose [**A2, A5**].

- Doc. dr. Andrius Melninkaitis dalyvavo visuose šioje disertacijoje aprašytuose tyrimuose. Jis suformulavo pagrindinius uždavinius ir tikslus, pateikė analitines įžvalgas apie gautus rezultatus, peržiūrėjo parengtus rankraščius, konsultavo eksperimentų planavimo, jų atlikimo, skaitinio modeliavimo klausimais bei bendrai lazerine spinduliuote inicijuojamos optinės pažaidos ir sugerties fizikos srityje.

- Dr. Linas Smalakys teikė patarimus ir technines įžvalgas apie spalvinio pokyčio pažaidos morfologinį vertinimą publikacijoje [**A1**].

- Martynas Keršys padėjo rašyti skaitinio modeliavimo kodą publikacijoje [**A2**].

- Dr. Simonas Kičas ir Vaida Grašytė pateikė eksperimentinius bandinius ir spektrinius matavimus publikacijose [**A3, A5**] ir antrame skyriuje aptartiems tyrimams.
- Austėja Aleksiejūtė padėjo atlikti PLSS matavimus publikacijoje [**A3**].
- Dr. Justinas Galinis padėjo atlikti pažaidos vietų analizę publikacijoje [**A3**], padėjo su morfologijų atvaizdavimu publikacijoje [**A5**].
- Dr. Marco Jupé, dr. Kevin Kiedrowski, dr. Morten Steinecke, Lars Herrero ir dr. Lars Jensen pateikė eksperimentinius bandinius ir technines įžvalgas apie jų paruošimą publikacijoje [**A4**].
- Urtė Kimbaraitė ir Mindaugas Ščiuka padėjo atlikti PLSS matavimus su nuolatinės veikos lazeriu publikacijoje [**A4**].
- Emilija Žutautaitė padėjo atlikti šilumos sklaidos modelio skaitinę simuliaciją publikacijoje [**A4**].
- Prof. dr. Laurent Gallais pateikė dviejų temperatūrų modelio skaitines simuliacijas publikacijoje [**A4**].
- dr. Arūnas Varanavičius ir Gaudenis Jansonas suteikė pagalbą ir ekspertines žinias, atliekant PLSS eksperimentus su trumpesniais nei 10 fs trukmės impulsais NAGLIS OPCPA sistemoje publikacijoje [**A4**].
- dr. Vytautas Jukna pateikė skaitinių simuliacijų kodą ir išvalgas apie sugerties procesus, pateiktus antrame skyriuje.

Santraukos struktūra

Ši disertacija yra parengta straipsnių pagrindu, aptariant publikacijas [**A1**] – [**A5**] ir nepaskelbtus duomenis.

Ši santrauka padalinta į tris skyrius. Pirmajame skyriuje glaustai aptariami PLSS mastelio dėsniai impulso trukmės atžvilgiu metalinėse ir dielektrinėse dangose. Antrame skyriuje glaustai aptariami sugerties procesai dielektrinėse dangose. Trečiame skyriuje aptariama sugerties įtaka nuovargio efektui ir kaip sugerties procesai lemia optinių dangų ilgaamžiškumą.

Pažaidos lazerine spinduliuote slenksčio mastelio dėsniai pagal impulso trukmę

Šio skyriaus turinys pagrįstas publikacijomis [**A1**] ir [**A4**], kurios buvo pristatytos konferencijose [**C1**], [**C3**], [**C4**], [**C5**], [**C8**] ir [**C12**].

PLSS mastelio dėsniai pagal impulso trukmę metalinėse dangose

Nors metalinės dangos pasižymi tokiais privalumais, kaip dispersijos neturintis atspindys ir platus spektrinis diapazonas, jų PLSS elgsena – ypač plačiame impulso trukmių intervale – išlieka menkai suprasta. Dauguma esamų metalų PLSS tyrimų apsiriboja siaurais trukmės intervalais arba neatsižvelgia į daugkartinės spinduliuotės sukeltą nuovargį. Šis darbas siekia užpildyti šią spragą, tiriant PLSS mastelio dėsnius plačiame impulso trukmių intervale (10 fs – 10 s), nustatant, ar metalams taikomi universalūs mastelio dėsniai, bei identifikuojant pagrindinius fizikinius parametrus.

Eksperimentinis tyrimas buvo atliktas su septyniomis metalinėmis (Al, Au, Ag, Cr, Ti, W, Ta) ir dviejomis puslaidininkinėmis (Si, Ge) dangomis, nusodintoms ant Borofloat stiklo pagrindukų, naudojant nuolatinio arba kintamo dažnio magnetroninio garinimo technologiją. Dangų storis svyravo nuo 45 nm iki 1775 nm. PLSS matavimai buvo atlikti pagal ISO standartą taikant 1-į-1 ir S(1000)-į-1 protokolus IR bangos ilgių ruože (1030 nm, 1064 nm ir 1070 nm). Buvo naudojamos trys lazerinės sistemos, o eksperimentinės sąlygos buvo kruopščiai prižiūrimos, užtikrinant duomenų patikimumą ir palyginimą tarp skirtingų sistemų. Daugumai impulsų trukmių pluošto skersmuo $1/e^2$ lygmenyje siekė 195 – 230 µm, o trumpiausiems impulsams (10 fs) – apie 100 µm. Nepaisant šio skirtumo, PLSS reikšmės ties 10 fs išliko nuoseklios, patvirtinant rezultatų patikimumą.

Pagrindinis šio darbo rezultatas – aiškus dviejų skirtingų PLSS mastelio dėsnių režimų identifikavimas. Impulsiniame režime (10 fs – 9 ns) buvo pastebėtas silpnas laipsninis dėsnis tarp PLSS ir impulso trukmės, su eksperimentiniais laipsnio rodikliais nuo 0.01 iki 0.15 vieno impulso (1-į-1) režimu ir nuo 0.05 iki 0.23 daugiaimpulsio (S-į-1) testavimo režimu. Šie rezultatai patvirtina, kad itin trumpų impulsų atveju pažaida daugiausia priklauso nuo metalo dangos šiluminės talpos, o šilumos difuzijos kaupimasis turi mažą reikšmę. Iš kitos pusės, nuolatinės veikos (NV) režime (100 ms – 10 s) stebėtas beveik tiesinis PLSS mastelio dėsnis ($\tau^{0.77-1.00}$), rodantis, kad vyrauja pagrinduko šiluminės difuzijos procesai.

Vienas iš reikšmingiausių pasiekimų – tai, kad perėjimas tarp impulsinio ir NV režimų priklauso nuo šiluminio vėsimo konstantos, kuri priklauso nuo specifinės šiluminės talpos ir dangos storio. Remiantis polinominės regresijos modeliavimu ir dviejų temperatūrų modeliu (DTM), šis ryšys buvo kiekybiškai įvertintas. Nustatyta, kad didesnę šiluminę talpą turinčios dangos arba dangos ant didesnės šiluminės difuzijos pagrindukų (pvz., vario) pasižymi lėtesniu perėjimu į NV režimą ir dėl to yra atsparesnės šilumos kaupimuisi. Taip pat eksperimentiškai buvo patvirtintas atvirkštinis ryšys tarp sugertos energijos dalies ir PLSS – didesnė sugerta dalis dažniausiai lėmė mažesnį PLSS. Vis dėlto,

impulsiniame režime pastebėtos išimtys, ypač aukštos lydymosi temperatūros dangoms, tokioms kaip volframas, kurios parodė, kad lydymosi temperatūra ir šiluminė talpa taip pat turi reikšmingą poveikį PLSS. Tai pabrėžia sudėtingą metalų PLSS elgseną, kur įvairūs fizikiniai parametrai – šiluminiai, mechaniniai ir optiniai – veikia, priklausomai nuo impulso trukmės.

Kitas svarbus rezultatas – eksperimentinis įrodymas, kad daugkartinės spinduliuotės sukeltas nuovargis padidina metalinių dangų jautrumą impulso trukmei, tikėtina, dėl kaupiamojo šiluminio ir mechaninio streso. Tokios degradacijos mechanizmai apima paviršiaus šiurkštėjimą, oksidaciją ir negrįžtamus mikro-struktūrinius pokyčius, kurie lemia ankstyvesnį pažaidos atsiradimą.

DTM buvo esminis faktorius, aiškinant eksperimentinius rezultatus, ypač tais atvejais, kai klasikiniai šilumos sklaidos modeliai, tokie kaip Wood'o vienmatė teorija, nesugebėjo pateikti tinkamo paaiškinimo. Nors Wood'o modelis tiksliai apibūdina tiesinį mastelio dėsnį NV režime, jis remiasi pusiau begalinio pagrinduko prielaida ir todėl netinka plonosioms dangoms ar netolygiai pasiskirsčiusioms energijoms trumpųjų impulsų metu. DTM, atsižvelgdamas į elektronų ir gardelės nesusietą šilumos pernašą bei energijos dinamiką, geriau atitinka stebėtus duomenis.

Išvados

Rezultatai parodė silpną laipsninio dėsnio priklausomybę tarp PLSS ir impulso trukmės impulsiniame režime ($\tau^{0.01–0.23}$), o beveik tiesinė priklausomybė ($\tau^{0.77–1.00}$) stebėta NV režime. Perėjimą tarp šių režimų lemia šiluminė vėsimo konstanta, kuri priklauso nuo dangos savitosios šiluminės talpos ir storio. Tiek eksperimentiniai duomenys, tiek skaitinis modeliavimas patvirtino, kad pagrinduko šiluminė difuzija ir pluošto skersmuo taip pat turi įtakos PLSS priklausomybei.

Be to, nustatyta, kad PLSS yra atvirkščiai proporcingas medžiagos sugerties koeficientui, tačiau nukrypimai impulsiniame režime rodo papildomą šiluminės talpos ir lydymosi temperatūros įtaką. Daugelio impulsų poveikis sukėlė matomus nuovargio reiškinius, kurie sustiprino PLSS nuo impulso trukmės priklausomybę impulsiniame režime.

Dviejų temperatūrų modelis pateikė tikslesnes prognozes nei klasikiniai šilumos sklaidos modeliai, ypač sub-ns intervalo trukmėms, ir parodė, kad NV sąlygoms būtinas detalesnis modeliavimas. Vis dėlto, tyrimas buvo apribotas fiksuotais bangos ilgiais ir pluošto dydžiais, todėl jo taikomumas kitoms spektrinėms ar geometrinėms sritims gali būti ribotas.

PLSS mastelio dėsniai pagal impulso trukmę dielektrinės dangose

Nors daug pastangų skirta katastrofinės pažaidos modeliavimui vieno are kelių impulsų sąlygomis, praktikoje lazerinės sistemos veikia daugkartinio apšvitos režimu, kuriame atsiranda kaupiamieji efektai. Sub-katastrofinė pažaida, tokia kaip spalviniai pokyčiai, dažnai yra ignoruojama mastelio tyrimuose, nors ji gali būti ankstyvas optinės degradacijos indikatorius. Šis tyrimas siekia sistemingai ištirti tiek katastrofinius, tiek spalvinio pokyčio pažaidos režimus skaidrinančiose (AR) dangose, remiantis eksperimentiniais PLSS matavimais ir teoriniu modeliavimu. Tyime buvo analizuotos dvi daugiasluoksnės dangos: skirta 1064 nm + 532 nm, sudaryta iš aukšto lūžio rodiklio ZrO_2 ir žemo lūžio rodiklio SiO_2 sluoksnių, ir skirta 355 nm bangos ilgiui, sudaryta iš Al_2O_3 ir SiO_2 sluoksnių.

PLSS matavimai buvo atliekami taikant 1-į-1 ir S-į-1 protokolus su impulsų skaičiumi nuo 1 iki 10^5, plačiame impulso trukmių intervale (50 fs – 9 ns). Pažaidos morfologija buvo vertinama naudojant diferencialinio interferencinio kontrasto (DIK) mikroskopiją, o pažaidos pobūdis buvo klasifikuojamas kaip katastrofinis arba spalvinis pokytis. Teorinei interpretacijai naudoti vienos elektronų generacijos lygties ir uždelstos elektronų generacijos lygčių modeliai, siekiant nustatyti, kurie pažaidos mechanizmai – daugiafotonė jonizacija (DFJ), griūtinė jonizacija (GJ) ar krūvininkų rekombinacija (RE) – dominuoja skirtinguose režimuose.

Eksperimentiniai rezultatai parodė, kad PLSS mastelio dėsnis aiškiai priklauso nuo pažaidos režimo. Katastrofinės pažaidos atveju buvo stebimas nuoseklus impulso trukmės dėsningumas – PLSS priklausė pagal $\tau^{0.35-0.40}$ tiek IR, tiek UV bangos ilgiuose. Šis laipsnio rodiklis nurodo DFJ inicijuotą, ir toliau sekantį GJ pažaidos mechanizmą – šią išvadą patvirtino ir teorinis modelis, kuriam prireikė visų DFJ + GJ + RE dėmenų, siekiant aproksimuoti duomenis.

Spalvinio pokyčio pažaida pasižymėjo visiškai kitokiu elgesiu. Morfologinė analizė parodė, kad spalviniai pokyčiai atsirado tik itin trumpų impulsų (<10 ps) metu ir visiškai nepasireiškė ilgesnių trukmių atveju – tai rodo, jog dominuoja DFJ mechanizmas be pakankamos plazmos tankio griūtinei jonizacijai. Šiuo atveju, iš S-į-1 matavimų gauti laipsninio dėsnio laipsnio rodikliai buvo $\tau^{0.55-0.65}$ (IR) ir $\tau^{0.43-0.52}$ (UV). Teorinis modelis parodė, kad šie laipsnio rodikliai atitinka dviejų–trijų fotonų sugerties procesus. Tai, kad abu pažaidos režimai buvo modeliuojami naudojant tuos pačius medžiagos parametrus, keičiant tik elektronų tankio slenkstį (10^{18}cm^{-3} spalviniam pokyčiui ir 10^{21}cm^{-3} katastrofinei pažaida), stipriai pagrindžia hipotezę, jog pažaidos tipą lemia sugertos energijos ir elektronų tankio dydis.

Vienas svarbiausių šio skyriaus rezultatų yra tai, kad katastrofinės pažaidos nuovargis smarkiai priklauso nuo impulso trukmės, rodantis, kad pakartotinė

sub-slenkstinė apšvita sukelia laipsnišką medžiagos degradaciją. O spalvos pokyčio nuovargis parodė menką priklausomybę nuo trukmės, tai leidžia manyti apie sužadinimo sotį be griūtinės jonizacijos plėtros arba apie savaime ribojamą defektų formavimąsi. Be to, tyrimas parodė, kad daugiaimpulsis poveikis sustiprina PLSS priklausomybę nuo impulso trukmės katastrofinės pažaidos atveju. Šis pastebėjimas dar smarkiau pagrindžia tai, jog nuovargio efektai modifikuoja medžiagos atsaką per struktūrinius ar cheminius pokyčius. Taip pat pabrėžtas fotonų energijos ir medžiagos draustinės juostos reikšmingumas: mažesnio draustinės juostos pločio medžiagos (pvz., ZrO_2) buvo jautresnės daugiafotinei sužadinimo sąlygai IR intervale, kaip ir tikėtasi pagal teorinius modelius.

Išvados

Pirmą kartą lazeriu sukeltų spalvinių pokyčių analizė LBO kristalų skaidrinančiose dangose IR ir UV diapazonuose buvo susieta su PLSS mastelio dėsningumais pagal impulso trukmę. Tiesioginis eksperimentinių PLSS duomenų ir elektronų generavimo lygčių modelių palyginimas parodė, kad PLSS mastelio dėsnis nėra universalus, bet priklauso nuo pažaidos režimo. Daugiafotonė sugertis dominuoja pradinėje pažaidos stadijoje esant trumpoms impulso trukmėms ir taip pat lemia spalvinių pokyčių atsiradimą ilgalaikio daugiaimpulsio eksponavimo metu. Atitinkamai, netiesinės sugerties sukelti spalviniai pokyčiai aiškiai priklauso nuo medžiagos draustinio juostos tarpo ir lazerio bangos ilgio.

Eksperimentu nustatyti PLSS mastelio dėsnio laipsnio rodikliai, taikant nuo 1 iki 10^5 impulsų taškui, spalviniams pokyčiams buvo $\tau^{0.55-0.65}$ IR diapazone ir $\tau^{0.43-0.52}$ UV diapazone. Vienos elektronų generavimo lygties modeliavimas sieja $\tau^{0.5}$ laipsnio rodiklį su dviejų fotonų sugertimi, o didesni laipsnio rodikliai rodo aukštesnės eilės daugiafotonės sugerties dalyvavimą. Abu pažaidos režimai buvo nuspėti naudojant tuos pačius medžiagos parametrus, tačiau taikant skirtingus slenksčius – sub-kritinę laisvųjų elektronų koncentraciją spalviniams pokyčiams ir kritinę elektronų koncentraciją katastrofiniam pažeidimui.

PLSS mastelio dėsnis katastrofiniam pažeidimui buvo nuoseklus tiek IR, tiek UV bangos ilgiams – nustatyti laipsnio rodikliai $\tau^{0.35-0.4}$ 50 fs – 9 ns intervalo impulso trukmėms, taikant tiek 1-į-1, tiek 10^5-į-1 matavimo protokolus. Laipsnio rodiklis, mažesnis nei 0.5, rodo dominuojantį griūtinės jonizacijos vaidmenį formuojantis katastrofiniam pažeidimui.

Nuovargio analizė parodė, kad katastrofinės pažaidos nuovargis aiškiai priklauso nuo impulso trukmės abiejuose bangos ilgiuose, o spalvinių pokyčių nuovargis praktiškai nerodė jokios priklausomybės. Toks nejautrumas atitinka netiesine sugertimi pagrįstą pažaidos formavimosi mechanizmą, nes spalvos pokyčiai nebuvo stebėti esant ilgesnei nei 10 ps impulso trukmei. Priešingai, katastrofinės pažaidos nuovargio priklausomybė nuo impulso trukmės gali

atspindėti papildomą griūtinės jonizacijos įtaką, ypač ilgėjant impulso trukmei.

Netiesinės sugerties įtaka PLSS

Šio skyriaus turinys pagrįstas straipsniu [**A2**] ir nepaskelbtais duomenimis, kurie buvo pristatyti konferencijose [**C6**], [**C7**] ir [**C12**].

Netiesinės sugerties elgesys dielektrinėse dangose

Kadangi ultratrumpųjų impulsų lazerinės sistemos tampa vis plačiau naudojamos pramoninėse ir mokslinėse srityse, tampa vis svarbiau suprasti optinių komponentų tarnavimo laiką ribojančius mechanizmus. Šiame skyriuje ypatingas dėmesys skiriamas tam, kaip netiesinė sugertis prisideda prie lazerine spinduliuote inicijuojamos optinės pažaidos vienasluoksnėse dangose.

Šiems efektams tirti buvo pasirinktos vienasluoksnės hafnio dioksido (HfO_2) dangos, nusodintos jonų pluošto garinimo būdu – dėl jų plataus taikymo didelės galios optikoje ir gerai apibrėžtų medžiaginių savybių. Buvo nagrinėtos trijų apdorojimų dangos: termiškai neapdorota po nusodinimo (kambario temperatūros), ir termiškai atkaitintos, esant 350°C ir 500°C temperatūroms 1 valandą. Netiesinės sugerties matavimai buvo atlikti taikant fototerminę bendro kelio interferometriją skirtingais bangos ilgiais (1064 nm, 532 nm ir 355 nm), naudojant 10 ps, 1 MHz lazerio šaltinį. Šis metodas leido atlikti laikinę sugerties kitimo analizę ir nustatyti jos ryšį su medžiagos pokyčiais. Sugertis buvo vertinama dviejais protokolais: T-scan (sugertis matuojama skirtinguose erdvės taškuose vienoje linijoje) ir Time-scan (sugertis stebima viename taške laike, esant pastoviam intensyvumui). Šie matavimo protokolai leido ištirti tiek momentinį, tiek laikinį medžiagos sugerties atsaką.

Išmatavus sugertį, buvo identifikuoti skirtingi daugiafotonės sugerties režimai, priklausomai nuo naudoto bangos ilgio. Esant 355 nm bangos ilgiui, sugertis pasižymėjo beveik linijine priklausomybe nuo intensyvumo, atitinkančia dviejų fotonų sugertį. 532 nm bangos ilgiu buvo stebimas mišrus režimas, kuriame vyko tiek dvifotonė, tiek trifotonė sugertis. Šie rezultatai buvo patvirtinti polinominio dėsnio ir empirinio modeliavimo būdu – nustatytos laipsninio dėsnio priklausomybės, atitinkančios teorines daugiafotonės sugerties prognozes, pagrįstas sveiko skaičiaus santykiu tarp medžiagos draustinio juostos tarpo ir fotono energijų.

Time-scan matavimai (10 min. eksponavimas) atskleidė skirtingas sugerties dinamikos tendencijas, priklausomai nuo dangos šiluminio apdorojimo būklės. Kambario temperatūros bandinyje sugerta dalis laikui bėgant mažėjo su visais bangos ilgiais – tai siejama su lazeriniu atkaitinimu, kuris pagerina dangos kokybę ir sumažina su defektais susijusią sugertį. Priešingai, termiškai atkaitintose dangose sugerta dalis su laiku didėjo, o tai rodo kaupiamąjį cheminių

ryšių ardymą ir spalvinių centrų formavimąsi. Tiek mažėjanti, tiek didėjanti sugerties dinamika, esant vienodoms eksponavimo sąlygoms, parodo sudėtingą sąveiką tarp atkaitinimo ir defektų kaupimo dangoje.

Rezultatai rodo, kad nors šiluminis atkaitinimas sumažina tiesinę sugertį dėl užbaigiamo oksidacijos proceso, jis taip pat padidina dangos jautrumą daugiafotoninei jonizacijai, esant didelio intensyvumo apšvitai. Be to, esant mažesniam intensyvumui, vyrauja atkaitinimo efektai, dėl kurių sugerta dalis mažėja, tačiau padidėjus intensyvumui, netiesiniai procesai ima dominuoti ir sugerta dalis pradeda augti. Šie priešingi mechanizmai parodo, kad norint išsamiai suprasti netiesinę sugertį, būtini laikinės skyros (angl. time-resolved) matavimai.

Išvados

Netiesinės sugerties matavimai, atlikti 1064 nm – 355 nm bangos ilgių intervale, atskleidė skirtingą intensyvumo priklausomybę. Silpniausia netiesinė sąveika, proporcinga I^1 priklausomybei (rodanti dviejų fotonų sugertį), buvo nustatyta esant 355 nm bangos ilgiui. O 532 nm bangos ilgiui būdinga mišri priklausomybė tarp I^1 ir I^2, parodant, kad vyksta tiek dviejų, tiek trijų fotonų sugertis.

Laikinė sugerties analizė (Time-scan) parodė, kad lazerinio eksponavimo metu veikia du konkuruojantys mechanizmai: lazeriu sukeltas atkaitinimas, kuris mažina bendrąją sugertį (tikėtina, dėl paviršinių defektų sumažėjimo draustinėje juostoje), ir cheminių ryšių ardymas, po kurio galimai susidaro spalviniai centrai, didinantys sugertį.

Šie rezultatai išryškina šiluminių ir elektroninių procesų sąveiką, lemiančią dinaminius hafnio dangų sugerties pokyčius, veikiant didelio intensyvumo spinduliuotei 1064 – 355 nm bangos ilgių intervale.

Netiesinės sugerties priklausomybė nuo impulso trukmės

Šiame tyrime pateikiama išsami eksperimentinė ir skaitinė dielektrinių plonų dangų laikinės sugerties dinamikos analizė priklausomai nuo lazerio impulso trukmės, apimančios intervalą nuo 170 fs iki 10 ps UV srityje (343 nm ir 355 nm). Tirtos dangos apima vienasluoksnes HfO_2, SiO_2 ir dvisluoksnę skaidrinančią (AR) HfO_2/SiO_2 dangas. Sugertis buvo matuota naudojant fototerminę bendro kelio interferometriją (PCI).

Tyrimo motyvacija kilo iš žinomo klasikinio elektronų generavimo lygčių modelių apribojimo: nors šie modeliai sėkmingai prognozuoja PLSS mastelio dėsnius pagal impulso trukmę, jie neatsižvelgia į medžiagos savybių pokyčius ilgalaikio ar daugiaimpulsio spinduliavimo metu – sąlygas, aktualias realiam lazeriniam taikymui. Standartiniai modeliai paprastai remiasi pastoviomis medžiagų savybėmis ir nuo intensyvumo priklausančia sugertimi, tačiau ig-

noruoja tai, kad sugertis laikui bėgant gali kisti dėl defektų susidarymo ar atkaitinimo.

Šiame tyrime buvo pritaikytos dvi sugerties matavimo protokolo versijos (T-scan ir Time-scan), kurios leido nustatyti tris skirtingas sugertos dalies sritis visoms dangoms: (1) pradinį sugertos dalies sumažėjimą, esant mažam energijos įtėkiui (galimai susijęs su lazeriniu atkaitinimu), (2) tiesinės sugerties sritį ir (3) netiesinės sugerties sritį su didesniais energijos įtėkiais dėl daugiafotonės sugerties (DFS). Pastebėta aiški sugertos dalies priklausomybė nuo impulso trukmės, kuri prieštarauja modeliams su fiksuotais optiniais medžiagos parametrais.

Pradinis modeliavimas, pagrįstas standartinėmis elektronų generavimo lygtimis – įtraukiant tiesinę sugertį, DFS ir laisvųjų krūvininkų sugertį – bei statinėmis medžiagos savybėmis, nesugebėjo atkurti pagrindinių eksperimentinių tendencijų, ypač sugertos dalies priklausomybės nuo energijos įtėkio statumo ir sugerties duomenų sangrūdą pagal impulso trukmę. Papildoma analizė parodė, kad DFS dominuoja, esant didesniam energijos įtėkiui, o esant mažesniam energijos įtėkiui, matoma palyginimo dydžio tiek tiesinė sugertis, tiek DFS. Laisvųjų krūvininkų sugerties įtaka buvo nereikšminga.

Siekiant išspręsti šiuos neatitikimus, buvo pritaikytas išplėstas elektronų generavimo lygčių modelis, įtraukiantis defektų sukeliamą vienfotonę sugertį iš seklių defektinių būsenų draustinėje juostoje. Šis modifikuotas modelis leido įvertinti vienfotonį sužadinimą iš defektinių lygmenų ir įtraukė defektų būsenų išsekimo dėmenį, kuris buvo esminis sekiant paaiškinti laikinės sugerties statumą. Keičiant tiesinės ir netiesinės sugerties koeficientus, priklausomai nuo impulso trukmės, išplėstas modelis geriau atitiko eksperimentinius laikinės sugerties rezultatus.

Tyrimo rezultatai parodė, kad netiesiniai sugerties koeficientai (β_K) didėja didėjant impulso trukmei, nors ties 10 ps pastebimi nukrypimai dėl pasikeitusio bangos ilgio. Be to, pastebėta, kad dangos storis turi įtakos įvertintiems koeficientams, todėl net ir tai pačiai medžiagai su skirtingais dangos storiais, reikalingi atskiri modelio parametrai.

Išvados

Tai pirmasis tyrimas, eksperimentiškai įvertinęs nuo impulso trukmės priklausomą laikinę sugertį dielektrinėse dangose. Parodyta, kad tiek spinduliavimo trukmė, tiek impulso trukmė lemia optinių medžiagos savybių pokytį. Šis darbas paneigia prielaidą apie nekintančius medžiagos parametrus lazerio ir medžiagos sąveikos modeliuose ir pabrėžia defektinių būsenų dinamikos svarbą.

Sugerties įtaka nuovargio efektui

Šio skyriaus turinys pagrįstas publikacijomis [**A3**] ir [**A5**], kurių rezultatai buvo pristatyti konferencijose [**C9**] – [**C11**] ir [**C13**].

Sugertos dozės vaidmuo nustatant optinių elementų ilgaamžiškumą

Lazeriu inicijuojamas nuovargis išlieka esminis iššūkis vertinant optinių dangų ilgalaikį atsparumą, ypač esant sub-katastrofiniam eksponavimui. Nors katastrofinės pažaidos slenksčiai yra gerai ištyrinėti, prognozavimo modelių nekatastrofiniams pažaidos režimams – tokiems kaip spalvinis pokytis – vis dar trūksta. Atsižvelgiant į tai, kad nuovargis yra kaupiamasis reiškinys ir glaudžiai susijęs su sugertos energijos kiekiu, šiame skyriuje tiriama, ar ilgalaikės degradacijos pradžią lemia ne impulsų skaičius ar intensyvumas, bet bendra sugerta dozė.

Tyrimas buvo atliktas su dviejomis dielektrinėmis medžiagomis – HfO_2 ir SiO_2 vienalsuoksnėmis dangomis, nusodintomis naudojant jonų pluošto garinimą ir įvertintomis tiek kaip neapdorotos, tiek termiškai atkaitintos (350°C ir 500°C) būsenomis. Nuovargio elgsena buvo tiriama naudojant 50 kHz dažnio 10 ps impulsus 257 nm – 1030 nm bangos ilgiuose. PLSS matavimai atlikti taikant išplėstą S-į-1 protokolą, nuo 1 iki 10^7 impulsų viename taške. Papildomai buvo atlikti sugerties matavimai, naudojant fototerminę bendro kelio interferometriją su 1 MHz pasikartojimo dažniu ties 266 nm – 1064 nm, leidžiančia tiksliai išmatuoti sugertį panašiomis sąlygomis.

Eksperimentai parodė, kad esant sub-slenkstiniams energijos įtėkiams, spalvinių pokyčių pažaida koreliuoja su sukaupta doze, o ne su aiškiai apibrėžtu PLSS nuovargio slenksčiu. Ši tendencija skiriasi nuo katastrofinės pažaidos, kuriai būdinga aiški, nuo intensyvumo priklausoma nuovargio sotis.

Tyrimas parodė, kad nuovargio sukelti spalviniai pokyčiai nesivysto taip, kaip katastrofinė pažaida. Vietoje to, jie atsiranda sukaupus medžiagos savitą dozės slenkstį, kuris, esant fiksuotai impulso trukmei, išlieka pastovus skirtingiems bangos ilgiams. Šis pastebėjimas rodo, kad spalvinių pokyčių pažaida tiesinės sugerties režime pasižymi deterministine prigimtimi ir yra nulemta pagrindinių medžiagos savybių. Pastebėtina, kad aukštesnėje temperatūroje atkaitintos dangos parodė reikšmingai aukštesnius sugertos dozės slenksčius, o tai rodo padidėjusį atsparumą defektų formavimuisi – šis rezultatas gali būti reikšmingas kuriant patvaresnes dangas ateityje.

Kita svarbi įžvalga – nukrypimas nuo tradicinių slenkstiniais principais pagrįstų pažaidos modelių. Skirtingai nei katastrofinė pažaida, kuri seka įprastomis PLSS mastelio dėsnio priklausomybėmis, spalvinių pokyčių nuovargis kinta palaipsniui ir neturi staigaus soties taško. Šis rezultatas kelia abejonių dėl esamų optinių komponentų ilgaamžiškumo prognozavimo modelių, kurie remiasi laipsniniu PLSS duomenų ekstrapoliavimu. Tyrime pasiūlytas

fenomenologinis, doze pagrįstas, modelis pateikia alternatyvą, kuri tiksliau įvertina tiek intensyvumo, tiek sugerties dinamikos poveikį.

Be to, sugerties matavimų integravimas su PLSS eksperimentais leido išplėsti diagnostines galimybes. Tiesioginis sugerties pokyčių stebėjimas laike leido identifikuoti ankstyvus katastrofinės pažaidos požymius bei atskirti stabilias ir progresuojančias spalvinių pokyčių formas. Šie metodai atskleidė platesnį pažaidos mechanizmų spektrą, kuris nepastebimas atliekant tradicinę mikroskopinę analizę ar vieno impulso testavimą.

Išvados

Šiame tyrime buvo nagrinėtas lazeriu inicijuojamo spalvinio pokyčio nuovargio ir sugerties ryšys vienasluoksnėse HfO_2 ir SiO_2 dielektrinėse dangose, nusodintose jonų pluošto garinimo būdu, esant bangos ilgių intervalui nuo 1030 nm iki 257 mm. Derinant PLSS testavimą su netiesinės sugerties matavimais, nustatyta, kad nuovargio elgsena stipriai priklauso nuo bangos ilgio. Medžiagos rodė didesnę sugertį trumpesniuose bangos ilgiuose, ypač šalia savo sugerties krašto, kur dominuoja žemesnės eilės daugiafotonė sugertis. Kaip ir ankstesniuose tyrimuose, nebuvo stebėta aiški spalvos pokyčio pažaidos pradžios slenkstinė riba.

Vienas svarbiausių šio darbo rezultatų – sugerta dozė, reikalinga spalvinio pokyčio nuovargiui inicijuoti, išlieka beveik pastovi visuose tirtuose bangos ilgiuose, esant fiksuotai impulso trukmei ir impulsų skaičiui, kadangi pažaida kyla dėl tiesinės sugerties. Be to, mažėjant spinduliuotės intensyvumui, bendra sugerta dozė didėja dėl mažėjančios netiesinės sugerties įtakos. Esant intensyvumams, keliomis eilėmis mažesniems nei vieno impulso PLSS, sugerta dozė, atrodo, artėjanti prie pastovios vertės, nors šiam dėsningumui patvirtinti būtini papildomi tyrimai.

Laikiniai sugerties matavimai atskleidė staigų sugerties padidėjimą prieš pat katastrofinės pažaidos pradžią, o tai leidžia manyti, kad šis reiškinys gali būti naudojamas prognozuojančiai diagnostikai. Nors lazerinis atkaitinimas gali būti spartinamas didinant intensyvumą, šiam procesui būdinga soties riba.

Norint paaiškinti šiuos stebėjimus, pasiūlytas fenomenologinis modelis, siejantis medžiagos draustinės juostos plotį, tiesinę ir netiesinę sugertį bei bangos ilgį su bendra sugerta doze ir optinės dangos ilgaamžiškumu. Modelis prognozuoja, kad spalvinio pokyčio nuovargis gali atsirasti dėl tiesinės sugerties, esant mažam intensyvumui, arba dėl netiesinės sugerties, esant didesniam intensyvumui. Šie rezultatai pabrėžia sugerta dalimi grįstų diagnostinių metodų potencialą kaip nekatastrofinę priemonę prognozuoti optinių komponentų ilgaamžiškumą, esant ilgalaikei lazerinei apšvitai.

Sugertos dozės slenkstis dielektrinėse dangose

Šis skyrius pratęsia ankstesnį su sugerta doze susijusį nuovargio tyrimą, išplečiant spinduliavimo trukmę ir analizuojant pažaidos mechanizmus, esant ilgalaikei lazerinei spinduliuotei. Tyrimas buvo atliktas su vienasluoksnėmis dielektrinėmis dangomis (HfO_2, ZrO_2, Al_2O_3), nusodintomis ant lydyto kvarco substratų jonų pluošto garinimo būdu. Bandiniai buvo tiriami kaip neapdoroti arba termiškai atkaitinti 350°C temperatūroje. Eksperimentuose naudotas 1 MHz dažnio 10 ps trukmės lazeris, veikiantis 355 nm bangos ilgiu, kuriuo buvo apšvitintos bandinio vietos nuo 1 iki 10^{10} impulsų vienam taškui. Sugerties dinamika realiuoju laiku buvo stebima fototerminės bendro kelio interferometrijos metodu, taikant laiko skenavimo protokolą su energijos įtėkiais gerokai žemesniais nei vieno impulso PLSS. Po spinduliavimo buvo atlikta morfologinė analizė, pasitelkiant Nomarski mikroskopiją, kuri leido klasifikuoti pažaidą į tris tipus: be pažaidos, su spalvos pokyčiu arba su katastrofine pažaida.

Tyrimas atskleidė du galimus skirtingus spalvos pokyčio formavimosi mechanizmus: lazerinio atkaitinimo skatinamą ryšių susidarymą neapdorotose dangose ir daugiafotoninės jonizacijos sukeltą cheminių ryšių ardymą termiškai atkaitintose dangose. Šie rezultatai suteikia svarbių įžvalgų apie tai, kaip to paties tipo spalvos pokytis gali kilti iš esmingai skirtingų šaltinių, priklausomai nuo medžiagos būklės ir eksponavimo režimo.

Ypač reikšmingas rezultatas – tai, kad netiesinės sugerties režime spalvinis pokytis pasireiškia prieš katastrofinę pažaidą. Tai rodo galimą perėjimą nuo slenksčio neviršijančių modifikacijų iki katastrofinės pažaidos, kuriai tarpininkauja daugiafotonė sugertis. Priešingai, tiesinės sugerties režime – būdingam neatkatintoms dangoms esant mažam intensyvumui – spalvinis pokytis išlieka nekritinis net ir veikiant iki 10^{10} impulsų. Ši dvejopa elgsena pabrėžia tiek medžiagos apdorojimo, tiek lazerio parametrų svarbą, prognozuojant optinių dangų ilgaamžiškumą.

Sugertos dozės analizė dar labiau sustiprina pažaidos režimų skirtį. Katastrofinė pažaida seka daugiafotoninės jonizacijos mechanizmą, pasižymintį aiškiai apibrėžtu PLSS nuovargio slenksčiu, o spalvos pokytis buvo nuosekliai sukeliamas prie beveik pastovios sugertos dozės ribos, nepriklausomai nuo intensyvumo. Tai patvirtina anksčiau siūlytą dozės pagrindu paremtą ilgaamžiškumo modelį ir parodo, kad dielektrinių dangų nuovargio elgsena negali būti universaliai prognozuojama remiantis tradiciniais PLSS kriterijais.

Be to, Time-scan matavimai parodė, kad staigus sugerties padidėjimas yra artėjančios katastrofinės pažaidos požymis, todėl šis rodiklis gali būti naudingas prognozuojant pažaidos pradžią. Priešingai, mažėjanti arba stabili sugertis koreliuoja su nekatastrofiniais arba atkaitinimo pobūdžio spalviniais pokyčiais, todėl laikui bėgant kintanti sugertis tampa svarbiu diagnostiniu požymiu, leidžiančiu atskirti katastrofines ir nekatastrofines pažaidos formas.

Morfologinė analizė šiuos rezultatus papildomai patvirtina: erdviškai

lokalizuota modifikacija siejama su daugiafotoninės jonizacijos sukeltu kaupiamuoju efektu, o tolygiai didėjantys morfologiniai pokyčiai rodo termiškai sukeltą dangos struktūros persitvarkymą. Pastebėtas ryškus spalvinio pokyčio nuovargis be atitinkamo PLSS sumažėjimo ryšys dar kartą pabrėžia šios pažaidos formos nedestruktyvų, tačiau funkciškai reikšmingą pobūdį.

Išvados

UV lazeriu inicijuotas nuovargis, laikinės sugerties elgsena ir sugerta spinduliuotės dozė buvo tiriami vienasluoksnėse dielektrinėse dangose (HfO_2, ZrO_2, Al_2O_3), naudojant 1 MHz dažnio lazerio šaltinį ir veikiant iki 10^{10} impulsų vienoje vietoje. Buvo identifikuoti bent du galimi spalvos pokyčio formavimosi mechanizmai: ryšių susidarymas per lazerinį atkaitinimą termiškai neapdorotose dangose ir ryšių ardymas per daugiafotoninę jonizaciją termiškai atkaitintose dangose. Netiesinės sugerties režime spalvinis pokytis pasireiškia prieš katastrofinę pažaidos pradžią, o tiesinės sugerties srityje išlieka nekritinis.

Sugertos dozės analizė parodė, kad katastrofinė pažaida seka daugiafotoninės jonizacijos lemiamą mechanizmą su aiškiai apibrėžtu PLSS nuovargio slenksčiu. Tuo tarpu spalvos pokytis yra nulemtas sukauptos sugertos dozės, be pastebimo nuovargio slenksčio tirtame impulsų intervale.

Bibliography

[1] Igor Fomenkov, David Brandt, Alex Ershov, Alexander Schafgans, Yezheng Tao, Georgiy Vaschenko, Slava Rokitski, Michael Kats, Michael Vargas, Michael Purvis, Rob Rafac, Bruno La Fontaine, Silvia De Dea, Andrew LaForge, Jayson Stewart, Steven Chang, Matthew Graham, Daniel Riggs, Ted Taylor, Mathew Abraham, and Daniel Brown. Light sources for high-volume manufacturing euv lithography: technology, performance, and power scaling. *Advanced Optical Technologies*, 6(3-4):173–186, 2017. doi: doi:10.1515/aot-2017-0029. URL `https://doi.org/10.1515/aot-2017-0029`.

[2] C.M. Banas and R. Webb. Macro-materials processing. *Proceedings of the IEEE*, 70(6):556–565, 1982. doi: 10.1109/PROC.1982.12354.

[3] Emmanuel Duplay, Zhuo Fan Bao, Sebastian Rodriguez Rosero, Arnab Sinha, and Andrew Higgins. Design of a rapid transit to mars mission using laser-thermal propulsion. *Acta Astronautica*, 192:143–156, 2022. ISSN 0094-5765. doi: https://doi.org/10.1016/j.actaastro.2021.11.032. URL `https://www.sciencedirect.com/science/article/pii/S0094576521006305`.

[4] G. Miller, Edward Moses, and Craig Wuest. The national ignition facility. *Optical Engineering*, 43:2841–2853, 12 2004. doi: 10.1117/1.1814767.

[5] Christopher J. Stolz and Raluca A. Negres. Ten-year summary of the Boulder Damage Symposium annual thin film laser damage competition. *Optical Engineering*, 57(12):1 – 13, 2018. doi: 10.1117/1.OE.57.12.121910. URL `https://doi.org/10.1117/1.OE.57.12.121910`.

[6] B. C. Stuart, M. D. Feit, S. Herman, A. M. Rubenchik, B. W. Shore, and M. D. Perry. Optical ablation by high-power short-pulse lasers. *J. Opt. Soc. Am. B*, 13(2):459–468, Feb 1996.

[7] Shane M. Eaton, Haibin Zhang, Peter R. Herman, Fumiyo Yoshino, Lawrence Shah, James Bovatsek, and Alan Y. Arai. Heat accumulation effects in femtosecond laser-written waveguides with variable repetition rate. *Opt. Express*, 13(12):4708–4716, Jun 2005. doi: 10.1364/OPEX.13.004708. URL `https://opg.optica.org/oe/abstract.cfm?URI=oe-13-12-4708`.

[8] L. D. Merkle, N. Koumvakalis, and M. Bass. Laser-induced bulk damage in sio2 at 1.064, 0.532, and 0.355 um. *Journal of Applied Physics*, 55:772–775, 1984. doi: 10.1063/1.333136.

[9] Laurent Gallais, Jérémie Capoulade, Jean-Yves Natoli, and Mireille Commandré. Investigation of nanodefect properties in optical coatings by coupling measured and simulated laser damage statistics. *Journal of Applied Physics*, 104(5):053120, 09 2008. ISSN 0021-8979. doi: 10.1063/1.2975179. URL `https://doi.org/10.1063/1.2975179`.

[10] Alexandre Chmel. Fatigue laser-induced damage in transparent materials. *Materials Science and Engineering: B*, 49:175–190, 10 1997. doi: 10.1016/S0921-5107(97)00138-4.

[11] Lasers and laser-related equipment — test methods for laser-induced damage threshold — part 2: Threshold determination. Standard 21254-2:2011(en), International Organization for Standardization, 2011.

[12] Detlev Ristau. *Laser-induced damage in optical materials*. CRC Press, 2014.

[13] Laurent Gallais, Benoît Mangote, Myriam Zerrad, Mireille Commandré, Andrius Melninkaitis, Julius Mirauskas, Maksim Jeskevic, and Valdas Sirutkaitis. Laser-induced damage of hafnia coatings as a function of pulse duration in the femtosecond to nanosecond range. *Appl. Opt.*, 50 (9):C178–C187, Mar 2011.

[14] Linas Smalakys, Balys Momgaudis, Robertas Grigutis, Simonas Kičas, and Andrius Melninkaitis. Contrasted fatigue behavior of laser-induced damage mechanisms in single layer zro2 optical coating. *Opt. Express*, 27 (18):26088–26101, Sep 2019.

[15] Arkadi Rosenfeld, Mark A. Lorenz, Razvan Stoian, and David Ashkenasi. Ultrashort-laser-pulse damage threshold of transparent materials and the role of incubation. *Applied Physics A*, 69:S373–S376, 1999.

[16] Linas Smalakys, Evelina Drobužaitė, Balys Momgaudis, Robertas Grigutis, and Andrius Melninkaitis. Quantitative investigation of laser-induced damage fatigue in hfo2 and zro2 single layer coatings. *Opt. Express*, 28(17):25335–25345, Aug 2020.

[17] Lasers and laser-related equipment - test methods for laser-induced damage threshold - part 1: Definitions and general principles (iso/dis 21254-1:2024). Technical Report 21254-1:2024-06 - Draft, International Organization for Standardization, 2024.

[18] Chenzhi Zhang, Ludovic Blarre, Rodger M. Walser, and Michael F. Becker. Mechanisms for laser-induced functional damage to silicon charge-coupled imaging sensors. *Appl. Opt.*, 32(27):5201–5210, Sep 1993. doi: 10.1364/AO.32.005201. URL `https://opg.optica.org/ao/abstract.cfm?URI=ao-32-27-5201`.

[19] P. A. Franken, A. E. Hill, C. W. Peters, and G. Weinreich. Generation of optical harmonics. *Phys. Rev. Lett.*, 7:118–119, Aug 1961. doi: 10.1103/PhysRevLett.7.118. URL `https://link.aps.org/doi/10.1103/PhysRevLett.7.118`.

[20] D. Attwood, E. Bliss, E. Pierce, and L. Coleman. Laser frequency doubling in the presence of small-scale beam breakup. *IEEE Journal of Quantum Electronics*, 12(3):203–204, 1976. doi: 10.1109/JQE.1976.1069114.

[21] R.J. Mears, L. Reekie, I.M. Jauncey, and D.N. Payne. Low-noise erbium-doped fibre amplifier operating at 1.54µm. *Electronics Letters*, 23:1026–1028, 1987. doi: 10.1049/el:19870719. URL https://digital-library.theiet.org/doi/abs/10.1049/el%3A19870719.

[22] Jonas Banys, Justina Savickytė, Ona Balachninaitė, Simona Armalytė, Viktorija Tamulienė, Vygandas Jarutis, and Julius Vengelis. Performance investigation of high-efficiency widely tunable subnanosecond optical parametric generator and amplifier based on mgo:ppln. *Opt. Express*, 30(13):23163–23176, Jun 2022. doi: 10.1364/OE.459826. URL https://opg.optica.org/oe/abstract.cfm?URI=oe-30-13-23163.

[23] Norman M. Kroll. Parametric amplification in spatially extended media and application to the design of tuneable oscillators at optical frequencies. *Phys. Rev.*, 127:1207–1211, Aug 1962. doi: 10.1103/PhysRev.127.1207. URL https://link.aps.org/doi/10.1103/PhysRev.127.1207.

[24] A. Dubietis, G. Jonušauskas, and A. Piskarskas. Powerful femtosecond pulse generation by chirped and stretched pulse parametric amplification in bbo crystal. *Optics Communications*, 88(4):437–440, 1992. ISSN 0030-4018. doi: https://doi.org/10.1016/0030-4018(92)90070-8. URL https://www.sciencedirect.com/science/article/pii/0030401892900708.

[25] Donna Strickland and Gerard Mourou. Compression of amplified chirped optical pulses. *Optics Communications*, 55(6):447–449, 1985. ISSN 0030-4018. doi: https://doi.org/10.1016/0030-4018(85)90151-8. URL https://www.sciencedirect.com/science/article/pii/0030401885901518.

[26] D. F. Swinehart. The beer-lambert law. *Journal of Chemical Education*, 39(7):333, 1962. doi: 10.1021/ed039p333. URL https://doi.org/10.1021/ed039p333.

[27] L. V. Keldysh. Ionization in the field of a strong electromagnetic wave. *Zh. Eksperim. i Teor. Fiz.*, 45(5):1945–1957, 1964.

[28] L.D. Landau and E.M. Lifshitz. *Statistical Physics: By L.D. Landau and E.M. Lifshitz. Translated from the Russian by E. Peierls and R.F. Peierls.* Course of theoretical physics. Elsevier Science, 1958. URL https://books.google.lt/books?id=O2UZyAEACAAJ.

[29] Roger M. Wood. *Laser-Induced Damage of Optical Materials*. CRC Press, 1 edition, 2003.

[30] Oliver Apel, Klaus Mann, Alfons Zoeller, Rainer Goetzelmann, and Eric Eva. Nonlinear absorption of thin al2o3 films at 193 nm. *Appl. Opt.*, 39(18):3165–3169, Jun 2000. doi: 10.1364/AO.39.003165. URL https://opg.optica.org/ao/abstract.cfm?URI=ao-39-18-3165.

[31] A. Couairon, E. Brambilla, T. Corti, D. Majus, O. de J. Ramírez-Góngora, and M. Kolesik. Practitioner's guide to laser pulse propagation models and simulation. *The European Physical Journal Special Topics*, 199(1):5–76, Nov 2011. ISSN 1951-6401. doi: 10.1140/epjst/e2011-01503-3. URL https://doi.org/10.1140/epjst/e2011-01503-3.

[32] Olga Razskazovskaya, Tran Trung Luu, Michael K. Trubetskov, Eleftherios Goulielmakis, and V. Pervak. Nonlinear behavior and damage of dispersive multilayer optical coatings induced by two-photon absorption. In Gregory J. Exarhos, Vitaly E. Gruzdev, Joseph A. Menapace, Detlev Ristau, and MJ Soileau, editors, *Laser-Induced Damage in Optical Materials: 2014*, volume 9237 of *Society of Photo-Optical Instrumentation Engineers (SPIE) Conference Series*, page 92370L, October 2014. doi: 10.1117/12.2068164.

[33] Mohamed Yaseen Noor, Emma Deangelis, Simin Zhang, Conrad Kuz, Justin Twardowski, Aaron Davenport, Carmen S. Menoni, and Enam Chowdhury. Pulse duration dependent effects of ultrafast laser induced damage on a 1030 nm multi-layer dielectric mirror for high repetition rate, high average power laser systems. *Opt. Mater. Express*, 15(2):212–228, Feb 2025. doi: 10.1364/OME.542504. URL https://opg.optica.org/ome/abstract.cfm?URI=ome-15-2-212.

[34] B. Rethfeld. Unified model for the free-electron avalanche in laser-irradiated dielectrics. *Phys. Rev. Lett.*, 92:187401, May 2004. doi: 10.1103/PhysRevLett.92.187401. URL https://link.aps.org/doi/10.1103/PhysRevLett.92.187401.

[35] A. Kaiser, B. Rethfeld, M. Vicanek, and G. Simon. Microscopic processes in dielectrics under irradiation by subpicosecond laser pulses. *Phys. Rev. B*, 61:11437–11450, May 2000. doi: 10.1103/PhysRevB.61.11437. URL https://link.aps.org/doi/10.1103/PhysRevB.61.11437.

[36] Xin Zhao and Yung C Shin. Coulomb explosion and early plasma generation during femtosecond laser ablation of silicon at high laser fluence. *Journal of Physics D: Applied Physics*, 46(33):335501, jul 2013. doi: 10.1088/0022-3727/46/33/335501. URL https://dx.doi.org/10.1088/0022-3727/46/33/335501.

[37] F Costache and J Reif. Femtosecond laser induced coulomb explosion from calcium fluoride. *Thin Solid Films*, 453-454:334–339, 2004. ISSN 0040-6090. doi: https://doi.org/10.1016/j.tsf.2003.11.096. URL https://www.sciencedirect.com/science/article/pii/S0040609003016894. Proceedings of Symposium H on Photonic Processing of Surfaces, Thin Films and Devices, of the E-MRS 2003 Spring Conference.

[38] N. M. Bulgakova, R. Stoian, A. Rosenfeld, I. V. Hertel, W. Marine, and E. E. B. Campbell. A general continuum approach to describe fast electronic transport in pulsed laser irradiated materials: The problem of

coulomb explosion. *Applied Physics A*, 81(2):345–356, Jul 2005. ISSN 1432-0630. doi: 10.1007/s00339-005-3242-0. URL https://doi.org/10.1007/s00339-005-3242-0.

[39] Sha Tao and Benxin Wu. The effect of emitted electrons during femtosecond laser–metal interactions: A physical explanation for coulomb explosion in metals. *Applied Surface Science*, 298:90–94, 2014. ISSN 0169-4332. doi: https://doi.org/10.1016/j.apsusc.2014.01.112. URL https://www.sciencedirect.com/science/article/pii/S0169433214001640.

[40] S. I. Anisimov, B. L. Kapeliovich, and T. L. Perelman. Electron emission from metal surfaces exposed to ultrashort laser pulses. *Zhurnal Eksperimentalnoi i Teoreticheskoi Fiziki*, 66:776–781, August 1974.

[41] S. T. Weber and B. Rethfeld. Phonon-induced long-lasting nonequilibrium in the electron system of a laser-excited solid. *Phys. Rev. B*, 99:174314, May 2019. doi: 10.1103/PhysRevB.99.174314. URL https://link.aps.org/doi/10.1103/PhysRevB.99.174314.

[42] Sridhar Sadasivam, Maria K. Y. Chan, and Pierre Darancet. Theory of thermal relaxation of electrons in semiconductors. *Phys. Rev. Lett.*, 119: 136602, Sep 2017. doi: 10.1103/PhysRevLett.119.136602. URL https://link.aps.org/doi/10.1103/PhysRevLett.119.136602.

[43] J. Faure, J. Mauchain, E. Papalazarou, M. Marsi, D. Boschetto, I. Timrov, N. Vast, Y. Ohtsubo, B. Arnaud, and L. Perfetti. Direct observation of electron thermalization and electron-phonon coupling in photoexcited bismuth. *Phys. Rev. B*, 88:075120, Aug 2013. doi: 10.1103/PhysRevB.88.075120. URL https://link.aps.org/doi/10.1103/PhysRevB.88.075120.

[44] C. W. Carr, H. B. Radousky, A. M. Rubenchik, M. D. Feit, and S. G. Demos. Localized dynamics during laser-induced damage in optical materials. *Phys. Rev. Lett.*, 92:087401, Feb 2004. doi: 10.1103/PhysRevLett.92.087401. URL https://link.aps.org/doi/10.1103/PhysRevLett.92.087401.

[45] Fedor Akhmetov, Igor Milov, Sergey Semin, Fabio Formisano, Nikita Medvedev, Jacobus M. Sturm, Vasily V. Zhakhovsky, Igor A. Makhotkin, Alexey Kimel, and Marcelo Ackermann. Laser-induced electron dynamics and surface modification in ruthenium thin films, 2022. URL https://arxiv.org/abs/2206.08690.

[46] L. A. Falkovsky and E. G. Mishchenko. Electron-lattice kinetics of metals heated by ultrashort laser pulses. *Journal of Experimental and Theoretical Physics*, 88(1):84–88, Jan 1999. ISSN 1090-6509. doi: 10.1134/1.558768. URL https://doi.org/10.1134/1.558768.

[47] M. Sheik-Bahae, A.A. Said, T.-H. Wei, D.J. Hagan, and E.W. Van Stryland. Sensitive measurement of optical nonlinearities using a single beam. *IEEE Journal of Quantum Electronics*, 26(4):760–769, 1990. doi: 10.1109/3.53394.

[48] R. de Nalda, R. del Coso, J. Requejo-Isidro, J. Olivares, A. Suarez-Garcia, J. Solis, and C. N. Afonso. Limits to the determination of the nonlinear refractive index by the z-scan method. *J. Opt. Soc. Am. B*, 19(2):289–296, Feb 2002. doi: 10.1364/JOSAB.19.000289. URL https://opg.optica.org/josab/abstract.cfm?URI=josab-19-2-289.

[49] R A Ganeev. Nonlinear refraction and nonlinear absorption of various media. *Journal of Optics A: Pure and Applied Optics*, 7(12):717, oct 2005. doi: 10.1088/1464-4258/7/12/004. URL https://dx.doi.org/10.1088/1464-4258/7/12/004.

[50] Daniel Correa, Leonardo Boni, Lino Misoguti, Ion Cohanoschi, Florencio Hernandez, and Cleber Mendonca. Z-scan theoretical analysis for three-, four-and five-photon absorption. *Optics Communications*, 277:440–445, 05 2007. doi: 10.1016/j.optcom.2007.05.043.

[51] K K Nagaraja, S Pramodini, P Poornesh, and H S Nagaraja. Effect of annealing on the structural and nonlinear optical properties of zno thin films under cw regime. *Journal of Physics D: Applied Physics*, 46(5): 055106, jan 2013. doi: 10.1088/0022-3727/46/5/055106. URL https://dx.doi.org/10.1088/0022-3727/46/5/055106.

[52] H.M. Zeyada and M.M. Makhlouf. Role of annealing temperatures on structure polymorphism, linear and nonlinear optical properties of nanostructure lead dioxide thin films. *Optical Materials*, 54:181–189, 2016. ISSN 0925-3467. doi: https://doi.org/10.1016/j.optmat.2016.02.031. URL https://www.sciencedirect.com/science/article/pii/S0925346716300921.

[53] Meiling Chen, Jianda Shao, Yuanan Zhao, Guohang Hu, Meiping Zhu, Yingjie Chai, Kaixin Zhang, and Hao Ma. High-sensitivity measurements of the nonlinear absorption coefficient of wide bandgap oxide thin films with the z-scan method. *Opt. Mater. Express*, 12(2):533–544, Feb 2022. doi: 10.1364/OME.447678. URL https://opg.optica.org/ome/abstract.cfm?URI=ome-12-2-533.

[54] Olaf Stenzel, Steffen Wilbrandt, Christian Mühlig, and Sven Schröder. Linear and nonlinear absorption of titanium dioxide films produced by plasma ion-assisted electron beam evaporation: Modeling and experiments. *Coatings*, 10(1), 2020. ISSN 2079-6412. doi: 10.3390/coatings10010059. URL https://www.mdpi.com/2079-6412/10/1/59.

[55] Semyon Papernov, Alexei A. Kozlov, James B. Oliver, Terrance J. Kessler, Alexander Shvydky, and Brendan Marozas. Near-ultraviolet absorption annealing in hafnium oxide thin films subjected to continuous-wave laser radiation. *Optical Engineering*, 53:122504, December 2014. doi: 10.1117/1.OE.53.12.122504.

[56] Mark Kozlowski, C. Wolfe, Michael Staggs, and John Campbell. Large area laser conditioning of dielectric thin film mirrors. *NIST Special Publication*, -1:1–3, 04 1990. doi: 10.1520/STP26505S.

[57] Camille Petite, Jeanne Graisset, Antonin Moreau, Hélène Krol, Catherine Grèzes-Besset, Julien Lumeau, and Laurent Gallais. Low absorption metrology of thin film optical components for high power continuous wave lasers. In Christopher Wren Carr, Detlev Ristau, and Carmen S. Menoni, editors, *Laser-Induced Damage in Optical Materials 2022*, volume 12300, page 123000I. International Society for Optics and Photonics, SPIE, 2022. doi: 10.1117/12.2642761. URL https://doi.org/10.1117/12.2642761.

[58] Facundo Zaldivar Escola, Nélida Mingolo, Oscar E. Martínez, Jorge J. Rocca, and Carmen S. Menoni. Investigation of laser annealing mechanisms in thin film coatings by photothermal microscopy. *Opt. Express*, 27(4):5729–5744, Feb 2019. doi: 10.1364/OE.27.005729. URL https://opg.optica.org/oe/abstract.cfm?URI=oe-27-4-5729.

[59] L. Skuja, M. Hirano, H. Hosono, and K. Kajihara. Defects in oxide glasses. *physica status solidi (c)*, 2(1):15–24, 2005. doi: https://doi.org/10.1002/pssc.200460102. URL https://onlinelibrary.wiley.com/doi/abs/10.1002/pssc.200460102.

[60] J. H. Stathis and M. A. Kastner. Time-resolved photoluminescence in amorphous silicon dioxide. *Phys. Rev. B*, 35:2972–2979, Feb 1987. doi: 10.1103/PhysRevB.35.2972. URL https://link.aps.org/doi/10.1103/PhysRevB.35.2972.

[61] Koichi Kajihara, Linards Skuja, Masahiro Hirano, and Hideo Hosono. Formation and decay of nonbridging oxygen hole centers in sio2 glasses induced by f2 laser irradiation: In situ observation using a pump and probe technique. *Applied Physics Letters*, 79(12):1757–1759, 09 2001. ISSN 0003-6951. doi: 10.1063/1.1404407. URL https://doi.org/10.1063/1.1404407.

[62] G. Petite, P. Daguzan, S. Guizard, and P. Martin. Conduction electrons in wide-bandgap oxides: a subpicosecond time-resolved optical study. *Nuclear Instruments and Methods in Physics Research Section B: Beam Interactions with Materials and Atoms*, 107(1):97–101, 1996. ISSN 0168-583X. doi: https://doi.org/10.1016/0168-583X(95)00845-4. URL https://www.sciencedirect.com/science/article/pii/0168583X95008454.

[63] Sören Richter, Matthias Heinrich, Sven Döring, Andreas Tünnermann, Stefan Nolte, and Ulf Peschel. Nanogratings in fused silica: Formation, control, and applications. *Journal of Laser Applications*, 24(4):042008, 07 2012. ISSN 1042-346X. doi: 10.2351/1.4718561. URL https://doi.org/10.2351/1.4718561. 042008.

[64] S. S. Mao, F. Quéré, S. Guizard, X. Mao, R. E. Russo, G. Petite, and P. Martin. Dynamics of femtosecond laser interactions with dielectrics. *Applied Physics A*, 79(7):1695–1709, Nov 2004. ISSN 1432-0630. doi: 10.1007/s00339-004-2684-0. URL https://doi.org/10.1007/s00339-004-2684-0.

[65] S. Guizard, Phildelia Martin, Guillaume Petite, P D'Oliveira, and P Meynadier. Time-resolved study of laser-induced colour centres in sio2. *Journal of Physics: Condensed Matter*, 8:1281, 01 1999. doi: 10.1088/0953-8984/8/9/018.

[66] T. Suratwala, R. Steele, M.D. Feit, L. Wong, P. Miller, J. Menapace, and P. Davis. Effect of rogue particles on the sub-surface damage of fused silica during grinding/polishing. *Journal of Non-Crystalline Solids*, 354(18):2023–2037, 2008. ISSN 0022-3093. doi: https://doi.org/10.1016/j.jnoncrysol.2007.11.015. URL https://www.sciencedirect.com/science/article/pii/S0022309307013270.

[67] Florian Bonneau, Patrick Combis, Jacques Vierne, and G. Daval. Simulations of laser damage of SiO2 induced by a spherical inclusion. In Gregory J. Exarhos, Arthur H. Guenther, Mark R. Kozlowski, Keith L. Lewis, and M. J. Soileau, editors, *Laser-Induced Damage in Optical Materials: 2000*, volume 4347, pages 308 – 315. International Society for Optics and Photonics, SPIE, 2001. doi: 10.1117/12.425023. URL https://doi.org/10.1117/12.425023.

[68] Laurent Gallais, Xinbin Cheng, and Zhanshan Wang. Influence of nodular defects on the laser damage resistance of optical coatings in the femtosecond regime. *Opt. Lett.*, 39(6):1545–1548, Mar 2014. doi: 10.1364/OL.39.001545. URL https://opg.optica.org/ol/abstract.cfm?URI=ol-39-6-1545.

[69] J-L Miquel, C Lion, and P Vivini. The laser mega-joule : Lmj & petal status and program overview. *Journal of Physics: Conference Series*, 688(1):012067, mar 2016. doi: 10.1088/1742-6596/688/1/012067. URL https://dx.doi.org/10.1088/1742-6596/688/1/012067.

[70] Lukas Rimkus, Julius Darginavičius, Erikas Atkočaitis, and Aurimas Augus. Solid-state femtosecond UV lasers: recent advances and challenges. In Gilles Lérondel, Yong-Hoon Cho, and Atsushi Taguchi, editors, *UV and Higher Energy Photonics: From Materials to Applications 2023*, volume 12652, page 1265206. International Society for Optics and Photonics, SPIE, 2023. doi: 10.1117/12.2676317. URL https://doi.org/10.1117/12.2676317.

[71] Yasunori Furukawa, Steven A. Markgraf, Masayoshi Sato, Hidetsugu Yoshida, Takatomo Sasaki, Hisanori Fujita, Tatsuhiko Yamanaka, and Sadao Nakai. Investigation of the bulk laser damage of lithium triborate, lib3o5, single crystals. *Applied Physics Letters*, 65(12):1480–1482, 1994. doi: 10.1063/1.112018. URL https://doi.org/10.1063/1.112018.

[72] B. J. Nagy, L. Gallais, L. Vámos, D. Oszetzky, P. Rácz, and P. Dombi. Direct comparison of kilohertz- and megahertz-repetition-rate femtosecond damage threshold. *Opt. Lett.*, 40(11):2525–2528, Jun 2015. doi: 10.1364/OL.40.002525. URL https://opg.optica.org/ol/abstract.cfm?URI=ol-40-11-2525.

[73] Chao Meng, Chun Wu, Xuelei Wang, Jingyue Li, and Rui Cao. Effect of thermal fatigue on microstructure and mechanical properties of h13 tool steel processed by selective laser surface melting. *Metals*, 9(7), 2019. ISSN 2075-4701. doi: 10.3390/met9070773. URL https://www.mdpi.com/2075-4701/9/7/773.

[74] Joel P. McDonald, Vanita R. Mistry, Katherine E. Ray, Steven M. Yalisove, John A. Nees, and Neville R. Moody. Femtosecond-laser-induced delamination and blister formation in thermal oxide films on silicon (100). *Applied Physics Letters*, 88(15):153121, 04 2006. ISSN 0003-6951. doi: 10.1063/1.2193777. URL https://doi.org/10.1063/1.2193777.

[75] Mark Mero, Benjamin R. Clapp, Jayesh C. Jasapara, Wolfgang G. Rudolph, Detlev Ristau, Kai Starke, Jörg Krüger, Sven Martin, and Wolfgang Kautek. On the damage behavior of dielectric films when illuminated with multiple femtosecond laser pulses. *Optical Engineering*, 44 (5):051107, 2005. doi: 10.1117/1.1905343. URL https://doi.org/10.1117/1.1905343.

[76] Fei Liu, Hongfei Jiao, Bin Ma, Sebastian Paschel, Istvan Balasa, Detlev Ristau, Zhanshan Wang, Jinlong Zhang, and Xinbin Cheng. Influence of the surface and subsurface contaminants on laser-induced damage threshold of anti-reflection sub-wavelength structures working at 1064 nm. *Optics & Laser Technology*, 127:106144, 2020. ISSN 0030-3992. doi: https://doi.org/10.1016/j.optlastec.2020.106144. URL https://www.sciencedirect.com/science/article/pii/S0030399219318250.

[77] A. Pereira, J.-G. Coutard, S. Becker, I. Tovena, P. Bouchut, and G. Ravel. Impact of organic contamination on 1064-nm laser-induced damage threshold of dielectric mirrors. In Gregory J. Exarhos, Arthur H. Guenther, Keith L. Lewis, Detlev Ristau, M. J. Soileau, and Christopher J. Stolz, editors, *Laser-Induced Damage in Optical Materials: 2006*, volume 6403, page 64030I. International Society for Optics and Photonics, SPIE, 2007. doi: 10.1117/12.696037. URL https://doi.org/10.1117/12.696037.

[78] H. Schröder, P. Wagner, D. Kokkinos, W. Riede, and A. Tighe. Laser-induced contamination and its impact on laser damage threshold. In Gregory J. Exarhos, Vitaly E. Gruzdev, Joseph A. Menapace, Detlev Ristau, and MJ Soileau, editors, *Laser-Induced Damage in Optical Materials: 2013*, volume 8885, page 88850R. International Society for Optics and Photonics, SPIE, 2013. doi: 10.1117/12.2030002. URL https://doi.org/10.1117/12.2030002.

[79] Georges Gebrayel El Reaidy and Laurent Gallais. Analysis of laser-induced contamination at 515 nm in the sub-ps/MHz regime. *Optical Engineering*, 60(3):031004, 2020. doi: 10.1117/1.OE.60.3.031004. URL https://doi.org/10.1117/1.OE.60.3.031004.

[80] Xiulan Ling, Yuanan Zhao, Dawei Li, Shuhong Li, Ming zhou, Jianda Shao, and Zhengxiu Fan. Impact of organic contamination on the laser-induced damage in vacuum. *Applied Surface Science*, 255(22):9255–9258,

2009. ISSN 0169-4332. doi: https://doi.org/10.1016/j.apsusc.2009.07.012. URL https://www.sciencedirect.com/science/article/pii/S0169433209009842.

[81] Marek Stehlik, Janis Zideluns, Camille Petite, Valentin Allard, Marco Minissale, Antonin Moreau, Aude Lereu, Fabien Lemarchand, Frank Wagner, Julien Lumeau, and Laurent Gallais. Investigation of laser-induced contamination on dielectric thin films in mhz sub-ps regime. *Advanced Optical Technologies*, Volume 12 - 2023, 2024. ISSN 2192-8584. doi: 10.3389/aot.2023.1261267. URL https://www.frontiersin.org/journals/advanced-optical-technologies/articles/10.3389/aot.2023.1261267.

[82] S. Möller, Ä. Andresen, C. Merschjann, B. Zimmermann, M. Prinz, and M. Imlau. Insight to uv-induced formation of laser damage on lib3o5 optical surfaces during long-term sum-frequency generation. *Opt. Express*, 15(12):7351–7356, Jun 2007. doi: 10.1364/OE.15.007351. URL http://opg.optica.org/oe/abstract.cfm?URI=oe-15-12-7351.

[83] K. Bien-Aimé, A. Pereira, C. Belin, L. Gallais, P. Grua, I. Tovena-Pecault, J. Néauport, and E. Fargin. Impact of outgassing organic contamination on laser induced damage of optics. In Gregory J. Exarhos, Vitaly E. Gruzdev, Detlev Ristau, M. J. Soileau, and Christopher J. Stolz, editors, *Laser-Induced Damage in Optical Materials: 2009*, volume 7504, page 75040V. International Society for Optics and Photonics, SPIE, 2009. doi: 10.1117/12.836384. URL https://doi.org/10.1117/12.836384.

[84] Georges Gebrayel El Reaidy, Frank R. Wagner, Delphine Faye, and Jean-Yves Natoli. Study of the first stages of laser-induced contamination. *Optical Engineering*, 57(12):121903, 2018. doi: 10.1117/1.OE.57.12.121903. URL https://doi.org/10.1117/1.OE.57.12.121903.

[85] Dam-Bé L. Douti, Laurent Gallais, and Mireille Commandré. Laser-induced damage of optical thin films submitted to 343, 515, and 1030 nm multiple subpicosecond pulses. *Optical Engineering*, 53(12):122509, 2014. doi: 10.1117/1.OE.53.12.122509. URL https://doi.org/10.1117/1.OE.53.12.122509.

[86] Larry D. Merkle, Michael Bass, and Randall T. Swimm. Multiple Pulse Laser-Induced Bulk Damage In Crystalline And Fused Quartz At 1.064 And 0.532 um. *Optical Engineering*, 22(4):224405, 1983. doi: 10.1117/12.7973135. URL https://doi.org/10.1117/12.7973135.

[87] Luke A. Emmert, Mark Mero, and Wolfgang Rudolph. Modeling the effect of native and laser-induced states on the dielectric breakdown of wide band gap optical materials by multiple subpicosecond laser pulses. *Journal of Applied Physics*, 108(4):043523, 08 2010. ISSN 0021-8979. doi: 10.1063/1.3457791. URL https://doi.org/10.1063/1.3457791.

[88] Linas Smalakys and Andrius Melninkaitis. Predicting lifetime of optical components with bayesian inference. *Opt. Express*, 29(2):903–915, Jan

2021. doi: 10.1364/OE.410844. URL https://opg.optica.org/oe/abstract.cfm?URI=oe-29-2-903.

[89] L. Gallais, J.Y. Natoli, and C. Amra. Statistical study of single and multiple pulse laser-induced damage in glasses. *Opt. Express*, 10(25): 1465–1474, Dec 2002. doi: 10.1364/OE.10.001465. URL https://opg.optica.org/oe/abstract.cfm?URI=oe-10-25-1465.

[90] B. Neuenschwander, B. Jaeggi, M. Schmid, A. Dommann, A. Neels, T. Bandi, and G. Hennig. Factors controlling the incubation in the application of ps laser pulses on copper and iron surfaces. In Xianfan Xu, Guido Hennig, Yoshiki Nakata, and Stephan W. Roth, editors, *Laser Applications in Microelectronic and Optoelectronic Manufacturing (LAMOM) XVIII*, volume 8607, page 86070D. International Society for Optics and Photonics, SPIE, 2013. doi: 10.1117/12.2004136. URL https://doi.org/10.1117/12.2004136.

[91] Jonathan Arenberg, Wolfgang Riede, Alessandra Ciapponi, Paul Allenspacher, and Jon Herringer. An empirical investigation of the laser survivability curve. In Gregory J. Exarhos, Vitaly E. Gruzdev, Joseph A. Menapace, Detlev Ristau, and M. J. Soileau, editors, *Laser-Induced Damage in Optical Materials: 2010*, volume 7842, page 78421B. International Society for Optics and Photonics, SPIE, 2010. doi: 10.1117/12.867349. URL https://doi.org/10.1117/12.867349.

[92] Paul Allenspacher, Wolfgang Riede, Denny Wernham, Annalisa Capanni, and Fabio Era. Vacuum laser damage test bench. In Gregory J. Exarhos, Arthur H. Guenther, Keith L. Lewis, Detlev Ristau, M.J. Soileau, and Christopher J. Stolz, editors, *Laser-Induced Damage in Optical Materials: 2005*, volume 5991, page 599128. International Society for Optics and Photonics, SPIE, 2006. doi: 10.1117/12.638550. URL https://doi.org/10.1117/12.638550.

[93] M. Lenzner, J. Krüger, S. Sartania, Z. Cheng, Ch. Spielmann, G. Mourou, W. Kautek, and F. Krausz. Femtosecond optical breakdown in dielectrics. *Phys. Rev. Lett.*, 80:4076–4079, May 1998. doi: 10.1103/PhysRevLett.80.4076. URL https://link.aps.org/doi/10.1103/PhysRevLett.80.4076.

[94] M. Mero, J. Liu, W. Rudolph, D. Ristau, and K. Starke. Scaling laws of femtosecond laser pulse induced breakdown in oxide films. *Phys. Rev. B*, 71:115109, Mar 2005. doi: 10.1103/PhysRevB.71.115109. URL https://link.aps.org/doi/10.1103/PhysRevB.71.115109.

[95] E. S. Bliss. Pulse duration dependence of laser damage mechanisms. *Opto-electronics*, 3(2):99–108, 1971. doi: 10.1007/BF01424087. URL https://doi.org/10.1007/BF01424087.

[96] Oleg M. Efimov, Saurius Juodkazis, and Hiroaki Misawa. Single- and multiple-pulse laser-induced breakdown in transparent dielectrics in the femto-nanosecond region. In Gregory J. Exarhos, Arthur H. Guenther,

Norbert Kaiser, Keith L. Lewis, M. J. Soileau, and Christopher J. Stolz, editors, *Laser-Induced Damage in Optical Materials: 2003*, volume 5273, pages 61 – 73. International Society for Optics and Photonics, SPIE, 2004. doi: 10.1117/12.530098. URL https://doi.org/10.1117/12.530098.

[97] M. H. Niemz. Threshold dependence of laser-induced optical breakdown on pulse duration. *Applied Physics Letters*, 66(10):1181–1183, 1995. doi: 10.1063/1.113850.

[98] J. Krüger, M. Lenzner, S. Martin, M. Lenner, C. Spielmann, A. Fiedler, and W. Kautek. Single- and multi-pulse femtosecond laser ablation of optical filter materials. *Applied Surface Science*, 208-209:233–237, March 2003. doi: 10.1016/S0169-4332(02)01389-2.

[99] D. Du, X. Liu, G. Korn, J. Squier, and G. Mourou. Laser-induced breakdown by impact ionization in sio2 with pulse widths from 7 ns to 150 fs. *Applied Physics Letters*, 64(23):3071–3073, 1994. doi: 10.1063/1.111350.

[100] Jean-Luc Déziel, Louis J. Dubé, and Charles Varin. Dynamical rate equation model for femtosecond laser-induced breakdown in dielectrics. *Phys. Rev. B*, 104:045201, Jul 2021. doi: 10.1103/PhysRevB.104.045201. URL https://link.aps.org/doi/10.1103/PhysRevB.104.045201.

[101] Andrius Melninkaitis, Darius Mikšys, Rimantas Grigonis, Valdas Sirutkaitis, Marco Jupé, and Detlev Ristau. Comparative studies of laser-induced damage threshold measurements in highly reflecting mirrors. In Gregory J. Exarhos, Arthur H. Guenther, Keith L. Lewis, Detlev Ristau, M. J. Soileau, and Christopher J. Stolz, editors, *Laser-Induced Damage in Optical Materials: 2007*, volume 6720, page 672012. International Society for Optics and Photonics, SPIE, 2007. doi: 10.1117/12.753705. URL https://doi.org/10.1117/12.753705.

[102] Arlee V. Smith and Binh T. Do. Bulk and surface laser damage of silica by picosecond and nanosecond pulses at 1064 nm. *Appl. Opt.*, 47(26): 4812–4832, Sep 2008. doi: 10.1364/AO.47.004812. URL http://opg.optica.org/ao/abstract.cfm?URI=ao-47-26-4812.

[103] Fanyu Kong, Yunxia Jin, Dawei Li, Weixiao Chen, Meiping Zhu, Tao Wang, Chaoyang Li, Hongbo He, Guang Xu, and Jianda Shao. Effect of pulse duration on laser induced damage threshold of multilayer dielectric gratings. In Gregory J. Exarhos, Vitaly E. Gruzdev, Joseph A. Menapace, Detlev Ristau, and M J Soileau, editors, *Laser-Induced Damage in Optical Materials: 2012*, volume 8530, pages 125 – 133. International Society for Optics and Photonics, SPIE, 2012. doi: 10.1117/12.977339. URL https://doi.org/10.1117/12.977339.

[104] Amlan Das, Andong Wang, Olivier Uteza, and David Grojo. Pulse-duration dependence of laser-induced modifications inside silicon. *Opt. Express*, 28(18):26623–26635, Aug 2020. doi: 10.1364/OE.398984. URL http://opg.optica.org/oe/abstract.cfm?URI=oe-28-18-26623.

[105] Xusan Yang, Hao Xie, Eric Alonas, Yujia Liu, Xuanze Chen, Philip J. Santangelo, Qiushi Ren, Peng Xi, and Dayong Jin. Mirror-enhanced super-resolution microscopy. *Light: Science & Applications*, 5(6):e16134–e16134, Jun 2016. ISSN 2047-7538. doi: 10.1038/lsa.2016.134. URL https://doi.org/10.1038/lsa.2016.134.

[106] Tatiana Ștefanov, Harsha Vardhan Reddy Maraka, Philip Meagher, James Rice, Wim Sillekens, and David J. Browne. Thin film metallic glass broad-spectrum mirror coatings for space telescope applications. *Journal of Non-Crystalline Solids: X*, 7:100050, 2020. ISSN 2590-1591. doi: https://doi.org/10.1016/j.nocx.2020.100050. URL https://www.sciencedirect.com/science/article/pii/S2590159120300078.

[107] Thilo Sandner, Jan Uwe Schmidt, Harald Schenk, Hubert Lakner, Minghong Yang, Alexandre Gatto, Norbert Kaiser, Stefan Braun, Thomas Foltyn, and Andreas Leson. Highly reflective optical coatings for high-power applications of micro scanning mirrors in the UV-VIS-NIR spectral region. In Hakan Ürey, David L. Dickensheets, and Bishnu P. Gogoi, editors, *MOEMS Display, Imaging, and Miniaturized Microsystems IV*, volume 6114, page 61140H. International Society for Optics and Photonics, SPIE, 2006. doi: 10.1117/12.644626. URL https://doi.org/10.1117/12.644626.

[108] A. Piegari and F. Flory. *Optical Thin Films and Coatings: From Materials to Applications*. Woodhead Publishing Series in Electronic and Optical Materials. Elsevier Science, 2018. ISBN 9780081020999. URL https://books.google.lt/books?id=-xxhDwAAQBAJ.

[109] M. Sparks and E. Loh. Temperature dependence of absorptance in laser damage of metallic mirrors: I. melting. *J. Opt. Soc. Am.*, 69(6):847–858, Jun 1979. doi: 10.1364/JOSA.69.000847. URL http://opg.optica.org/abstract.cfm?URI=josa-69-6-847.

[110] G.D. Tsibidis, D. Mansour, and E. Stratakis. Damage threshold evaluation of thin metallic films exposed to femtosecond laser pulses: The role of material thickness. *Optics & Laser Technology*, 156:108484, 2022. ISSN 0030-3992. doi: https://doi.org/10.1016/j.optlastec.2022.108484. URL https://www.sciencedirect.com/science/article/pii/S0030399222006375.

[111] Matthias Domke, Luigi Nobile, Stephan Rapp, Sasia Eiselen, Jürgen Sotrop, Heinz P. Huber, and Michael Schmidt. Understanding thin film laser ablation: The role of the effective penetration depth and the film thickness. *Physics Procedia*, 56:1007–1014, 2014. ISSN 1875-3892. doi: https://doi.org/10.1016/j.phpro.2014.08.012. URL https://www.sciencedirect.com/science/article/pii/S1875389214001576. 8th International Conference on Laser Assisted Net Shape Engineering LANE 2014.

[112] Nan Zheng, Ricardas Buividas, Hsin-hui Huang, Dominyka Stonyte, Suresh Palanisamy, Tomas Katkus, Maciej Kretkowski, Paul Stoddart,

and Saulius Juodkazis. Laser machining at high pw/cm2 intensity and high throughput. *Photonics*, 11:598, 06 2024. doi: 10.3390/photonics11070598.

[113] Simas Butkus, Vytautas Jukna, Evaldas Kazukauskass, Zilvinas Svirksas, Domas Paipulas, and Valdas Sirutkaitis. High-contrast marking of stainless-steel using bursts of femtosecond laser pulses. *Micromachines*, 14:194, 01 2023. doi: 10.3390/mi14010194.

[114] Beat Neuenschwander, Beat Jaeggi, Marc Schmid, Vincent Rouffiange, and Paul-E. Martin. Optimization of the volume ablation rate for metals at different laser pulse-durations from ps to fs. In Guido Hennig, Xianfan Xu, Bo Gu, and Yoshiki Nakata, editors, *Laser Applications in Microelectronic and Optoelectronic Manufacturing (LAMOM) XVII*, volume 8243, page 824307. International Society for Optics and Photonics, SPIE, 2012. doi: 10.1117/12.908583. URL https://doi.org/10.1117/12.908583.

[115] Thibault Genieys, Marc Sentis, and Olivier Utéza. Measurement of ultrashort laser ablation of four metals (al, cu, ni, w) in the single-pulse regime. *Advanced Optical Technologies*, 9(3):131–143, 2020. doi: doi:10.1515/aot-2019-0064. URL https://doi.org/10.1515/aot-2019-0064.

[116] Jianjun Yang, Youbo Zhao, Nan Zhang, Yanmei Liang, and Mingwei Wang. Ablation of metallic targets by high-intensity ultrashort laser pulses. *Phys. Rev. B*, 76:165430, Oct 2007. doi: 10.1103/PhysRevB.76.165430. URL https://link.aps.org/doi/10.1103/PhysRevB.76.165430.

[117] Norman Hodgson, Sebastian Heming, Albrecht Steinkopff, Hatim Haloui, and Tony S. Lee. Lasers in manufacturing conference 2019 ultrafast laser ablation at 1035 nm , 517 nm and 345 nm as a function of pulse duration and fluence. 2019. URL https://api.semanticscholar.org/CorpusID:203629417.

[118] M Hashida, A.F Semerok, O Gobert, G Petite, Y Izawa, and J.F-Wagner. Ablation threshold dependence on pulse duration for copper. *Applied Surface Science*, 197-198:862–867, 2002. ISSN 0169-4332. doi: https://doi.org/10.1016/S0169-4332(02)00463-4. URL https://www.sciencedirect.com/science/article/pii/S0169433202004634. COLA'01 SI.

[119] YongJian Zhu, Yunfeng Ma, Wang Cheng, Zhixi Zhang, Wenyun Kang, Fang Bai, ChenXin Cao, Guangyan Guo, Yasong Chow, Tao Zhong, Tianzhuo Zhao, and Zhongwei Fan. Laser-induced damage thresholds in sio2-coated aluminum mirrors under various ultrashort pulse widths. *Appl. Opt.*, 64(5):1235–1245, Feb 2025. doi: 10.1364/AO.547110. URL https://opg.optica.org/ao/abstract.cfm?URI=ao-64-5-1235.

[120] Guillaume Duchateau and Anthony Dyan. Coupling statistics and heat transfer to study laser-induced crystal damage by nanosecond pulses. *Opt. Express*, 15(8):4557–4576, Apr 2007.

[121] Guillaume Duchateau. Simple models for laser-induced damage and conditioning of potassium dihydrogen phosphate crystals by nanosecond pulses. *Opt. Express*, 17(13):10434–10456, Jun 2009.

[122] A. Dyan, F. Enguehard, S. Lallich, H. Piombini, and G. Duchateau. Scaling laws in laser-induced potassium dihydrogen phosphate crystal damage by nanosecond pulses at 3ω. *J. Opt. Soc. Am. B*, 25(6):1087–1095, Jun 2008.

[123] Jérémie Capoulade, Laurent Gallais, Jean-Yves Natoli, and Mireille Commandré. Multiscale analysis of the laser-induced damage threshold in optical coatings. *Appl. Opt.*, 47(29):5272–5280, Oct 2008. doi: 10.1364/AO.47.005272. URL `https://opg.optica.org/ao/abstract.cfm?URI=ao-47-29-5272`.

[124] F. Bonneau, P. Combis, J. L. Rullier, J. Vierne, M. Pellin, M. Savina, M. Broyer, E. Cottancin, J. Tuaillon, M. Pellarin, L. Gallais, J. Y. Natoli, M. Perra, H. Bercegol, L. Lamaignère, M. Loiseau, and J. T. Donohue. Study of uv laser interaction with gold nanoparticles embedded in silica. *Applied Physics B*, 75(8):803–815, Dec 2002. ISSN 1432-0649. doi: 10.1007/s00340-002-1049-7. URL `https://doi.org/10.1007/s00340-002-1049-7`.

[125] Mihai-George Mureșan, Jan Vanda, Saulius Pakalnis, Martin Mydlář, and Jan Brajer. Influence of laser beam size on the determination of LIDT. In Christopher Wren Carr, Detlev Ristau, Carmen S. Menoni, and Michael D. Thomas, editors, *Laser-Induced Damage in Optical Materials 2023*, volume 12726, page 127260H. International Society for Optics and Photonics, SPIE, 2023. doi: 10.1117/12.2686177. URL `https://doi.org/10.1117/12.2686177`.

[126] N. Sanner, B. Bussiere, O. Utéza, A. Leray, T. Itina, M. Sentis, J. Y. Natoli, and M. Commandré. Influence of the beam-focus size on femtosecond laser-induced damage threshold in fused silica. In Joseph Neev, Stefan Nolte, Alexander Heisterkamp, and Christopher B. Schaffer, editors, *Commercial and Biomedical Applications of Ultrafast Lasers VIII*, volume 6881, page 68810W. International Society for Optics and Photonics, SPIE, 2008. doi: 10.1117/12.762767. URL `https://doi.org/10.1117/12.762767`.

[127] Hailong Hong, Qiang Liu, Lei Huang, and Mali Gong. Improvement and formation of uv-induced damage on lbo crystal surface during long-term high-power third-harmonic generation. *Opt. Express*, 21(6):7285–7293, Mar 2013. doi: 10.1364/OE.21.007285. URL `http://opg.optica.org/oe/abstract.cfm?URI=oe-21-6-7285`.

[128] Rimantas Budriūnas, Tomas Stanislauskas, Jonas Adamonis, Aidas Aleknavičius, Gediminas Veitas, Darius Gadonas, Stanislovas Balickas, Andrejus Michailovas, and Arūnas Varanavičius. 53 w average power cep-stabilized opcpa system delivering 5.5 tw few cycle pulses at 1 khz repetition rate. *Opt. Express*, 25(5):5797–5806, Mar 2017. doi:

10.1364/OE.25.005797. URL https://opg.optica.org/oe/abstract.cfm?URI=oe-25-5-5797.

[129] Vincent Loriot, Gregory Gitzinger, and Nicolas Forget. Self-referenced characterization of femtosecond laser pulses by chirp scan. *Opt. Express*, 21(21):24879–24893, Oct 2013. doi: 10.1364/OE.21.024879. URL https://opg.optica.org/oe/abstract.cfm?URI=oe-21-21-24879.

[130] Michael Borden, James Folta, Christopher Stolz, John Taylor, Justin Wolfe, Andrew Griffin, and Michael Thomas. Improved method for laser damage testing coated optics - art. no. 59912a. *Proceedings of SPIE - The International Society for Optical Engineering*, 5991, 12 2005. doi: 10.1117/12.637825.

[131] Small optics laser damage test procedure. Standard MEL01-013-OE, Lawrence Livermore National Laboratory, USA, 2017.

[132] A. Alexandrovski, Martin Fejer, A. Markosian, and Roger Route. Photothermal common-path interferometry (PCI): new developments. In W. Andrew Clarkson, Norman Hodgson, and Ramesh K. Shori, editors, *Solid State Lasers XVIII: Technology and Devices*, volume 7193, page 71930D. International Society for Optics and Photonics, SPIE, 2009. doi: 10.1117/12.814813. URL https://doi.org/10.1117/12.814813.

[133] Giedrius Abromavičius, Simonas Kičas, and Rytis Buzelis. High temperature annealing effects on spectral, microstructural and laser damage resistance properties of sputtered hfo2 and hfo2-sio2 mixture-based uv mirrors. *Optical Materials*, 95:109245, 2019. ISSN 0925-3467. doi: https://doi.org/10.1016/j.optmat.2019.109245. URL https://www.sciencedirect.com/science/article/pii/S0925346719304562.

[134] T. H. Maiman, R. H. Hoskins, I. J. D'Haenens, C. K. Asawa, and V. Evtuhov. Stimulated optical emission in fluorescent solids. ii. spectroscopy and stimulated emission in ruby. *Phys. Rev.*, 123:1151–1157, Aug 1961. doi: 10.1103/PhysRev.123.1151. URL https://link.aps.org/doi/10.1103/PhysRev.123.1151.

[135] Zhongyang Li, Edgar Palacios, Serkan Butun, Hasan Kocer, and Koray Aydin. Omnidirectional, broadband light absorption using large-area, ultrathin lossy metallic film coatings. *Scientific Reports*, 5(1):15137, Oct 2015. ISSN 2045-2322. doi: 10.1038/srep15137. URL https://doi.org/10.1038/srep15137.

[136] M. Trubetskov, T. Amotchkina, L. Lehnert, J. Sancho-Parramon, K. Golyari, V. Janicki, M. Ossiander, M. Schultze, and V. Pervak. Broadband phase-shifting mirrors for ultrafast lasers. *Appl. Opt.*, 59(5):A123–A127, Feb 2020. doi: 10.1364/AO.59.00A123. URL https://opg.optica.org/ao/abstract.cfm?URI=ao-59-5-A123.

[137] Gang Wang, Tingyi Liu, Jiale Chao, Hong Jin, Jiayao Liu, Han Zhang, Wenhao Lyu, Peng Yin, Ahmed Al-Ghamdi, Swelm Wageh,

Bo Fu, and Han Zhang. Recent advances and challenges in ultrafast photonics enabled by metal nanomaterials. *Advanced Optical Materials*, 10(11):2200443, 2022. doi: https://doi.org/10.1002/adom.202200443. URL https://onlinelibrary.wiley.com/doi/abs/10.1002/adom.202200443.

[138] S. I. Anisimov and B. S. Luk'yanchuk. Selected problems of laser ablation theory. *Physics-Uspekhi*, 45(3):293–324, 2002. doi: 10.1070/PU2002v045n03ABEH001003. URL https://ufn.ru/en/articles/2002/3/b/.

[139] P.A. Tipler. *Physics for Scientists and Engineers: Vol. 1: Mechanics, Oscillations and Waves, Thermodynamics*. Physics for Scientists and Engineers. W. H. Freeman, 1999. ISBN 9781572594913. URL https://books.google.lt/books?id=U9lkAkTdAosC.

[140] Junrong Ma and Changsuo Zhang. Ignition thresholds and flame propagation of methane/air mixtures ignited via radiatively heated inert particles. *Energies*, 14:5173, 08 2021. doi: 10.3390/en14165173.

[141] Bin Wang and Laurent Gallais. A theoretical investigation of the laser damage threshold of metal multi-dielectric mirrors for high power ultrashort applications. *Opt. Express*, 21(12):14698–14711, Jun 2013. doi: 10.1364/OE.21.014698. URL http://opg.optica.org/oe/abstract.cfm?URI=oe-21-12-14698.

[142] Bin Wang and Laurent Gallais. A theoretical investigation of the laser damage threshold of metal multi-dielectric mirrors for high power ultrashort applications. *Opt. Express*, 21(12):14698–14711, Jun 2013. doi: 10.1364/OE.21.014698. URL https://opg.optica.org/oe/abstract.cfm?URI=oe-21-12-14698.

[143] Yong Jee, Michael F. Becker, and Rodger M. Walser. Laser-induced damage on single-crystal metal surfaces. *J. Opt. Soc. Am. B*, 5(3):648–659, Mar 1988. doi: 10.1364/JOSAB.5.000648. URL http://opg.optica.org/josab/abstract.cfm?URI=josab-5-3-648.

[144] C. S. Lee, N. Koumvakalis, and M. Bass. A theoretical model for multiple-pulse laser-induced damage to metal mirrors. *Journal of Applied Physics*, 54(10):5727–5731, 10 1983. ISSN 0021-8979. doi: 10.1063/1.331794. URL https://doi.org/10.1063/1.331794.

[145] Henry M Musal. Thermomechanical stress degradation of metal mirror surfaces under pulsed-laser irradiation. *Laser Induced Damage in Optical Materials: 1979*, pages 159–173, 1980.

[146] A. Rosenfeld, M. Lorenz, R. Stoian, and D. Ashkenasi. Ultrashort-laser-pulse damage threshold of transparent materials and the role of incubation. *Applied Physics A*, 69(1):S373–S376, Dec 1999. ISSN 1432-0630. doi: 10.1007/s003390051419. URL https://doi.org/10.1007/s003390051419.

[147] Kevin Kiedrowski, Marco Jupé, Henrik Ehlers, Michael Kennedy, Andreas Wienke, and Detlev Ristau. Challenges in the development of a reliable cw-lidt measurement routine. *Opt. Mater. Express*, 13(6):1712–1725, Jun 2023. doi: 10.1364/OME.488629. URL https://opg.optica.org/ome/abstract.cfm?URI=ome-13-6-1712.

[148] D. Franta, D. Nečas, L. Zajíčková, I. Ohlídal, and J. Stuchlík. Advanced modeling for optical characterization of amorphous hydrogenated silicon films. *Thin Solid Films*, 541:12–16, 2013.

[149] K. M. Davis, K. Miura, N. Sugimoto, and K. Hirao. Writing waveguides in glass with a femtosecond laser. *Opt. Lett.*, 21(21):1729–1731, Nov 1996. doi: 10.1364/OL.21.001729. URL http://opg.optica.org/ol/abstract.cfm?URI=ol-21-21-1729.

[150] Balys Momgaudis, Viaceslav Kudriasov, Mikas Vengris, and Andrius Melninkaitis. Quantitative assessment of nonlinearly absorbed energy in fused silica via time-resolved digital holography. *Opt. Express*, 27 (5):7699–7711, Mar 2019. doi: 10.1364/OE.27.007699. URL http://opg.optica.org/oe/abstract.cfm?URI=oe-27-5-7699.

[151] An-Chun Tien, Sterling Backus, Henry Kapteyn, Margaret Murnane, and Gérard Mourou. Short-pulse laser damage in transparent materials as a function of pulse duration. *Phys. Rev. Lett.*, 82:3883–3886, May 1999. doi: 10.1103/PhysRevLett.82.3883. URL https://link.aps.org/doi/10.1103/PhysRevLett.82.3883.

[152] Alexei Alexandrovski, Gisele Foulon, Lawrence Myers, Roger Route, and Martin Fejer. Uv and visible absorption in litao3. *Proceedings of SPIE - The International Society for Optical Engineering*, 3610, 05 1999. doi: 10.1117/12.349242.

[153] Bincheng Li, Sven Martin, and Eberhard Welsch. Pulsed top-hat beam thermal-lens measurement for ultraviolet dielectric coatings. *Opt. Lett.*, 24(20):1398–1400, Oct 1999. doi: 10.1364/OL.24.001398. URL https://opg.optica.org/ol/abstract.cfm?URI=ol-24-20-1398.

[154] Bincheng Li, S. Martin, and E. Welsch. Laser conditioning and nonlinear absorption of laf3/mgf2 dielectric multilayers at 193 nm. *Applied Physics A*, 74:27–33, 02 2002. doi: 10.1007/s003390100867.

[155] Bincheng Li, Shengming Xiong, Yundong Zhang, S. Martin, and E. Welsch. Nonlinear absorption measurement of uv dielectric components by pulsed top-hat beam thermal lens. *Optics Communications*, 244(1):367–376, 2005. ISSN 0030-4018. doi: https://doi.org/10.1016/j.optcom.2004.09.018. URL https://www.sciencedirect.com/science/article/pii/S0030401804009046.

[156] Jun Shi, Meiping Zhu, Wenyun Du, Tianbao Liu, Li Zhou, Youen Jiang, and Jianda Shao. Effect of annealing on the properties of hfo2-al2o3 mixture coatings for picosecond laser applications. *Applied Surface Science*, 579:152192, 2022. ISSN 0169-4332. doi: https://doi.org/10.1016/j.

apsusc.2021.152192. URL https://www.sciencedirect.com/science/article/pii/S0169433221032207.

[157] Franz Urbach. The long-wavelength edge of photographic sensitivity and of the electronic absorption of solids. *Phys. Rev.*, 92:1324–1324, Dec 1953. doi: 10.1103/PhysRev.92.1324. URL https://link.aps.org/doi/10.1103/PhysRev.92.1324.

[158] Y. Toyozawa, K.S. Song, and R.T. Williams. *Self-Trapped Excitons*. Springer Series in Solid-State Sciences. Springer Berlin Heidelberg, 2013. ISBN 9783642852367. URL https://books.google.lt/books?id=ZLDoCAAAQBAJ.

[159] Zhanliang Sun, Matthias Lenzner, and Wolfgang Rudolph. Generic incubation law for laser damage and ablation thresholds. *Journal of Applied Physics*, 117(7):073102, 02 2015. ISSN 0021-8979. doi: 10.1063/1.4913282. URL https://doi.org/10.1063/1.4913282. 073102.

[160] Klaus R. Mann and Eric Eva. Characterizing the absorption and aging behavior of DUV optical material by high-resolution excimer laser calorimetry. In Luc van den Hove, editor, *Optical Microlithography XI*, volume 3334 of *Society of Photo-Optical Instrumentation Engineers (SPIE) Conference Series*, pages 1055–1061, June 1998. doi: 10.1117/12.310736.

[161] Fatma Abdel Samad, Mohammed Ali Jasim, Alaa Mahmoud, Yasmin Abd El-Salam, Hamza Qayyum, Retna Apsari, and Tarek Mohamed. Experimental investigation of the optical nonlinearity of laser-ablated titanium dioxide nanoparticles using femtosecond laser light pulses. *Nanomaterials*, 14(23), 2024. ISSN 2079-4991. doi: 10.3390/nano14231940. URL https://www.mdpi.com/2079-4991/14/23/1940.

[162] D. Sahoo, P. Priyadarshini, R. Dandela, D. Alagarasan, R. Ganesan, S. Varadharajaperumal, and R. Naik. In situ laser irradiation: the kinetics of the changes in the nonlinear/linear optical parameters of as50se40sb10 thin films for photonic applications. *RSC Adv.*, 11:16015–16025, 2021. doi: 10.1039/D1RA02368C. URL http://dx.doi.org/10.1039/D1RA02368C.

[163] Abinash Parida, D. Alagarasan, R. Ganesan, Sagar Bisoyi, and R. Naik. Influence of time dependent laser-irradiation for tuning the linear–nonlinear optical response of quaternary ag10in15s15se60 films for optoelectronic applications. *RSC Adv.*, 13:4236–4248, 2023. doi: 10.1039/D2RA07981J. URL http://dx.doi.org/10.1039/D2RA07981J.

[164] Young In Jhon and Ju Han Lee. Saturable absorption dynamics of highly stacked 2d materials for ultrafast pulsed laser production. *Applied Sciences*, 11(6), 2021. ISSN 2076-3417. doi: 10.3390/app11062690. URL https://www.mdpi.com/2076-3417/11/6/2690.

[165] Erikas Atkočaitis, Linas Smalakys, and Andrius Melninkaitis. Pulse temporal scaling of lidt for anti-reflective coatings deposited on lithium triborate crystals. *Opt. Express*, 30(16):28401–28413, Aug 2022. doi: 10.

1364/OE.459391. URL https://opg.optica.org/oe/abstract.cfm?URI=oe-30-16-28401.

[166] L. Béziat, N. Roquin, and L. Lamaignère. Multishot laser damage of multilayer dielectric mirrors in the near-infrared subpicosecond regime. *Appl. Opt.*, 63(20):5403–5410, Jul 2024. doi: 10.1364/AO.528931. URL https://opg.optica.org/ao/abstract.cfm?URI=ao-63-20-5403.

[167] P.T Mannion, J Magee, E Coyne, G.M O'Connor, and T.J Glynn. The effect of damage accumulation behaviour on ablation thresholds and damage morphology in ultrafast laser micro-machining of common metals in air. *Applied Surface Science*, 233(1):275–287, 2004. ISSN 0169-4332. doi: https://doi.org/10.1016/j.apsusc.2004.03.229. URL https://www.sciencedirect.com/science/article/pii/S0169433204004799.

[168] Erikas Atkočaitis, Austėja Aleksiejūtė, Justinas Galinis, and Andrius Melninkaitis. Role of absorbed dose in a lifetime of hfo2 and sio2 dielectric coatings. *Opt. Express*, 33(7):14825–14842, Apr 2025. doi: 10.1364/OE.553105. URL https://opg.optica.org/oe/abstract.cfm?URI=oe-33-7-14825.

[169] N. Kaiser and H.K. Pulker. *Optical Interference Coatings*, pages 131–154. Springer Series in Optical Sciences. Springer Berlin Heidelberg, 2013. ISBN 9783540363866. URL https://books.google.lt/books?id=NxT_CAAAQBAJ.

[170] Tingting Zeng, Meiping Zhu, Yingjie Chai, Chaoyi Yin, Nuo Xu, Kui Yi, Yanzhi Wang, Yuanan Zhao, Guohang Hu, and Jianda Shao. Effects of water adsorption on properties of electron-beam hfo2/sio2 high-reflection coatings. *Thin Solid Films*, 697:137826, 2020. ISSN 0040-6090. doi: https://doi.org/10.1016/j.tsf.2020.137826. URL https://www.sciencedirect.com/science/article/pii/S0040609020300420.

Curriculum Vitae

Name: Erikas

Surname: Atkočaitis

Place of birth: Vilnius, Lithuania

E-mail: erikas.atkocaitis@ff.vu.lt

Education:

2021–2025	Vilnius University, Faculty of Physics, Laser Research Center *Ph.D. studies*
2019–2021	Vilnius University, Faculty of Physics, Laser Research Center *Master of Science*
2018 04 01–08 31	Augsburg University, Faculty of Mathematics, Natural Sciences, and Materials Engineering *Erasmus+ Exchange program*
2015–2019	Vilnius University, Faculty of Physics *Bachelor of Science*
2011–2015	Vilnius Mykolas Bižiška's Gymnasium
2004–2011	Vilnius Gabija's Gymnasium

Work experience:

2022–present	**Laser Technician** R&D department, Light Conversion Ltd.
2021–present	**Assistant Researcher** Vilnius University Faculty of Physics, Laser Research Center

2021–2023	**Specialist**
	Vilnius University Faculty of Physics,
	Laser Research Center
2020–present	**Laboratory Assistant**
	Vilnius University Faculty of Physics,
	Laser Research Center
2019–2021	**Junior Research Analyst**
	Lidaris Ltd.

Internships:

2025 08 29	Assembly "Lazeriai. Mokslas ir technologijos 2025" (Vilnius, Lithuania)
2025 01 25–30	SPIE Photonics West conference (San Francisco, CA, USA)
2024 08 25–26	Summer school in EPS-QEOD Europhoton conference (Vilnius, Lithuania)
2024 08 23–24	Assembly "Lazeriai. Mokslas ir technologijos 2024" (Dubingiai, Lithuania)
2023 04 05	ELI workshop "Laser particle accelerators, their applications, and possibilities of experiments in the ELI infrastructure" (Vilnius, Lithuania)

Academic activities:

2024 08 25–30	**Assitant**
	EPS-QEOD Europhoton conference
	(Vilnius, Lithuania)
2023–2024	**Head of Conference Operations and Academic Relations**
	Open Readings Conference (Vilnius, Lithuania)
2023 11 20–21	**Invited presenter**
	American International School of Vilnius
	(Vilnius, Lithuania)
2022–2023	**Conference Coordinator**
	Open Readings Conference (Vilnius, Lithuania)
2021–2023	**Finance Manager**
	Open Readings Conference (Vilnius, Lithuania)

Honors and awards:

2024 **The MJ Soileau Best Student Paper Award**
SPIE Laser Damage 2024 (San Ramon, CA, USA)

Vilnius University Press
Saulėtekio al. 9, LT-10222 Vilnius
e-mail: info@leidykla.vu.lt,
www.leidykla.vu.lt
bookshop.vu.lt
journals.vu.lt
Print run copies 20